A Fast-Track Method for Fatigue Crack Growth Prediction with a Cohesive Zone Model

A Thesis Submitted to the University of Manchester for the degree of PhD in the Faculty of Engineering and Physical Science

2013

HENDERY DAHLAN

School of Mechanical, Aerospace and Civil Engineering

List of Content

Word Count: 33,810

List of Figure

List of Table

Abstract

An alternative point of view with regard to understanding the mechanism of energy transfer involved to create new surface is considered in this study. A combination of transport equation and cohesive element is presented. A practical demonstration in 1-D is presented to simulate the mechanism of energy transfer in a damage zone model for both elastic and elastic-plastic materials. The combination of transport and cohesion element shows the extent elastic energy plays to supply the energy required for crack growth. Meanwhile, plastic energy dissipation for an elastic-plastic material is shown to be well described by the transport approach.

The cohesive zone model is one of many alternative approaches used to simulate fatigue crack growth. The model incorporates a relationship between cohesive traction and separation in the zone ahead of a crack tip. The model introduces irreversibility into the constitutive relationships by means of damage accumulation with cyclic loading. The traction-separation relationship underpinning the cohesive zone model is not required to follow a predetermined path, but is dependent on irreversibility introduced by decreasing a critical cohesive traction parameter. The approach can simulate fatigue crack growth without the need for re-meshing and caters for constant amplitude loading and single overloading. This study shows the retardation phenomenon occurring in elastic plastic-materials due to single overloading. Plastic materials can generate a significant plastic zone at the crack which is shown to be well captured by the cohesive zone model approach.

In a cohesive zone model, fatigue crack growth involves the dissipation of separation energy released per cycle. The crack advance is defined by the total energy separation dissipated term equal to the critical energy release rate or toughness. The effect of varying toughness with the assumption that the critical traction remains fixed is investigated here. This study reveals that varying toughness does not significantly affect the stress distribution along the crack path. However, plastic energy dissipation can significantly increase with toughness.

A new methodology called the fast-track method is introduced to accelerate the simulation of fatigue crack growth. The method adopts an artificial material toughness. The basic idea of the proposed method is to decrease the number of cycle for computation by reducing the toughness. By establishing a functional relationship between the number of cycles and variable artificial toughness, the real number of cycles can be predicted. The proposed method is shown to be an excellent agreement with the numerical results for both constant amplitude loading and single overloading.

A new approach to predict fatigue crack growth curves is presented. The approach combines the fast-track method and an extrapolation methodology. The basic concept is to establish a function relationship using the curve fitting technique applied to data obtained from preliminary calculation of fast-track methodology. It is shown in this thesis that the new methodology provides excellent agreement with an empirical model. The methodology is limited to constant amplitude loading and small scale yielding conditions.

It is shown in the thesis that fatigue crack growth curves for variable amplitude loading can be predicted by using the data set for fatigue crack growth rate for constant amplitude loading. A retardation parameter can be deduced from the number of cycles delayed using the cohesive zone model. The retardation parameter is established by performing calculation for different toughness. This methodology is shown to give good agreement with results from empirical models for different variable amplitude loading conditions.

Declaration

No portion of the work referred to in this thesis has been submitted in support of an application for another degree or qualification of this or other university or institute of learning.

Copyright Statement

Dedication

To my parents, my wife: Trisfa Augia, and my children: Aliffa Hade, Ryan Hade and Faiz Hade.

Acknowledgement

I would like to express my deepest gratitude to my supervisor, Dr. Keith Davey for his excellent guidance, advice, patience and continuous support during my research. His constant enthusiasm and extraordinary insight have inspired me throughout my research.

I wish to thank my family for their unconditional support during these years and especially to my wife and my children for their love, patience and support. Their love provides my inspiration and is my driving force.

I would like to thank Dr. Daniele Colombo for the helpful discussions and tutorial about Code_Aster.

I am also grateful to The Indonesian Directorate General of Higher Education, Republic of Indonesia and Electrical De France (EDF) for the financial support and finite element package program support.

Nomenclature

a	Crack length
a_i	Crack size applied by constant amplitude loading in i^{th} cycle
a_o	Crack size applied by overloading
a_{o-1}	First crack size applied by overloading
a_{o-2}	Second crack size applied by overloading
$\underline{b}$	A body force
c	Specific thermal heat capacitance
$\dot{\Gamma}$	The rate of surface energy per unit length
δ	Separation
δ_n	Normal separation
δ_c	Critical separation
δ^e	Elastic displacement
δ^p	Plastic displacement
E	Modulus Elasticity
ε	Strain
$\dot{\varepsilon}^e$	The rate of elastic strain
$\dot{\varepsilon}^p$	The rate of plastic strain
G_I	The energy release rate
G_c	Toughness
κ	Crack irreversibility
K_I	Stress intensity factor mode I
K_o	Stress intensity factor due to overloading
K_i	Stress intensity factor due to constant amplitude loading in i^{th} cycle
ΔK	Stress intensity factor range

L_o, ℓ_o	Initial length
L_{cz}	Size of cohesive interface element
ν	Poison's ratio
$\dot{\Pi}$	The rate of potential energy system
đQ	The change of heat
$\underline{q}$	The heat flux
ρ	Density
r	Distance form crack tip
r_p	Radius of plastic zone
r_{po}	Crack tip plastic zone due to overloading
r_{pi}	Crack tip plastic zone due to constant amplitude loading
$\underline{\underline{\sigma}}$	Cauchy stress tensor
σ_c	Critical cohesive traction
σ_{xx}	Normal stress in x direction
σ_{yy}	Normal stress in y direction
σ_r	Normal stress in radian direction
σ_θ	Normal stress in θ direction
σ_Y	Yield stress
τ_{xy}	Shear stress in x and y direction
ϕ	Retardation factor
dS	The change of entropy
T	Temperature
$\dot{U}^e$	The rate of elastic strain energy
dU	The change of energy
dU_Ω	The change of energy in body
dU_{Γ_c}	The change of energy in boundary
U_Ω^{mech}, ω	Strain energy

U_{Γ_c}	Surface formation energy
đW	The change of work
$\dot{W}$	The rate work of external load
W_e	Strain energy per unit area
W_p	Plastic energy per unit area
W_s	Separation energy per unit area
W_d	Work done per unit area

List of Abbreviation

Ave	Average
CAL	Constant amplitude loading
FTM	Fast-track method
SOL	Single overloading ratio
OVL	Overloading
VAL	Variable amplitude loading

Chapter 1

Introduction

1.1. Background of Research

Fatigue is an important phenomenon in materials failure and can lead the catastrophic failure of engineering components. Fatigue failure is a mechanism that involves failure of materials caused by crack initiation and propagation. Factors that can affect the fatigue life of the structure can be mechanical, microstructural and environmental. The peculiarity of fatigue failure is that the driving force causing the failure is much smaller than the yield stress of the material. Fatigue and its modeling therefore remains a major concern for designers in many industries with regard to propagation. A fatigue model is needed to predict the rate of crack growth and how long it takes a crack to grow from its initial size to a permissible size after which catastrophic failure occurs.

The most widely used fatigue model applied to predict fatigue crack growth is the Paris model [1] and its modified version [2-5]. The model consists of a

phenomenological relation between the crack growth rate (da/dN) and the stress intensity factor range (ΔK). However, these models have limitation and need specific requirements to ensure them to be applicable such as a long crack must be initially present [6, 7], no blunting at the crack tip [8] and a nonlinear zone due to plasticity at the crack tip must be limited (small scale yielding) [6-8]. The Paris model does not describe the material failure caused by crack initiation.

An alternative approach commonly employed in fracture mechanics is the J-integral [9, 10] to characterize crack initiation under elastic-plastic loading condition. However, the approach is not applicable under reverse loading condition. The restriction on J-integrals to monotonic loading of non-linear dissipative materials is a major impediment to industrial analysis. Some recent progress in addressing this issue has been reported [11].

To overcome the limitation and disadvantages of the Paris model and other alternative approaches, the cohesive zone model can be employed to characterize the fatigue crack growth. The basic concept of the cohesive zone model was firstly introduced by Dugdale [12] who developed the concept that there are thin plastic zone ahead of crack tip and stress acting in the zone is limited by yield stress. Barenblatt [13] introduced the cohesive force on a molecular scale to cope the problem of equilibrium in an elastic material with crack. Hillerborg [14] proposed a maximum stress applied in model is the tensile strength. His model allowed the existing crack to initiate and propagate for brittle material.

In the cohesive zone model, the material failure can be viewed as a phenomenological model instead of an exact physical representation of material behaviour in the fracture process zone. The fracture proses zone is defined as the region ahead of the crack tip where the distribution of microcrack or void formation takes place [15]. In this region, material separation process can be described by a softening constitutive equation with a connection between the crack surface traction and the extent of material separation. Material separation in this way can be viewed as a result of material damage in the fracture process zone and interacts with the surrounding material.

To describe the material separation process, there are some important cohesive constitutive parameters these are a critical cohesive traction (σ_c), cohesive energy and a critical separation (δ_c). The damage of initiation is related to the critical cohesive traction. The critical cohesive traction is defined as the maximum stress which can be sustained in the crack tip area before the crack initiates. The crack propagation constrained by the relationship between the cohesive traction and material separation which is called the cohesive law, or the traction-separation law. In this law, the crack surface is completely open when cohesive traction is zero and critical separation is attained. Crack propagation also occurs when the cohesive energy is completely dissipated. In the cohesive zone model, the cohesive energy is defined as the area under traction-separation law well known as toughness in the case of linear elastic fracture mechanics.

The advantages of the cohesive zone model are its simplicity and ability to analyse crack initiation and fatigue crack propagation in one model. The combination of the cohesive zone model and finite element method does not need the re-meshing model to define crack propagation. In this current work, the cohesive zone model approach therefore is used to predict the fatigue crack growth in elastic-plastic materials.

1.2. Research Objective

The failure analysis under cyclic loading involves the slow degradation of material strength with accumulated damage. This degradation can be represented indirectly in the cohesive zone model by an evolution of stiffness and the critical cohesive traction. However the effect of slow degradation in the many thousands of loading cycles involved results in time consuming computation in predicting fatigue crack propagation. Therefore in this present research, a method is introduced to overcome this particularly drawback. The detailed objectives of the present works are

(a) The development of 1-D analytical theory describing the energy transfer required in the creating of new surface. The energy comprises the stored elastic energy and the separation energy. This model considers the transport equations for energy and entropy along with a cohesive zone model.

(b) The implementation of a cohesive zone model for constant amplitude loading and single overloading as well as to assess the effect of critical traction on retardation in fatigue crack growth.

(c) The assessment of local and remote stress distribution from the crack tip for various toughness values with fixed critical traction in a cohesive zone model. The elastic and plastic energy is also assessed for variable toughness.

(d) The development of a new methodology for the quick simulation of fatigue crack growth when subject to constant amplitude cyclic loading and single overloading. The proposed method is founded on the existence of a functional relationship between the number of cycles and various artificial toughness values. The artificial toughness is incorporated into a cohesive zone model that utilizes cohesive elements in the finite element method for the numerical simulation of material separation.

(e) The development of a new methodology for the prediction of fatigue crack growth by means of the fast-track method and an extrapolation methodology.

1.3. Research Contribution to Knowledge

In the present research, three main issues are considered that contribute to knowledge, i.e.

1. To give a new fundamental theory about the source of energy to create a new surface. The theory involves a combination of the strain energy stored and energy separation.
2. To give a new perspective to the energy criteria in the fatigue crack growth analysis by using the assumption that critical cohesive traction is fixed for varying artificial toughness values.

3. A new methodology is introduced to reduce computational analysis time in fatigue crack growth analysis. Time consumption is a big issue for the fatigue crack growth analysis especially for elastic-plastic materials with the finite element method. The idea of the method is to predict the many thousand cycles of fatigue crack growth by using the fewest numbers of cycles which result from the artificial toughness and extrapolation methodology.

1.4. Outline of Research

The framework of the current research can be explained as follows:

Chapter 1 provides the background of research which presents brief information about the disadvantages of some classical approaches on the fatigue crack growth prediction and introduces the alternative approaches i.e. the cohesive zone model. The objective of the present research and the research contribution of knowledge are explained in this section.

Chapter 2 reviews the existing literature about various approaches in fracture mechanics and fatigue crack growth i.e. the stress intensity factor, the energy criteria and the cohesive zone model. This information is essential to define the approach adopted in the present work i.e. the cohesive zone model.

Chapter 3 explains the basic theory of fracture mechanics i.e. the linear elastic and the linear elastic-plastic in fracture mechanics. The basic model for overloading is also is introduced in this section.

Chapter 4 describes 1-D analytical theory based on the transport equation for the energy balance in creating new surface. The theory is developed for linear elastic and elastic-plastic materials. In this chapter, the different point of view is exposed on how energy is supplied to the damage zone for the creation of new surface. To explain this mechanism, a practical demonstration in 1-D is presented.

Chapter 5 comprises the cohesive zone model formulation from Code_Aster and its implementation for constant amplitude loading and single overloading. The fatigue crack growth curve is provided and then the effect of critical cohesive traction for the fatigue crack growth rate by using the cohesive zone model due to the single overloading is presented in this section.

Chapter 6 presents the varying toughness approach with assumption that critical cohesive traction is fixed. The effect of varying toughness for fatigue crack growth and stress distribution along the crack path is shown. The functional relationship between varying toughness and number of cycles for same incremental crack length is also concerned. This phenomenon is investigated with an objective to reduce the number of cycles required for crack growth analysis. Since energy criteria can be used in crack growth analysis it is of interest therefore to examine the effect of varying toughness on elastic and plastic energy.

Chapter 7 explains an alternative methodology to predict fatigue crack growth. The fast-track methodology solution is introduced. This method is based on the existence of a functional relationship between the number of cycles and variable artificial toughness. The fast-track method is applied to simulate fatigue crack growth due to the constant amplitude loading and single overloading.

Chapter 8 presents a new methodology for the prediction of the fatigue crack growth curve based on an extrapolation methodology. The approach applies the combination of the fast-track method and an extrapolation methodology under the assumption of small scale yielding. The set of data obtained from the fast track-method is used to define parameters in an empirical model. The fatigue crack growth curve obtained from the new approach is compared with Forman empirical model and experimental results for the constant amplitude loading. This chapter also shows how the new approach captures fatigue crack growth retardation due to variable amplitude loading. The retardation parameter is defined by evaluating the fatigue crack growth retardation in the application of varying toughness using the cohesive zone model.

Chapter 9 consists of the general conclusion of the current work and recommendation for further work.

Chapter 2

Literature Review

2.1. Introduction

An understanding of the fatigue mechanism is an essential prerequisite for considering various aspects affecting the component life and crack growth. Knowledge of linear elastic materials, nonlinearity of materials and residual stress is important for fatigue life prediction. The fatigue life is commonly split into two phases i.e. crack initiation and a crack growth phase. The crack initiation phase usually involves microcrack growth and the crack growth phase principally supposed includes macrocrack growth.

2.2. Fatigue Crack Growth Prediction

The local stresses and strains near the crack tip commonly affect the fatigue crack growth process. A fracture mechanics principle often used local to the crack tip is the stress intensity factor. The stress intensity factor was firstly introduced by Irwin [16] to describe the stress intensity near the crack tip caused by remote applied loading.

The stress intensity factor is well defined for linear-elastic materials and its application fall under the field of Linear Elastic Fracture Mechanics (LEFM).

The use of the stress intensity factor in the fatigue crack growth prediction was firstly proposed by Paris and Erdogan [1]. The Paris law provides the phenomenological relation between the crack growth rate and the amplitude of the stress intensity factor range. However, a number of modifications to the original Paris law standard have been developed to take into account the load ratio (R) effect [3, 6], fracture toughness [3, 6], threshold limits and crack closure effects [5, 17]. The Paris law and its modified forms successfully describe experimental data under ideal conditions such as small scale yielding, constant amplitude loading and long cracks. However, when these conditions are not satisfied, the predictive capability of this approach diminishes [18].

The crack closure effect was first introduced by Elber [5, 17]. The concept takes account of crack closure due to the residual plastic deformation remaining in the wake of an advancing crack. The phenomena of crack closure may be described as follows: during loading, large tensile plastic strain is produced around the crack tip, which are not fully reversed upon unloading. The resulting compressive residual stresses act upon the crack surfaces and in the situation of zero applied loading induces crack closure. Upon tensile loading, energy is required to overcome the compressive stress. The crack closure concept can be accounted for with an effective stress intensity factor in the fatigue crack growth equation.

Numerous fatigue crack growth analyses have been developed to model the crack closure concept [18-28]. Newman [20, 21] proposed an analytical crack closure model applicable in plane stress and plane strain conditions. The model is founded on the Dugdale model, but differs in that is leaves plastically deformed material along the surface as the crack grows.

Unfortunately, most crack closure models are not easy to use and severe limitations in practice [29]. It is very difficult to conventionally measure the displacement histories at a midsection of a thick specimen for example as required in some models Also the lack of the accuracy in the analytical model arises because a numbers of crucial assumptions are required to simplify the material model.

The alternative analysis of fatigue crack growth is based on an energy criterion. In brittle materials, it is recognized that the strain energy change should be sufficient to overcome the surface energy of materials [30]. It is also stated that the crack driving force should overcome the crack resistance of materials. This means that the energy for crack growth is supplied from existing elastic strain energy of materials which gives rise to the strain energy release rate (G). Although the strain energy release rate can be calculated directly with crack movement, the more popular are indirect approaches found on J-integral [9, 10]. However, the major problem of J-integral is its restriction to monotonic loading of non-linear dissipative materials. Some current progress in addressing this issue has been reported [9].

In the ductile material, Rice [10] introduced a plastic dissipation criterion to analyse fatigue crack growth. Plastically dissipated energy can be directly related to the accumulation of plastic strain. Plastic deformation is related to dislocation motion, which is also associated with fatigue. The plastic energy dissipation rate can also be defined as ductile tearing resistance [31, 32]. Thus, the rate of plastic energy dissipated per cycle in the reversed plastic region can used to predict the fatigue crack growth [33-37]. Cojocaru and Karlsson [38] proposed a concept based on the fatigue crack growth by cyclic material degradation in the process zone at the crack tip. The degradation of the material is accompanied by significant plastic deformation. Therefore, the plastically dissipated energy in the crack-tip may be used to evaluate the crack growth.

2.3. Cohesive Zone Model

A recent approach for fatigue crack growth is known as a cohesive zone model. This approach takes a different point of view for the crack tip stress and strain fields. A principal motivation in the cohesive zone model is to circumvent the unrealistic stress singularity at the crack tip. In this approach the essential physics of fatigue crack growth may be captured. The basic concept of the cohesive zone model was proposed Barenblatt [13] who assume that failure would occur with the separation of the upper and lower surfaces of a zero volume cohesive zone ahead of the crack tip.

In the cohesive zone model, the separation of the two surfaces which bound on the cohesive process zone is determined by a cohesive traction law where material

failure is controlled by quantities such as displacements jump or separation and cohesive traction. Crack growth occurs when the separation of the crack tip reaches a critical value at which the cohesive traction vanishes.

Structures subject to cyclic loading are affected by the slow degradation of material ahead of a crack. This degradation can be represented indirectly in the cohesive zone model by an evolution of stiffness and critical normal traction (σ_c). The material degradation that needs to be considered for damage accumulation should be path-dependent in the process of separation [11]. Camacho and Ortiz [39] proposed an irreversible cohesive law for the weakening of cohesive strength with increasing crack opening. Roe and Siegmund [40] introduced a damage evolution law in terms of the accumulated separation into the cohesive zone model. Haodon Jiang [41] proposed that the irreversibility is incorporated into the constitutive law with consideration of: (a) specific loading and unloading path; (b) accumulation of damage under subcritical cyclic loading; and (c) compression or normal surface contact behavior. The current cohesive tractions are determined by the current amount of damage as well as by the current separation. The constitutive laws are therefore history dependent and a gradual degradation of the cohesive properties under cyclic loading is reflected in the process zone ahead of the crack tip.

The relationship between plastic strain gradient to material separation processes, crack closure and the resulting crack growth rate has been studied by Brinkmann [42]. His fatigue crack simulation incorporates a strain dependent plasticity model and an irreversible cohesive zone model. Combination of cohesive element and the

specific elastic-plastic law which is used to investigate the crack closure phenomena was introduced by [43]. A modified strip yield model with assumption of crack growth is proportional to the cyclic crack tip opening displacement.

Since the traction-separation law plays major role in the cohesive zone model, the measuring of the traction-separation law is an important issue in the cohesive zone model. The most procedure measures the curve obtained from an experiment. However, the experimental results have shown some major shortcomings [8] .i.e.

1. The cohesive zone position is very difficult to be determined for uncrack specimen and also multiple cracks may occur in arbitrary location due to heterogeneity and certain materials undergo large plastic zone before cohesive crack forms.
2. For a small cracked specimen, asymmetric model of fracture occurs ad crack opening is not uniform across the specimen.

An alternative method is introduced to determine the traction-separation curve. This method utilizes indirect methods by means of the parametric fitting of experimental results. This method is known as inverse analysis or data reduction. However this methodology commonly does not provide identical results for same given materials [8].

2.4. Overloading

Many structures are occasionally subject to overload during the service. Fatigue crack growth rate is well known to be decelerated by the application of overloads

despite causing an initial increase of the crack growth rate. This initial increase is followed by a fast decrease before finally returning to steady state crack propagation. The cause is usually attributed to plasticity induced crack closure, strain hardening, and crack tip blunting [44, 45]. The plastic zone is considered to be of major importance as a reduction factor contributing to the crack growth retardation behavior due to overload [46]. Increased overload can provide larger retardation effects in crack growth because the plastic zone size around the crack tip tends to be proportional to the overload ratio [46].

Wheeler [47] suggested that residual compressive stresses can retard post-overload crack growth. Huang Xiaoping [48] introduced a modified Wheeler model incorporating an improved fatigue crack growth rate equation and the concept of equivalent stress intensity factor range. Harmain [49] proposed several modifications to Wheeler's growth idea which incorporate a consideration involving effective stress intensity factor based on an Elber's concept of crack closure [17], the relationship between overload ratio and the Wheeler's exponent, and fatigue growth rate calculation. Pavlou [50] developed a model that consider the influence of the yield stress changes within the overload plastic zone on the fatigue crack growth rate. This approach is based on strain-hardening fatigue mechanism in the plastic zone that takes place during all the fatigue life stages.

In the cohesive zone approach, Siegmund [51] studied an irreversible cohesive zone model for fatigue crack growth simulation. The model is applied to study transient

fatigue failure. Single overload cases are computed to demonstrate the effect of variations in the cohesive zone properties.

Ural [6] introduced a damage model that has three material parameters i.e. the rate of damage accumulation, the threshold value for accumulation of damage, and the rate of crack retardation. The model was applied to predict crack retardation due to a single peak overload. He postulated that residual stress in the very large plastic zone can cause the crack retardation. In this phenomenon was adequately captured by a plasticity model in the bulk material.

However, slow degradation in the many thousands of loading cycles commonly affect time consuming computation in predicting fatigue crack propagation especially for elastic-plastic material. Therefore in this present research, an alternative methodology is introduced to overcome this particularly drawback in computation.

2.5. Probabilistic and Statistical Prediction Fatigue Crack Growth

As mentioned in the previous section, the fatigue crack growth rate (da/dN) can be expressed as a function of crack-tip stress intensity factor range (ΔK). This function is mostly utilized to exam the fatigue life of important mechanical components. Some fatigue crack growth models have been developed on the basis of Paris law [1] and several of its modified models [2-5]. However, since fatigue crack growth is significantly affected by some special factors such as the environment [52], stress ratio [53], and loading history [54], there have scatter data for the rate of fatigue

crack growth. This has given rise to a number of fatigue crack growth prediction models based on probabilistic and statistical approaches. These approaches have been proposed and developed to evaluate the variability in fatigue crack growth examples of which are the Markov chain model [55, 56], the exponential model [57, 58] and the polynomial model [56]. Since these models are probabilistic and statistical analysis in nature. They require experimental data to determine key parameter.

Chapter 3

Theoretical Review of Fracture Mechanics

3.1. Introduction

In engineering components subjected to cyclic loading, a fatigue crack can be initiated on a microscopically small scale, followed by crack growth to macroscopic size, eventually leading to failure. Understanding the fatigue mechanism is an essential prerequisite in understanding which parameter affects fatigue life and fatigue crack growth.

This chapter explains the basic theory of fracture mechanics i.e. crack initiation, crack growth, the linear elastic and the linear elastic plastic in fracture mechanics. The basic model of overloading also is introduced in this section.

3.2. Crack initiation

Fatigue initiation occurs as consequence of cyclic slip due to dislocation movement where cyclic slip requires a cyclic shear stress. For the microscopically small scale, the cyclic shear stress is not homogeneously distributed throughout the material. The shear stress on crystallographic slip planes differs from grain to grain, depending on the size and shape of grains, crystallographic orientation of the grain, and elastic anisotrophy of the materials. In grains at the surface slip occurs at grain which are more beneficial for cyclic slip than in other surface grains. If slip occurs in a grain, a slip step will be formed at the material surface as shown in Figure 3.1a. If the load increases, then strain hardening will occur in a slip band. As a consequence, for unloading, larger shear stress will be present on the same slip band, but now in the reversed direction as shown in Figure 3.1b. The same sequence of events can occur in the second cycle see Figure 3.1c and d.

In practical situation, an inhomogeneous stress distribution can occur due to a notch effect of a hole or some other geometric discontinuity. Inhomogeneous stress distributions lead to a peak stresses at surfaces (stress concentration). Furthermore, surface roughnesses can also encourage crack initiation at the materials surface. Fatigue in the crack initiation phase is essentially a surface phenomenon and is very sensitive to various surface conditions e.g. surface roughness.

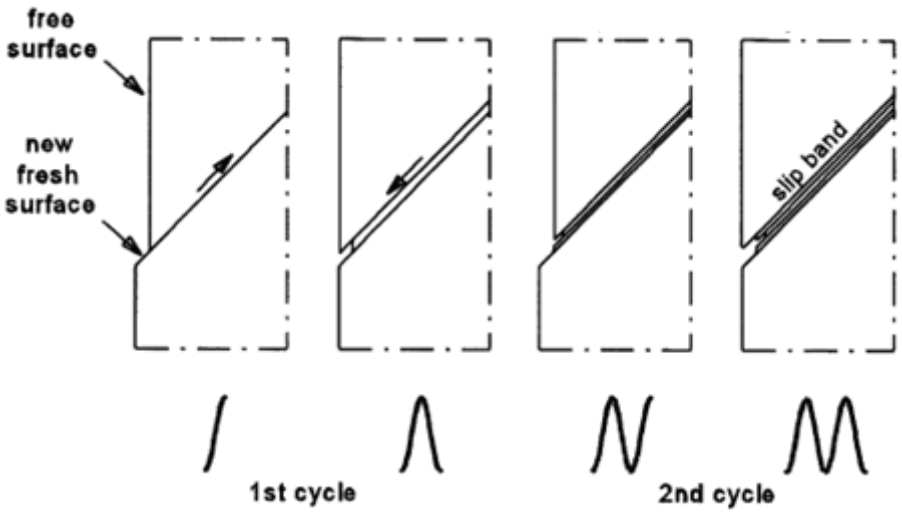

(a) (b) (c) (d)

Figure 3.1 Cyclic slip leads to nucleation [59]

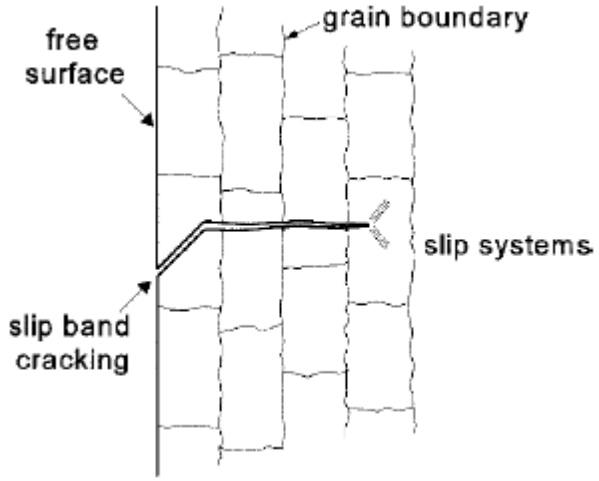

Figure 3.2 Cross section of microcrak [59]

3.3. Crack growth

Microcracks contribute to loaded stress inhomogeneity due to a stress concentration at the tip of the microcrack. This can result in the situation of a slip system. Furthermore a crack propagates into material, the slip displacements can be retarded

as consequence adjacent grain and different slip orientation. It is also the slip displacement will slip by more than one slip plane. Then the microcrack growth will deviate from initially direction. However, in general, the microcrack growth direction tends to be perpendicular to loading direction as show in Figure 3.2.

The crack growth rate decreases as the crack tip approaches a grain boundary, although after penetrating the grain boundary, the crack growth rate increases after passing through grain boundary the crack growth rate will increase steadily, as illustrated in Figure 3.3

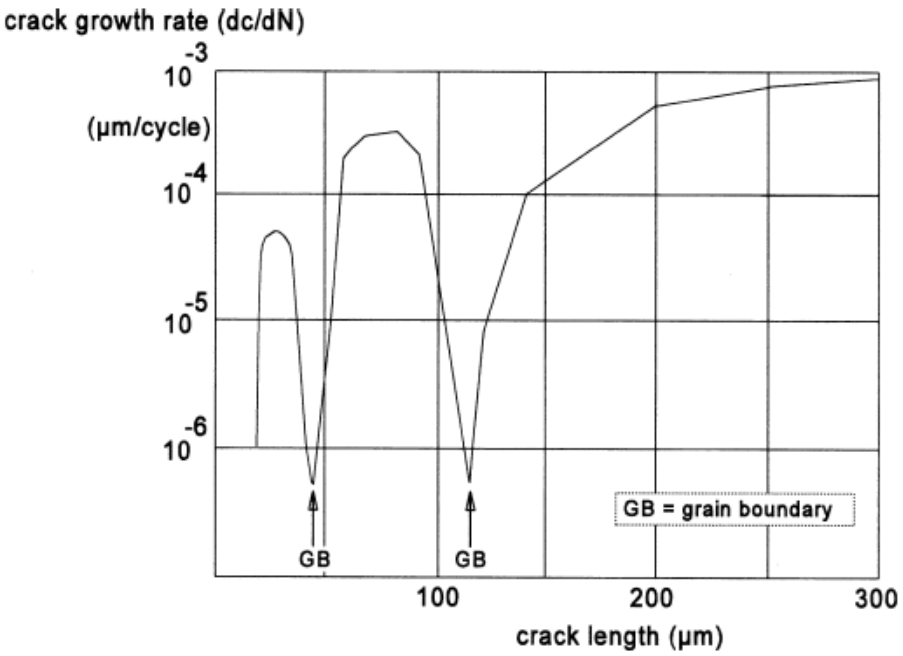

Figure 3.3 Grain boundary effect on crack growth in Al-alloy [59]

3.4. Linear Elastic Crack Tip Stress Field

A crack loading can be divided into three different modes. Each mode involves different crack surface displacement as shown in Figure 3.4. Mode I is defined to be the mode when displacement of crack surfaces is perpendicular to the plane of the crack. Mode II is the in-plane sliding mode in which displacement of the crack surfaces is in the plane of the crack and perpendicular to the leading edge of the crack. Mode III is the tearing mode which is caused by out of plane shear. The displacement involved in this mode is surface in the plane of the crack and parallel to the leading edge of the crack.

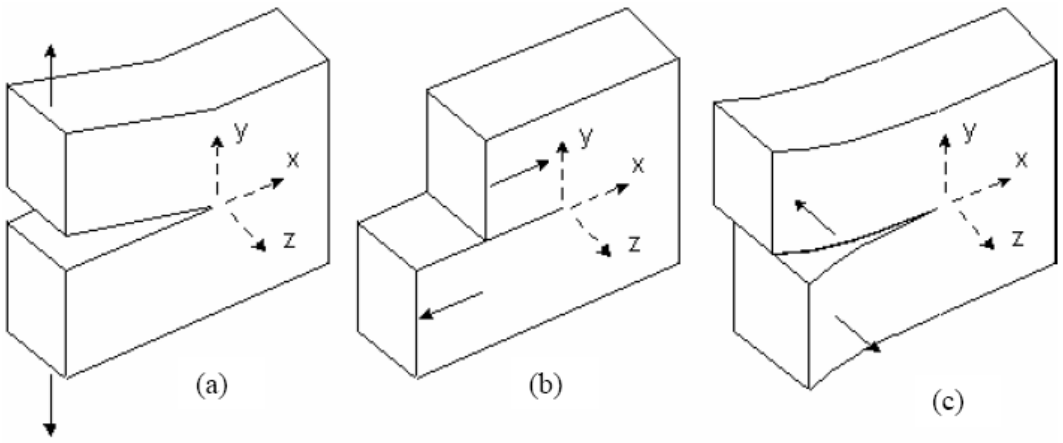

Figure 3.4 Three modes of crack: (a) Opening mode (Mode I),
(b) Sliding mode (Mode II) and (c) Tearing mode (Mode III)

The present study is only concerned with Mode I fracture, because this is recognized as the dominant mode in fracture mechanics [60]. Therefore, only Mode I stress crack-length relations will be presented. Following the notation presented in Figure 3.5, the crack tip stresses can be express as

$$\sigma_{xx} = \frac{K_I}{\sqrt{2\pi r}} \cos\frac{\theta}{2}\left[1 - \sin\frac{\theta}{2}\sin\frac{3\theta}{2}\right] + O\left(\sqrt{r}\right)$$

$$\sigma_{yy} = \frac{K_I}{\sqrt{2\pi r}} \cos\frac{\theta}{2}\left[1 + \sin\frac{\theta}{2}\sin\frac{3\theta}{2}\right] + O\left(\sqrt{r}\right) \qquad (3.1)$$

$$\tau_{xy} = \frac{K_I}{\sqrt{2\pi r}} \sin\frac{\theta}{2}\cos\frac{\theta}{2}\cos\frac{3\theta}{2} + O\left(\sqrt{r}\right)$$

as $r \to 0$.

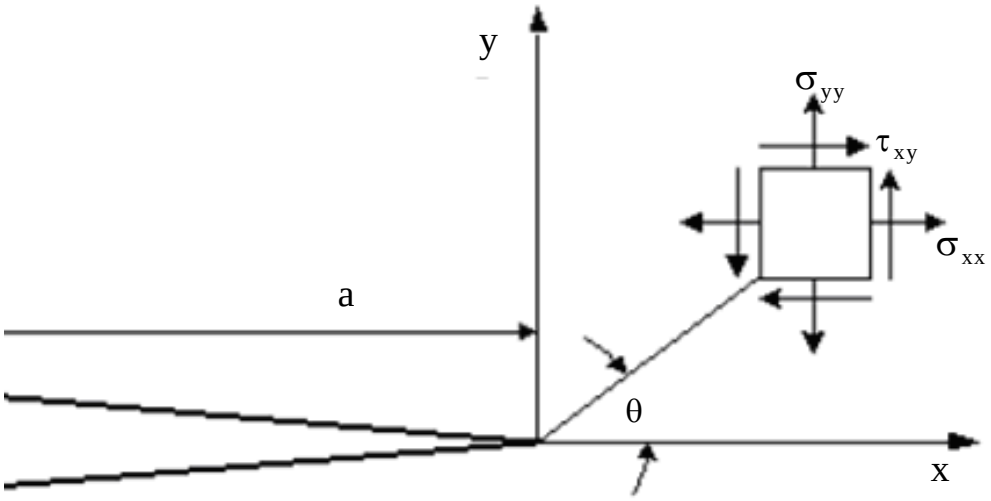

Figure 3.5 Coordinate system and stresses at near crack-tip field

The stress field around the crack tips, which is represented in Equation (3.1), depends on distance from the crack tip r and angle θ only for given value of K_I. K_I is defined as the stress intensity factor for Mode I and can be expressed by the following equation:

$$K_I = \beta\sigma_o\sqrt{\pi a} \qquad (3.2)$$

where σ_o is the remote applied stress, a is the crack length and β is a dimensionless factor which depends on crack length and component geometry. The stress intensity factor provides a unique measure of the intensity of stress within an annular zone ahead of the crack tip under linear conditions.

In polar coordinate, singular components of stress can be expressed as

$$\sigma_r = \frac{K_I}{\sqrt{2\pi r}}\left[\frac{5}{4}\cos\frac{\theta}{2} - \frac{1}{4}\cos\frac{3\theta}{2}\right] + O\left(\sqrt{r}\right)$$

$$\sigma_\theta = \frac{K_I}{\sqrt{2\pi r}}\left[\frac{3}{4}\cos\frac{\theta}{2} + \frac{1}{4}\cos\frac{3\theta}{2}\right] + O\left(\sqrt{r}\right) \qquad (3.3)$$

$$\tau_{r\theta} = \frac{K_I}{\sqrt{2\pi r}}\left[\frac{1}{4}\sin\frac{\theta}{2} + \frac{1}{4}\sin\frac{3\theta}{2}\right] + O\left(\sqrt{r}\right)$$

as $r \to 0$, and for the principal singular stress

$$\sigma_1 = \frac{K_I}{\sqrt{2\pi r}}\cos\frac{\theta}{2}\left[1 + \sin\frac{\theta}{2}\right] + O\left(\sqrt{r}\right) \qquad (3.4)$$

$$\sigma_2 = \frac{K_I}{\sqrt{2\pi r}}\cos\frac{\theta}{2}\left[1 - \sin\frac{\theta}{2}\right] + O\left(\sqrt{r}\right)$$

as $r \to 0$.

3.5. Elastic-Plastic Crack Tip Stress Field

In linear elastic fracture mechanics, the amount of inelastic deformation at the crack tip is assumed negligible. However in most practical cases, there is some degree of plasticity at the crack tip, which can be extensive in the case of ductile materials.

3.5.1 Crack Tip Plastic Zone Size

The stress field around the crack tip in Equation (3.1) is proportional to $r^{-1/2}$. This means that at the crack tip stress field become infinite as $r \to 0$. In reality this is unrealistic, the material will plastically deform near the crack tip. As a result stresses are lowered to a first approximation to the level of the yield strength of material as shown in Figure 3.6.

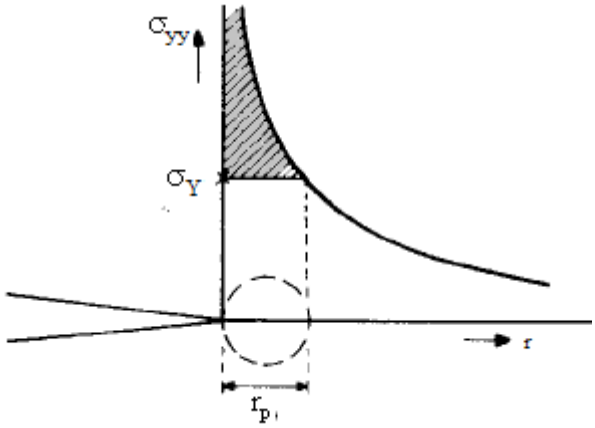

Figure 3.6 Crack tip zone under small scale yielding condition [60]

The stress intensity factor can still be used to characterize crack growth under the small-scale yielding conditions. This condition requires that the crack tip zone of inelastic deformation be confined well inside the region of K-dominance i.e. where Equation (3.1) provides a reasonable approximation.

Plastic zone length r_p ahead of crack can be calculated by means of substitution of Equation (3.4) into the von Mises yield criteria. The estimation of plastic zone can be written in terms of

$$r_p(\theta) = \frac{1}{4\pi}\left(\frac{K_I}{\sigma_Y}\right)^2\left[\frac{3}{2}\sin^2\theta + 1 + \cos\theta\right] \tag{3.5}$$

for plane stress and

$$r_p(\theta) = \frac{1}{4\pi}\left(\frac{K_I}{\sigma_Y}\right)^2\left[\frac{3}{2}\sin^2\theta + (1-2\nu)^2(1+\cos\theta)\right] \tag{3.6}$$

for plane strain.

The plastic zone along the crack axis $(\theta = 0)$ and $\nu = 1/3$ is given by

$$r_p(0) = \frac{1}{2\pi}\left(\frac{K_I}{\sigma_Y}\right)^2 \tag{3.7}$$

for plane stress and

$$r_p(0) = \frac{1}{18\pi}\left(\frac{K_I}{\sigma_Y}\right)^2 \tag{3.8}$$

for plane strain.

3.5.2 The Irwin Approximation

Plastic zone length r_p ahead of the crack tip was also introduced by Irwin [61] who considered the plastic zone to be of circular shape. He postulated that the plasticity affected to make the crack behave as if it were longer than its physical size. Thus, as a consequence of crack tip plasticity is that displacement at the crack surfaces is larger and the stiffness is lower than in the elastic case. In Irwin's model, the size of plastic zone r_p is twice as large as the first estimate provided by Equation (3.7), i.e.

$$r_p(0) = \frac{1}{\pi}\left(\frac{K_I}{\sigma_Y}\right)^2 \tag{3.9}$$

for plane stress. Small scale yielding is assumed to apply if $r_p << a$ where a is crack length.

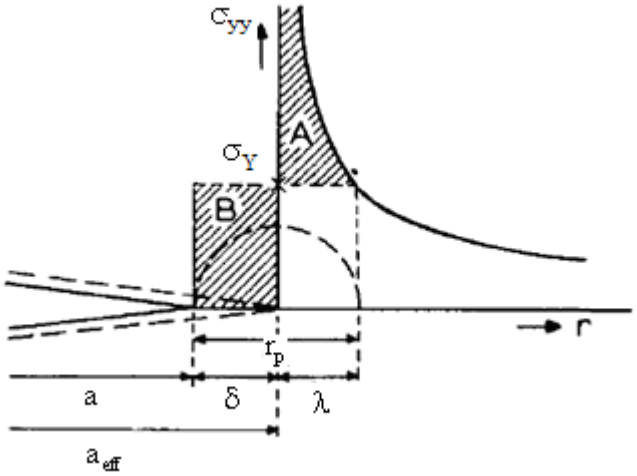

Figure 3.7 Crack tip zone for Irwin Approximation [60]

3.5.3 The Dugdale Approximation

An alternative approach was introduced by Dugdale [12] to determine the plastic zone length. He considered an effective crack length which is larger than the physical size as shown in Figure 3.8. The crack edges in front of the physical crack tip carry out the yield stress (σ_Y) on tend to close the crack. The additional length L_ρ can be determined by means of:

$$L_\rho = \frac{\pi}{8}\left(\frac{K_I}{\sigma_Y}\right)^2 \tag{3.10}$$

This result can be compared with Equation (3.9), it is apparently that both equations are quite similar i.e.

$$r_p = 0.318\left(\frac{K_I}{\sigma_Y}\right)^2 \qquad \text{and} \qquad L_\rho = 0.393\left(\frac{K_I}{\sigma_Y}\right)^2$$

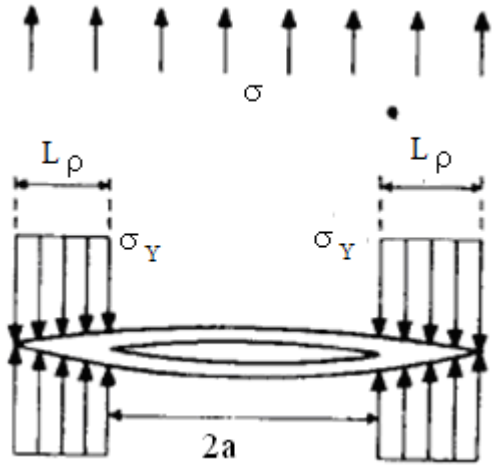

Figure 3.8 Dugdale Approximation [60]

3.6. Effect of Overloading

Many engineering structures are subject to complex fluctuating loads during service. Research has been undertaken in understanding the effect of variation in amplitude of cyclic loading. This research [62] showed that the fatigue life of a component is significantly affected by variable amplitude load fluctuation. A thorough understanding of the effect of various variables on fatigue crack initiation and propagation under variable amplitude load fluctuation is essential to the development of accurate prediction methods of fatigue life of engineering structures.

Somewhat surprisingly, the application of overload can cause crack growth rates to be much less than without the application of overload, as illustrated in Figure 3.9. It is apparent that a high to low load sequence provide a longer crack growth life than it

would have been predicted on the basis of the summation of crack growth for each cycle using constant amplitude cycle.

The amount of retardation increases as the overloading ratio to the level of subsequent loading increases. In fact, if the overload ratio is large enough, the crack growth can arrest, with the ratio depending on material, geometry etc. Crack retardation tends to increase if several consecutive overloads are applied periodically instead of a single overload. However, application of too many consecutive overloads will cause growth itself that counteracts any gains in life due to retardation. Finally, retardation is more pronounced in thinner sections and is reduced in thicker sections or for higher yield strength alloys.

The overloading causes a large plastic zone as shown in Figure 3.10a. The material in this zone is plastically deformation. After unloading condition, this zone remains to fit in the surrounding elastic materials. The elastic materials back to its original condition. This cause the elastic materials will employ compressive stress on plastic zone at the crack tip and also result residual stress as shown in Figure 3.10b.

Whilst a tensile overload can extend the crack growth life, a large compressive load can have the opposite effect. However, increases in growth rate following compressive overload are much smaller than retardation caused by tensile overload of the same value. Moreover, if the tensile overload is followed immediately by compressive overloads, then crack growth retardation will be diminished.

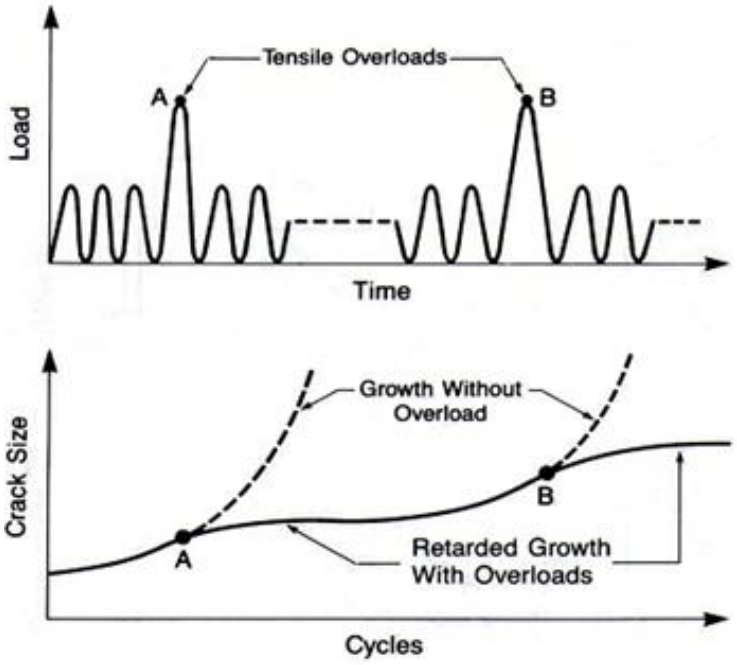

Figure 3.9 Schematic of crack retardation effect [63]

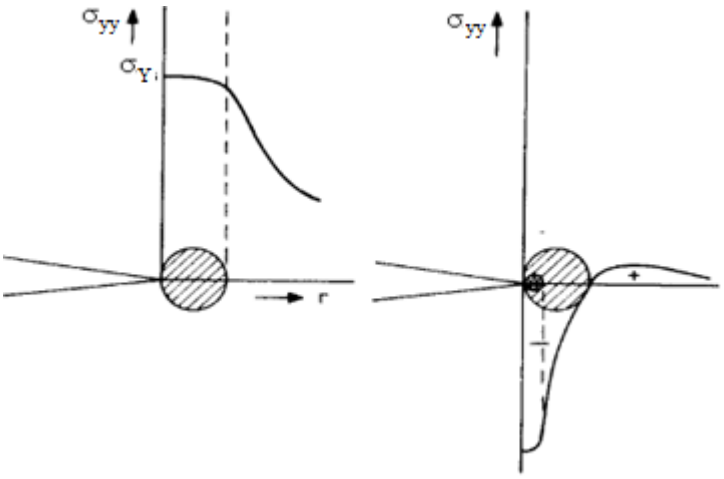

(a) Overload (b) after overload

Figure 3.10 Residual compressive stress ahead of crack tip [60]

3.6.1 Retardation Models

A retardation model was proposed by Wheeler [47] who introduced a retardation parameter (ϕ) denoted as the ratio of the current plastic zone size to the size of the plastic enclave formed on overload as shown in Figure 3.11a. An overload occurring at the crack size, (a_0) leads to plastic zone around the crack tip. The size of plastic zone can be determined by means of

$$r_{po} = C_1 \frac{S_o^2 a_o}{\sigma_Y^2} = C \frac{K_o^2}{\sigma_Y^2} \tag{3.11}$$

where S_o and K_o are the applied stress and the stress intensity factor in overload stress, respectively. σ_Y is the yield stress. C_1 and C are the constant parameter. When the crack growth to a length (a_i), the current plastic zone size will be

$$r_{pi} = C_1 \frac{S_i^2 a_i}{\sigma_Y^2} = C \frac{K_i^2}{\sigma_Y^2} \tag{3.12}$$

where S_i and K_i are the stress and the stress intensity factor in the *i* th cycle, respectively. C_1 and C are the constant parameter. If the subsequent plastic zone remain embedded in the plastic enclave (a distance λ in front of the current crack (a_i)), then retardation factor (ϕ) introduced by Wheeler is assumed to be dependent on the ratio r_{pi}/λ. Since from Figure 3.8 $\lambda = a_0 + r_{po} - a_i$ these assumption amounts to

$$\left(\frac{da}{dN}\right)_{retarded} = \phi \left(\frac{da}{dN}\right)_{linear} = \phi f(\Delta K) \tag{3.13}$$

with $\phi = \left(r_{pi}/\left(a_o + r_{po} - a_i\right)\right)^m$ as long as $a_i + r_{pi} < a_o + r_{po}$. If $a_i + r_{pi} > a_o + r_{po}$ then the crack has passed through the overload plastic zone and the retardation factor $\phi = 1$.

For the case of a single overload in constant amplitude the retardation factor gradually decreases to unity while the crack growth progresses through the plastic enclave. If a second higher load occurs, producing a plastic zone extending beyond the border of existing plastic enclave, the boundary of this new plastic zone is used in the equation as illustrated in Figure 3.11b.

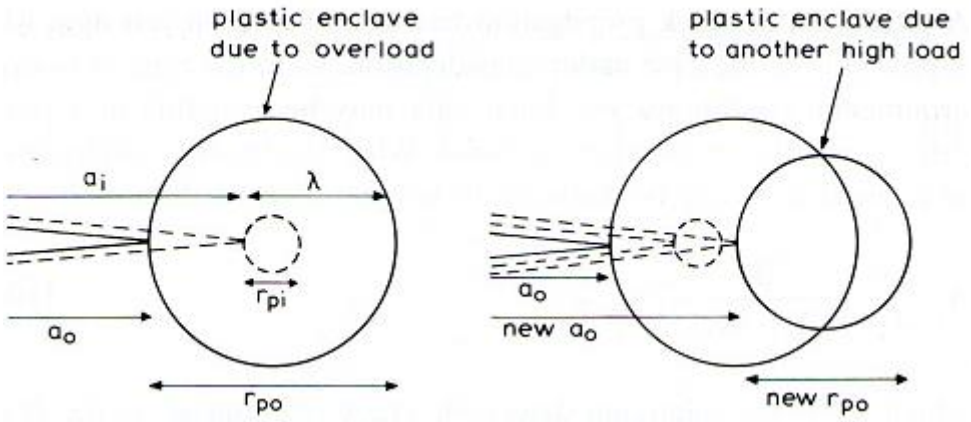

a. situation after overload b. situation after second overload

Figure 3.11 Wheeler's model [47]

A modified Wheeler's model was introduced by [64] who incorporated a plastic zone correction factor $\left(\lambda_p\right)$ in the expression for instantaneous cycle plane stress plastic i.e.

$$r_{pi} = \lambda_p \left(\frac{1}{\pi}\right)\left(\frac{\Delta K}{2\sigma_Y}\right)^2 \qquad (3.14)$$

The retardation factor ϕ can be expressed as

$$\phi = \left(\frac{\lambda r_{pi}}{\left[a_{o1} + r_{po} - a_i \right]} \right)^m = \gamma \left[\frac{r_{pi}}{\left(a_{o1} + r_{po} - a_i \right)} \right]^m \tag{3.15}$$

Where $\gamma = \lambda_p^m$ is a correction factor.

3.7. Energy Balance for Crack Growth

An energy balance criteria can be established for crack growth by considering energy release rate that occurs on the underloading of materials. Griffith [30] proposed an energy criterion for the failure of brittle materials. He proposed that surface energy must be supplied in order to create new crack surfaces. This approach can be expressed as

$$G = \dot{W} - \dot{U}^e = \dot{\Gamma} = 2\gamma A \tag{3.16}$$

where $\dot{W}$ is the rate work of external load, $\dot{U}^e$ is the rate of elastic strain energy of the cracked body and $\dot{\Gamma}$ is the rate of energy per unit time spent in increasing the crack area. Additional energy is needed for crack growth in ductile materials when compared to brittle materials to account for the plastic energy dissipated during the fracture process. An energy balance of the following form

$$\dot{W} = \dot{U}^e + \dot{U}^p + \dot{\Gamma} \tag{3.17}$$

where $\dot{U}^p$ is the rate of dissipated energy due to plastic deformation. Equation.(3.17) can be expressed as

$$-\dot{\Pi} = \dot{U}^p + \dot{\Gamma} \tag{3.18}$$

where $\dot{\Pi} = \dot{U}^e - \dot{W}$ is the rate of potential energy system. Equation (3.18) shows that the rate of potential energy decrease during crack growth is equal to rate of energy dissipated in plastic deformation and surface formation.

An energy and stress field approach at the crack tip for elastic fracture mechanics are equivalent. This means the relationship between the energy release rate (G_I) and the stress intensity factor (K_I) is unique and is of the form

$$G_I = \frac{K_I^2}{E} \tag{3.19}$$

for plane stress

$$G_I = \frac{\left(1-\upsilon^2\right)K_I^2}{E} \tag{3.20}$$

for plain strain, where E is Young's modulus and υ is Poisson ratio.

Chapter 4

Energy Driven Force in Fracture Mechanics

4.1. Introduction

A crack requires energy to growth supplied by the applied loading. Griffith [30] firstly introduced for brittle materials that the work of separation per unit area required to create two surface should be supplied from the strain energy release rate In ductile materials, Rice [9] proposed the plastic dissipation criteria for fatigue crack growth. The rate of plastic energy dissipated per cycle can be used to predict the fatigue crack growth [34, 38, 65]. Cojocaru and Karlsson [34] proposed the concept based on the fatigue crack growth by cyclic material degradation in the process zone at the crack tip. The degradation of the material is accompanied by significant plastic deformation. Therefore, the plastically dissipated energy in the crack-tip may be used to evaluate crack growth. However, the fundamental relation between plastic energy dissipation during damage process for an elastic plastic material and crack growth may be not clearly found.

A recent innovation has revealed more general forms of energy balance. Mechanical-energy based transport equations for moving frames have recently been formalised for materials possessing univariate entropy. These can be applied to fracture and plasticity and also be employed with a cohesive zone model, which hitherto has remained impossible.

In the present study, a new approach is presented using the cohesive element approach in combination with transport equations, control volume and thermodynamic laws. 1-D analytical theory underpinned by transport equation for energy balance in creating new surface is highlighted here. The theory is developed for linear elastic and elastic-plastic materials by using the cohesive element approach. The method demonstrates how energy are supplied and dissipated in the damage zone for the creation of new surface. The process of energy transfer is presented numerical by means of practical demonstration. The relationship between artificial toughness and energy transport is established in this chapter.

4.2. General Transport Forms

The first law $dU = đQ + đW$ in transport form is

$$\frac{D^*}{D^*t}\int_\Omega \rho u dV + \int_\Gamma \rho u\left(\underline{v} - \underline{v}^*\right)\cdot \underline{n} d\Gamma = -\int_\Gamma \underline{q}\cdot\underline{n} d\Gamma + \int_\Omega \rho Q dV + \int_\Gamma \underline{v}\cdot\underline{\underline{\sigma}}\cdot\underline{n} d\Gamma + \int_\Omega \rho \underline{v}\cdot\underline{b} dV \quad (4.1)$$

where u is stationary internal energy per unit mass, $\underline{q}\cdot\underline{n}$ is heat flux, Q represents a heat source, $\underline{\underline{\sigma}}$ is the Cauchy stress tensor and $\underline{b}$ is a body force. The derivative

D^*/D^*t is not common to the literature but plays a crucial role in formularising a rigorous foundation for transport theory and their correct application to discontinuous physics. The use of D^*/D^*t rather than the ordinary derivative d/dt in Equation (4.1) even though these are identical when applied to a function of t. The use of the derivative D^*/D^*t in these equations is intended to immediately relay the notion that Ω is a control volume transported through $\underline{v}^*$.

A general transport equation form is

$$\frac{D^*}{D^*t}\int_\Omega \rho\psi dV + \int_\Gamma \rho\psi\left(\underline{v}-\underline{v}^*\right)\cdot\underline{n}d\Gamma = -\int_\Gamma \underline{J}\cdot\underline{n}d\Gamma + \int_\Omega \rho b dV \tag{4.2}$$

which has a weighted equivalent

$$\frac{D^*}{D^*t}\int_\Omega W\rho\psi dV + \int_\Gamma W\rho\psi\left(\underline{v}-\underline{v}^*\right)\cdot\underline{n}d\Gamma - \int_\Omega \rho\psi\left(\underline{v}-\underline{v}^*\right)\cdot\nabla W dV =$$

$$= -\int_\Gamma W\underline{J}\cdot\underline{n}d\Gamma + \int_\Omega \nabla W\cdot\underline{J}dV + \int_\Omega \rho W b dV \tag{4.3}$$

where W is transported invariantly with Ω, i.e. $D^*W/D^*t = 0$ although if W were not invariant, then the term $\int_\Omega D^*W/D^*t\,\rho\psi dV$, is required to be subtracted from the left hand side of equation (4.3). Setting $W = T^{-1}$ (for example) in Equation (4.3) applied to Equation (4.1) gives

$$\frac{D^*}{D^*t}\int_\Omega \frac{\rho u}{T}dV - \int_\Omega \frac{D^*T^{-1}}{D^*t}\rho u dV + \int_\Gamma \frac{\rho u}{T}\left(\underline{v}-\underline{v}^*\right)\cdot\underline{n}d\Gamma - \int_\Omega \frac{\rho u}{T}\left(\underline{v}-\underline{v}^*\right)\cdot\nabla\left(\frac{1}{T}\right)dV =$$

$$= -\int_\Gamma \frac{\underline{q}\cdot\underline{n}}{T}d\Gamma + \int_\Omega \frac{\rho Q}{T}dV + \int_\Gamma \frac{\underline{v}\cdot\underline{\underline{\sigma}}\cdot\underline{n}}{T}d\Gamma - \int_\Omega \underline{v}\cdot\underline{\underline{\sigma}}\cdot\nabla\left(\frac{1}{T}\right)dV + \int_\Omega \frac{\rho\underline{v}\cdot\underline{b}}{T}dV + \int_\Omega \underline{q}\cdot\nabla\left(\frac{1}{T}\right)dV$$

(4.4)

4.3. Entropy Transport Equation for Plastic Deformation: Reversible Approach

Consider a reversible increment in heat supply and work to give

$$dU = đQ_R + đW_R = TdS + đW_R \tag{4.5}$$

where it is assumed here that there exists a reversible process (axiomatic to classical thermodynamics), so that the increment in internal energy matches that arising from the first law above. Equation (4.5) provides a relationship between state variables and has wide validity although only strictly applicable at stable equilibrium conditions, albeit readily extended to local equilibrium.

Prior to the substitution of (4.5) into the first law it is prudent to explore whether a reversible process does in fact exist to facilitate this. The work on a continuum element subject to a stress state σ_{ij} is $đW = \sigma_{ij}\dot{\varepsilon}_{ij}dtdV$ where dV refers to an elemental volume of material. Assume the additive decomposition

$$đW = \sigma_{ij}\dot{\varepsilon}_{ij}dtdV = \sigma_{ij}\dot{\varepsilon}^p_{ij}dtdV + \sigma_{ij}\dot{\varepsilon}^e_{ij}dtdV = đW^p + đW^e \tag{4.6}$$

where it is further assumed that elastic deformation is reversible, i.e. $đW^R = \sigma_{ij}\dot{\varepsilon}^e_{ij}dtdV = đW^e$ (this assertion is revisited at a later date) and plastic deformation $đW^p$ is thermally dissipative (i.e. any increase in material dislocation potential is assumed negligible). Thus, a reversible process is required to deliver heat $đQ_R = đQ + đW^p$ to facilitate the substitution of (4.5) into the 1st law. Consider then the existence of a Carnot heat pump which over one cycle extracts $đQ$ from dV at state U (temp T) and delivers heat $đQ + đW^p$ to dV at state

$U + dU$ (temp $T + dT$). The work supplied to the heat pump over the cycle is $đW^p$ and evidently the net entropy of the system is unchanged by this operation and it is clearly reversible. Thus it is justifiable to substitute Equation (4.5) into the first law to give

$$TdS = đQ + đW - đW_R \tag{4.7}$$

or equivalently

$$dS = \frac{đQ}{T} + \frac{đW}{T} - \frac{đW_R}{T} \tag{4.8}$$

but note the inclusion of T (being intensive) necessities the elemental approach adopted above.

For an elemental volume dV, Equation (4.8) is equivalent to

$$dS = \left(\frac{\mathrm{div}\left(-\underline{q}\right)}{T} + \frac{\rho Q}{T} \right) dtdV + \frac{\underline{\underline{\sigma}} : \dot{\underline{\underline{\varepsilon}}}^p}{T} dtdV$$

$$= \left(\mathrm{div}\left(-\frac{\underline{q}}{T} \right) + \frac{\rho Q}{T} \right) dtdV + \underline{q} \cdot \nabla \left(\frac{1}{T} \right) dtdV + \frac{\underline{\underline{\sigma}} : \dot{\underline{\underline{\varepsilon}}}^p}{T} dtdV \tag{4.9}$$

and the transport equation immediately follows, i.e.

$$\frac{D^*}{D^* t} \int_\Omega \rho s dV + \int_\Gamma \rho s \left(\underline{v} - \underline{v}^* \right) \cdot \underline{n} d\Gamma = -\int_\Gamma \frac{\underline{q} \cdot \underline{n}}{T} d\Gamma + \int_\Omega \frac{\rho Q}{T} dV + \int_\Omega \frac{\underline{\underline{\sigma}} : \dot{\underline{\underline{\varepsilon}}}_p}{T} dV + \int_\Omega \underline{q} \cdot \nabla \left(\frac{1}{T} \right) dV \tag{4.10}$$

The two integral terms at the end right of Equation (4.10)

$$\int_\Omega \underline{\underline{\sigma}} : \dot{\underline{\underline{\varepsilon}}}_p dV + \int_\Omega \underline{q} \cdot \nabla \left(\frac{1}{T} \right) dV = \int_\Omega \frac{\underline{\underline{\sigma}} : \dot{\underline{\underline{\varepsilon}}}_p}{T} dV - \int_\Omega \frac{\underline{q} \cdot \nabla (T)}{T^2} dV \geq 0 \tag{4.11}$$

have the effect of producing entropy and affirms the non-conservative nature of entropy, i.e. entropy production is a part of the entropy transport equation.

4.4. Entropy Transport Equation for Plastic Deformation: Irreversible Approach

An alternative but equivalent approach, that avoids the need to consider reversibility, to arrive at Equation (4.10), is to consider dS to be formed in two parts, i.e. $dS = d_eS + d_iS$ (following the notation of Prigogine), where d_eS is the entropy due to exchange of energy (and matter) and d_iS is entropy produced by irreversible processes. It follows on consideration of an elemental volume dV that

$$d_eS = \left(\mathrm{div}\left(-\frac{\underline{\underline{q}}}{T} \right) + \frac{\rho Q}{T} \right) dV dt \tag{4.12}$$

and

$$d_iS = \left(\underline{q} \cdot \nabla\left(\frac{1}{T} \right) + \frac{\underline{\underline{\sigma}} : \underline{\underline{\dot{\varepsilon}}}_p}{T} \right) dV dt \tag{4.13}$$

but note that the exchange entropy (on comparison with Equation (4.8)) is of the form $d_eS = -đQ/T - d_i^QS$, where d_i^QS is the irreversible entropy production arising from temperature gradient. This infers that $-đQ = Td_eS + Td_i^QS$ (although according to Prigogine $Td_eS = -đQ$).

Summation (integration) of the elemental volumes leads to $\dot{S} = \dot{S}_e + \dot{S}_i$, where

$$\dot{S} = \frac{dS}{dt} = \frac{D^*}{D^*t}\int_\Omega \rho s dV + \int_\Gamma \rho s\left(\underline{v} - \underline{v}^* \right) \cdot \underline{n} d\Gamma \tag{4.14}$$

$$\dot{S}_e = -\int_\Gamma \frac{\underline{\underline{q}} \cdot \underline{n}}{T} d\Gamma + \int_\Omega \frac{\rho Q}{T} dV \tag{4.15}$$

$$\dot{S}_i = \int_\Omega \frac{\underline{\underline{\sigma}} : \underline{\underline{\dot{\varepsilon}}}_p}{T} dV + \int_\Omega \underline{q} \cdot \nabla\left(\frac{1}{T} \right) dV \geq 0 \tag{4.16}$$

where integration of (4.14) with respect to time produces S.

It is evident on comparison of (4.9) and (4.10) with (4.12) to (4.16), that both approaches provide the same outcomes.

4.5. Transport Equations for Fracture

It is of interest to consider an elemental volume where a crack is assumed to be present in the volume. For an elemental volume dV containing a surface dA_c identified with a crack path (ligament plus crack),

$$\begin{aligned} dU &= đQ_\Omega + đQ_{\Gamma_c} + đW_\Omega + đW_{\Gamma_c} = \\ &= \left(\mathrm{div}\left(-\underline{q}\right) + \rho Q\right) dt dV - \left[\left[\underline{q}_c \cdot \underline{n}_c\right]\right] dt dA_c + \underline{\underline{\sigma}} : \dot{\underline{\underline{\varepsilon}}} dt dV + \left[\left[\underline{\tau}_c \cdot \underline{v}_c\right]\right] dt dA_c \end{aligned} \tag{4.17}$$

where $đW_{\Gamma_c} = \left[\left[\underline{\tau}_c \cdot \underline{v}\right]\right] dt dA_c$ is positive and represents the work required to form new crack surface, and where $\underline{\tau}_c = -\underline{\tau}$, $\underline{n}_c = -\underline{n}$, $\underline{q}_c = -\underline{q}$, $\underline{v}_c = \underline{v}$, $\left[\left[\underline{\tau} \cdot \underline{v}\right]\right] = \underline{\tau}_2 \cdot \underline{v}_2 + \underline{\tau}_1 \cdot \underline{v}_1 = \underline{\tau}_2 \cdot \left(\underline{v}_2 - \underline{v}_1\right)$ and $\left[\left[\underline{q} \cdot \underline{n}\right]\right] = \underline{q}_2 \cdot \underline{n}_2 + \underline{q}_1 \cdot \underline{n}_1 = \underline{n}_2 \cdot \left(\underline{q}_2 - \underline{q}_1\right)$; note that Γ_c is considered contained in a domain of infinitesimal thickness, so $\underline{n}_c$ on Γ_c is outward pointing with regard to this domain.

This formulation is typical of a cohesive zone approach and a common approximation is $đW_{\Gamma_c} \approx \tau_n d\delta_n dA_c$, associated with mode I fracture, where τ_n is a

function of δ_n, and where δ_n represents normal separation. The corresponding transport equation is

$$\frac{D^+}{D^+t}\int_\Omega \rho u dV + \int_\Gamma \rho u\left(\underline{v}-\underline{v}^+\right)\cdot\underline{n}d\Gamma - \int_{\Gamma_c}\left[\left[\rho u\left(\underline{v}-\underline{v}^+\right)\cdot\underline{n}_c\right]\right]d\Gamma =$$

$$= \int_\Gamma \underline{v}\cdot\underline{\underline{\sigma}}\cdot\underline{n}d\Gamma - \int_{\Gamma_c}\left[\left[\underline{v}\cdot\underline{\tau}_c\right]\right]d\Gamma - \int_\Gamma \underline{q}\cdot\underline{n}d\Gamma + \int_{\Gamma_c}\left[\left[\underline{q}\cdot\underline{n}_c\right]\right]d\Gamma + \int_\Omega \rho Q dV + \int_\Omega \rho\underline{v}\cdot\underline{b}dV \tag{4.18}$$

where $\underline{v}^+$ matches the velocity of Γ_c and also $\underline{v}^+\cdot\underline{n} = \underline{v}^*\cdot\underline{n}$ on Γ, which is the boundary excluding Γ_c.

Equation (4.18) simplifies to

$$\frac{D^*}{D^*t}\int_\Omega \rho u dV + \int_\Gamma \rho u\left(\underline{v}-\underline{v}^*\right)\cdot\underline{n}d\Gamma =$$

$$= \int_\Gamma \underline{v}\cdot\underline{\underline{\sigma}}\cdot\underline{n}d\Gamma - \int_{\Gamma_c}\left[\left[\underline{v}\cdot\underline{\tau}_c\right]\right]d\Gamma - \int_\Gamma \underline{q}\cdot\underline{n}d\Gamma + \int_{\Gamma_c}\left[\left[\underline{q}\cdot\underline{n}_c\right]\right]d\Gamma + \int_\Omega \rho Q dV + \int_\Omega \rho\underline{v}\cdot\underline{b}dV \tag{4.19}$$

The transport equation for entropy follows on identification of irreversible terms, i.e.

$$d_iS = \left(\underline{q}\cdot\nabla\left(\frac{1}{T}\right) + \frac{\underline{\underline{\sigma}}:\dot{\underline{\underline{\varepsilon}}}_p}{T}\right)dVdt + \frac{\left[\left[\underline{\tau}_c\cdot\underline{v}\right]\right]}{T}dtdA_c \tag{4.20}$$

whilst exchange entropy is

$$d_eS = \left(\mathrm{div}\left(-\frac{\underline{q}}{T}\right) + \frac{\rho Q}{T}\right)dVdt + \frac{\left[\left[\underline{q}\cdot\underline{n}_c\right]\right]}{T}dA_cdt \tag{4.21}$$

The corresponding transport equation is

$$\frac{D^*}{D^*t}\int_\Omega \rho s dV + \int_\Gamma \rho s\left(\underline{v}-\underline{v}^*\right)\cdot\underline{n}d\Gamma = -\int_\Gamma \frac{\underline{q}\cdot\underline{n}}{T}d\Gamma + \int_{\Gamma_c}\frac{\left[\left[\underline{q}\cdot\underline{n}_c\right]\right]}{T}d\Gamma + \int_\Omega \frac{\rho Q}{T}dV$$

$$+\int_{\Omega}\frac{\underline{\underline{\sigma}}:\dot{\underline{\underline{\varepsilon}}}_{p}}{T}dV+\int_{\Gamma_c}\frac{\left[\left[\underline{v}\cdot\underline{\tau}_c\right]\right]}{T}d\Gamma+\int_{\Omega}\underline{q}\cdot\nabla\left(\frac{1}{T}\right)dV \qquad (4.22)$$

4.6. Cohesive Approach

It is evident that bulk properties predominately dictate the behaviour of the surface with the exception of a forming surface. It is reasonable to assume therefore that $dU = dU_{\Omega} + dU_{\Gamma_c}$, $dS = dS_{\Omega} + dS_{\Gamma_c}$, and it is convenient to assume further that S_{Ω} is a function of T only. This immediately infers that $dU_{\Omega} = dU_{\Omega}^{T} + dU_{\Omega}^{mech}$ and it follows from equation (4.17) that

$$dU_{\Omega}^{T} + dU_{\Omega}^{mech} + dU_{\Gamma_c} = \text{đ}Q + \text{đ}W_{\Omega} + \text{đ}W_{\Gamma_c} = \text{đ}Q + \text{đ}W_{\Omega}^{p} + \text{đ}W_{\Omega}^{e} + \text{đ}W_{\Gamma_c} \qquad (4.23)$$

and it follows following the discussion above that $dU_{\Omega}^{T} = \text{đ}Q + \text{đ}W_{\Omega}^{p}$, $dU_{\Omega}^{mech} = \text{đ}W_{\Omega}^{e}$ and $dU_{\Gamma_c} = \text{đ}W_{\Gamma_c}$.

In terms of an elemental volume

$$dU_{\Omega}^{T} = d\left(\rho cTdV\right) = \text{đ}Q + \text{đ}W_{\Omega}^{p} = \left(\text{div}\left(-\underline{q}\right) + \rho Q\right)dtdV + \left[\left[\underline{q}\cdot\underline{n}_c\right]\right]dtdA_c + \underline{\underline{\sigma}}:\dot{\underline{\underline{\varepsilon}}}^{p}dtdV \qquad (4.24)$$

$$dU_{\Omega}^{mech} = d\left(\omega dV\right) = \text{đ}W_{\Omega}^{e} = \underline{\underline{\sigma}}:\dot{\underline{\underline{\varepsilon}}}^{e}dtdV \qquad (4.25)$$

$$dU_{\Gamma_c} = d\left(udA_c\right) = \text{đ}W_{\Gamma_c} = \left[\left[\underline{\tau}_c\cdot\underline{v}\right]\right]dtdA_c \qquad (4.26)$$

where c is specific thermal heat capacitance, ω is strain energy, which is usually defined indirectly to a reference strain energy using $\omega dV = \omega_0 dV_0$, and u is the surface energy of formation.

In transport form these equations are:

$$\frac{D^*}{D^*t}\int_\Omega \rho cT dV + \int_\Gamma \rho cT\left(\underline{v}-\underline{v}^*\right)\cdot\underline{n}d\Gamma = -\int_\Gamma \underline{q}\cdot\underline{n}d\Gamma + \int_{\Gamma_c}\left[\left[\underline{q}\cdot\underline{n}_c\right]\right]d\Gamma + \int_\Omega \rho Q dV + \int_\Omega \underline{\underline{\sigma}}:\dot{\underline{\underline{\varepsilon}}}^p dV \tag{4.27}$$

$$\frac{D^+}{D^+t}\int_\Omega \omega dV + \int_\Gamma \omega\left(\underline{v}-\underline{v}^+\right)\cdot\underline{n}d\Gamma - \int_{\Gamma_c}\left[\left[\omega\left(\underline{v}-\underline{v}^+\right)\cdot\underline{n}_c\right]\right]d\Gamma = \int_\Omega \underline{\underline{\sigma}}:\dot{\underline{\underline{\varepsilon}}}^e dV \tag{4.28}$$

$$\frac{D^+}{D^+t}\int_{\Gamma_c} u d\Gamma + \int_{\Sigma_c} u\left(\underline{v}-\underline{v}^+\right)\cdot\underline{t}\underline{n}d\Sigma = \int_{\Gamma_c}\left[\left[\underline{v}\cdot\underline{\tau}_c\right]\right]d\Gamma \tag{4.29}$$

where Σ_c represents a contour boundary for the surface Γ_c and $\underline{t}\underline{n}$ represents unit normal on Σ_c lying in the tangent plane of Γ_c.

The transport equation for entropy follows in a similar fashion with most direct route by means of identifying irreversible processes, i.e. $dS = d_eS_\Omega + d_iS_\Omega + dS_{\Gamma_c}$, where

$$d_eS_\Omega = \left(\mathrm{div}\left(-\frac{\underline{q}}{T}\right)+\frac{\rho Q}{T}\right)dVdt + \frac{\left[\left[\underline{q}\cdot\underline{n}_c\right]\right]}{T}dA_c dt \tag{4.30}$$

$$d_iS_\Omega = \left(\underline{q}\cdot\nabla\left(\frac{1}{T}\right)+\frac{\underline{\underline{\sigma}}:\dot{\underline{\underline{\varepsilon}}}^p}{T}\right)dVdt \tag{4.31}$$

$$dS_{\Gamma_c} = d\left(sdA_c\right) = \frac{\left[\left[\underline{\tau}_c\cdot\underline{v}\right]\right]}{T}dtdA_c \tag{4.32}$$

where s is the surface entropy density of formation, and where Equation (4.32) in transport form is

$$\frac{D^+}{D^+t}\int_{\Gamma_c} s d\Gamma + \int_{\Sigma_c} s\left(\underline{v}-\underline{v}^+\right)\cdot\underline{t}\underline{n}d\Sigma = \int_{\Gamma_c}\frac{\left[\left[\underline{v}\cdot\underline{\tau}_c\right]\right]}{T}d\Gamma \tag{4.33}$$

4.7. Practical Demonstrations

It is of interest to explore some simple 1-D material models to better understand the theory under consideration. Material models can be constructed from springs, sliding friction and cohesive elements. The constitutive relationships selected for these elements are respectively: $\varepsilon = E^{-1}\sigma$; $\dot{\varepsilon} = \eta^{-1}\sigma'$; $\dot{\varepsilon} = 0$ if $\sigma < \sigma_Y$ and $\dot{\varepsilon} = \dot{\lambda}\sigma'$ otherwise; and $\delta = \delta_c\left(1 - \sigma_c^{-1}\sigma\right)$ for $0 < \sigma < \sigma_c$ when degradation has begun. Here E, η, δ_c and σ_c are material parameters, and σ' denotes deviatoric stress and δ is separation. Of principal interest here is the serial combination of these elements where it is assumed that strain rate components are simply additive. The classical Maxwell model for example is obtained on combining a spring and a dashpot to give $\dot{\varepsilon} = \dot{\varepsilon}^e + \dot{\varepsilon}^D = E^{-1}\dot{\sigma} + \eta^{-1}\sigma'$, where $\dot{\varepsilon} = \partial v/\partial x$ and v is material velocity. It is convenient also to decompose v into additive components and in the case of Maxwell $v = v^e + v^D$, where $\dot{\varepsilon}_e = \partial v^e/\partial x = E^{-1}\dot{\sigma}$, $\dot{\varepsilon}_D = \partial v^D/\partial x = \eta^{-1}\sigma'$, and where also $\varepsilon^e = \partial u^e/\partial x$. This later definition assumes small deflection theory is invoked (since require $D/Dt \approx \partial/\partial t$). It is instructive to consider the effect of including cohesive elements in various serial combinations when subjected to an initial strain/extension.

4.7.1 Spring and Cohesive Element Combination

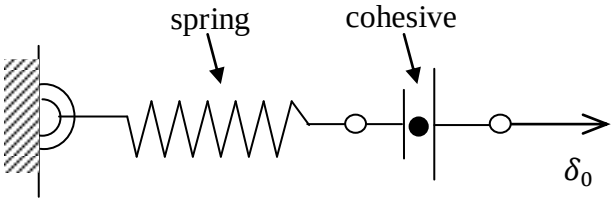

Figure 4.1 The elastic materials modelling

Consider the element subject to an initial extension δ_0, and let $\varepsilon_0 = \delta_0/\ell_0$ and $\sigma_0 = E\varepsilon_0$. If $\sigma_0 \le \sigma_c$, then $\sigma = E\varepsilon_0$, $\varepsilon = \varepsilon_0$ and $\delta_{tot} = \varepsilon_0\ell_0 = \delta_0$. If however $\sigma_0 > \sigma_c$, then require $\delta_0 = \delta^e + \delta$ and $\sigma_c\left(1-\delta/\delta_c\right) = \sigma^e = E\varepsilon^e = E\,\delta^e/\ell_0$, which solves to give

$$\frac{\delta^e}{\delta_c} = \frac{1-\dfrac{\delta_0}{\delta_c}}{1+\dfrac{E\delta_c}{\sigma_c\ell_0}} \tag{4.34}$$

which is valid for $\delta_0 \le \delta_c$ and should this equality be violated, then the material ceases to be load bearing.

The thermodynamics of this case is relatively straightforward since strain energy is $U_\Omega^{mech} = \tfrac{1}{2}k\delta^{e2} = \tfrac{1}{2}k\left(\delta_0-\delta\right)^2$, where $k = EA/\ell_0$ and surface formation energy is $U_{\Gamma_c} = \sigma_c\delta\left(1-\tfrac{1}{2}\tfrac{\delta}{\delta_c}\right)A$, whilst the only entropy change arises from the formation of new surface equal to $S_{\Gamma_c} = \sigma_c\delta\left(1-\tfrac{1}{2}\tfrac{\delta}{\delta_c}\right)AT^{-1}$, where A is cross sectional area and $\tfrac{1}{2}U_{\Gamma_c}$ and $\tfrac{1}{2}S_{\Gamma_c}$ can be attributed to each individual surface. Note that

$dU_{\Omega}^{mech} = k\delta^{e}d\delta^{e} = -dW_{\Omega}^{e}$ and $dU_{\Gamma_c} = \sigma_c\left(1-\frac{\delta}{\delta_c}\right)Ad\delta = -dW_{\Gamma_c} = -\sigma^{e}Ad\delta^{e} = -k\delta^{e}d\delta^{e}$

and it follows that $dU_{\Omega}^{mech} = -dU_{\Gamma_c}$, confirming that any loss in elastic energy gives rise to a gain in surface formation energy. In this case external boundaries are fixed, so $dU_{\Omega}^{mech} + dU_{\Gamma_c} = 0$.

4.7.1.1 The Calculation of Energy for Elastic Materials

The understanding of energy required to create a crack is highlighted by the stress-displacement response of spring-cohesive combination as shown in Figure 4.2. The strain or elastic energy for spring is identified as $U_{\Omega}^{mech} = \frac{1}{2}k\delta^{e2}$ where $k = EA/\ell_o$. Thus strain or elastic energy can be expressed as $U_{\Omega}^{mech} = \frac{1}{2}(EA/\ell_o)\delta^{e2}$. If $\varepsilon = \delta^{e}/\ell_o$ and $\sigma = E\varepsilon$. The strain energy can be shown in form of $U_{\Omega}^{mech} = \frac{1}{2}\sigma A\delta^{e}$. The calculation of elastic energy per unit area, $W_e = U_{\Omega}^{mech}/A = \frac{1}{2}\sigma\delta^{e}$, can be explained using Figure 4.2.

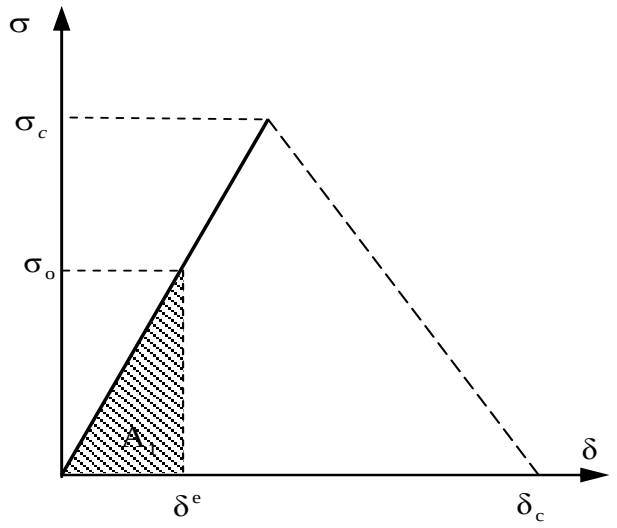

Figure 4.2 Stress-displacement response of spring-cohesive combination

For $\sigma_0 \le \sigma_c$ the elastic energy per unit area W_e is defined as area A_1 i.e.

$$W_e = A_1 = \frac{1}{2}\sigma_o \delta^e \tag{4.35}$$

which is equal to work done per unit area W_d .

For $\sigma_0 > \sigma_c$ Figure 4.3(a) it is apparent on elimination of that the stored elastic energy per unit area is defined as area A_1 is

$$W_e = A_1 = \frac{1}{2}\sigma^e \delta^e \tag{4.36}$$

In addition, the shaded area A_2 is equal to

$$\begin{aligned} A_2 &= \frac{1}{2}\left(\sigma_c + \sigma^e\right)\left(\delta^a - \delta^e\right) + \frac{1}{2}\left(\sigma_c + \sigma^e\right)\left(\delta_o - \delta^a\right) \\ A_2 &= \frac{1}{2}\left[\sigma_c\delta^a - \sigma_c\delta^e + \sigma^e\delta^a + \sigma^e\delta^e + \sigma_c\delta_o - \sigma_c\delta^a + \sigma^e\delta_o - \sigma^e\delta^a\right] \\ A_2 &= \frac{1}{2}\left[\left(\sigma_c + \sigma^e\right)\delta_o - \left(\sigma_c + \sigma^e\right)\delta^e\right] \end{aligned} \tag{4.37}$$

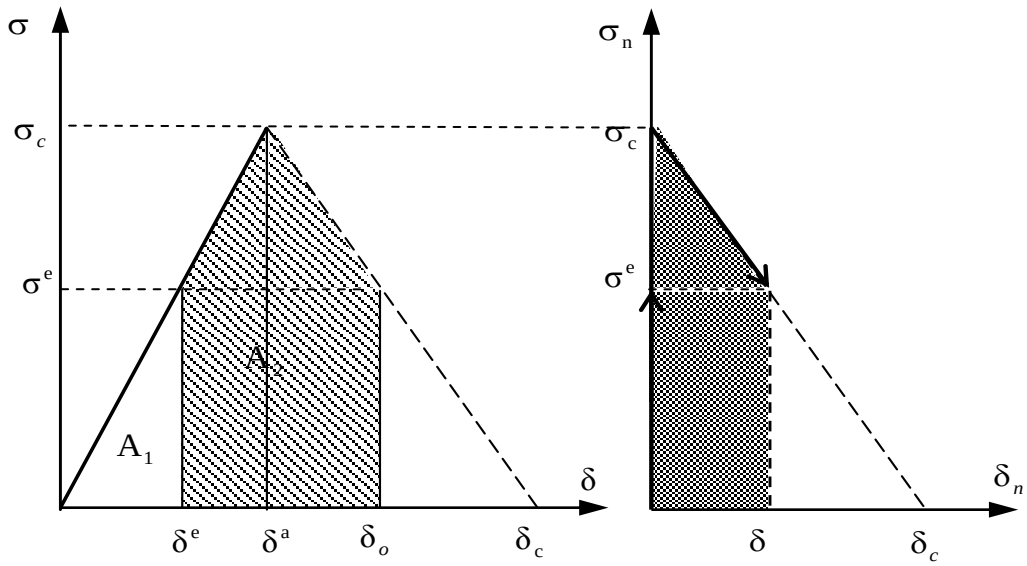

(a) elastic material (b) cohesive element

Figure 4.3 The stress-displacement response beyond critical traction

Figure 4.3(b) reveals that the dissipated separation energy per unit area is equal to.

$$W_s = \frac{1}{2}\left(\sigma_c + \sigma^e\right)\delta \tag{4.38}$$

where $\delta = \delta_o - \delta^e$. Equation (4.38) can be reduce to

$$W_s = \frac{1}{2}\left(\sigma_c + \sigma^e\right)\left(\delta_o - \delta^e\right) = \frac{1}{2}\left[\left(\sigma_c + \sigma^e\right)\delta_o - \left(\sigma_c + \sigma^e\right)\delta^e\right] \tag{4.39}$$

It reveals that the shade area A_2 from Figure 4.3(a) is equal to the separation energy per unit area W_s.

The work done per unit area for the system can be calculated by the summation of A_1 and A_2 i.e.

$$W_d = \frac{1}{2}\left[\sigma^e\delta^e + \left(\sigma_c + \sigma^e\right)\delta_o - \left(\sigma_c + \sigma^e\right)\delta^e\right] = \frac{1}{2}\left[\left(\sigma_c + \sigma^e\right)\delta_o - \sigma_c\delta^e\right] \tag{4.40}$$

4.7.1.2 Model Description

The elements shown in Figure 4.1 are attributed with materials properties: the spring has Young's modulus E of 7200 MPa, initial length L_o of 10 mm and cross section area A of 1 mm^2, respectively. The cohesive element has critical cohesive traction σ_c of 340 MPa and different value of toughness Gc of 30, 25 and 20 N/mm, respectively.

4.7.1.3 Results and Discussion

Figure 4.4 presents curves for different energy and displacements for different values of toughness. A single source of energy transfer is the work done by an applied load. This has the effect of solely energizing elastically until a critical traction is attained and the dissipative mechanism of separation begins. Beyond the critical traction, the elastic energy begins to decrease gradually alongside the appearance and increase of separation energy until it completely vanishes when the separation energy reaches its maximum value.

Figure 4.5 shows a graph of the various energies normalized with regard to the total energy versus the applied displacement. The elastic energy has the same value as the normalized total energy before the appearance of the normalized separation energy. The normalized elastic energy decreases gradually with the rise of normalized separation energy. It is clear from Figure 4.5 that the dissipative separation process is driven by the elastic energy.

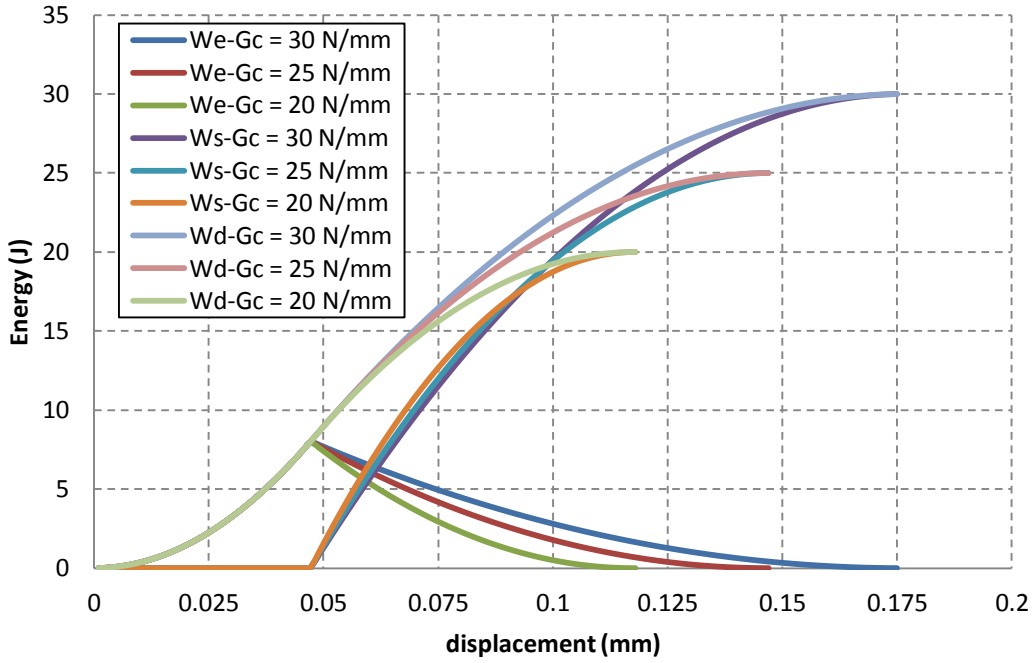

Figure 4.4 The energy comparison for elastic material

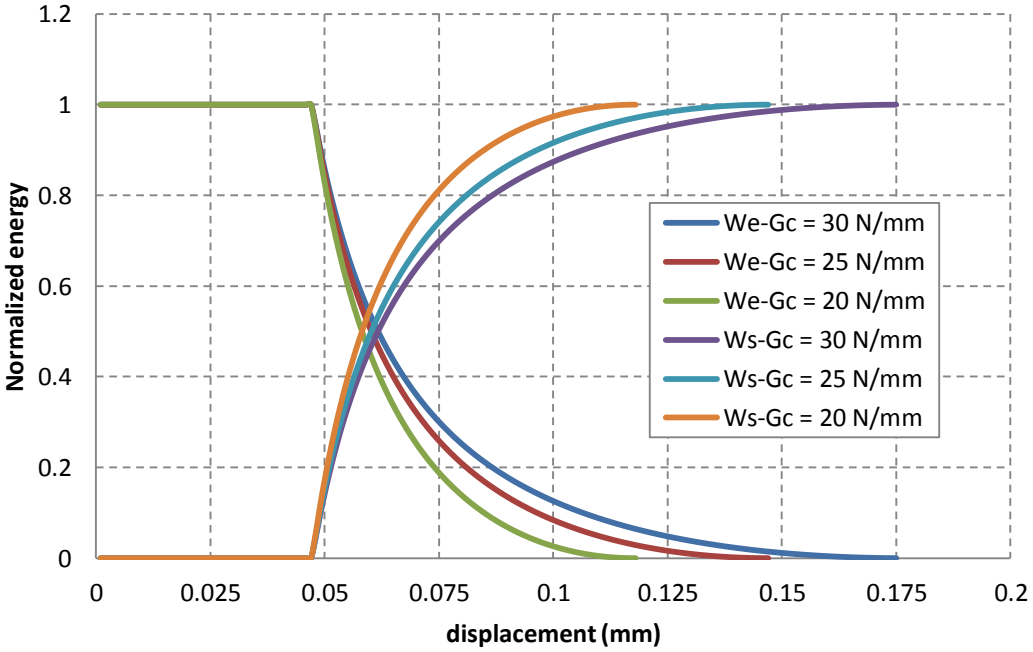

Figure 4.5 The normalized energy comparison for elastic material

4.7.2 Sliding-Friction, Spring and Cohesive Element Combination

The model under consideration is depicted in Figure 4.6 and involves a sliding element to capture on phenomenon of plasticity. In simple tension the behaviour of the element is initially elastic followed by plastic deformation or crack separation when the load is sufficient; the dominance of which depends on the relative magnitudes of σ_c and treat as yield stress σ_Y. If $\sigma_Y < \sigma_c$, then plastic deformation occurs prior to any possible crack formation but if $\sigma_c < \sigma_Y$, then crack separation occurs and plasticity is not realised. Attention is restricted to the former (i.e. $\sigma_Y < \sigma_c$) and where the plastic response is approximated by the linear expression $\bar{\sigma} = \sigma_Y + E^p \bar{\varepsilon}^p$, where for uniaxial tension $\bar{\sigma} = \sigma$ and $\bar{\varepsilon}^p = \varepsilon^p$. Thus for $\sigma \le \sigma_Y$ and $\varepsilon \le \sigma_Y / E$, then $\varepsilon = \varepsilon^e = \sigma / E$ and for $\sigma_Y < \sigma < \sigma_c$, and $\varepsilon^p < \varepsilon_c^p = \left(\sigma_c - \sigma_Y\right) / E^p$, then $\varepsilon = \left(\sigma - \sigma_Y\right) / E^p + \varepsilon^e$, where $\varepsilon^e = \sigma / E$. For the situation where $\varepsilon^p \ge \varepsilon_c^p$, then $\delta = \delta_c \left(1 - \sigma_c^{-1} \sigma\right)$ and again $\varepsilon^e = \sigma / E$. It is assumed here that when separation is initiated that unloading is elastic.

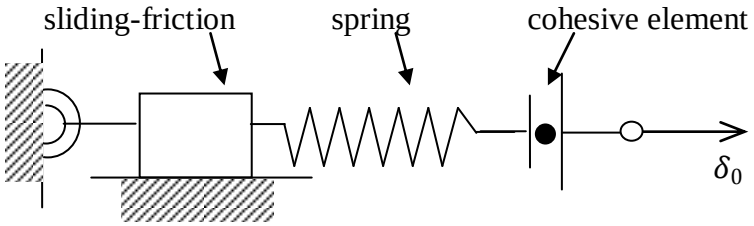

Figure 4.6 The elastic plastic materials modelling

4.7.2.1 The Calculation of Energy for Elastic Plastic Materials

Figure 4.7, 4.8 and 4.9 show the model of slider-spring-cohesive element in stress-displacement response for $\sigma \le \sigma_Y$, $\sigma_Y < \sigma < \sigma_c$ and $\sigma > \sigma_c$ condition, respectively. For $\sigma \le \sigma_Y$, the elastic energy per unit area is defined as area A_1 as show in Figure *4.7* i.e.

$$W_e = A_1 = \frac{1}{2}\sigma\delta^e \tag{4.41}$$

which is equal to work done per unit area for the system.

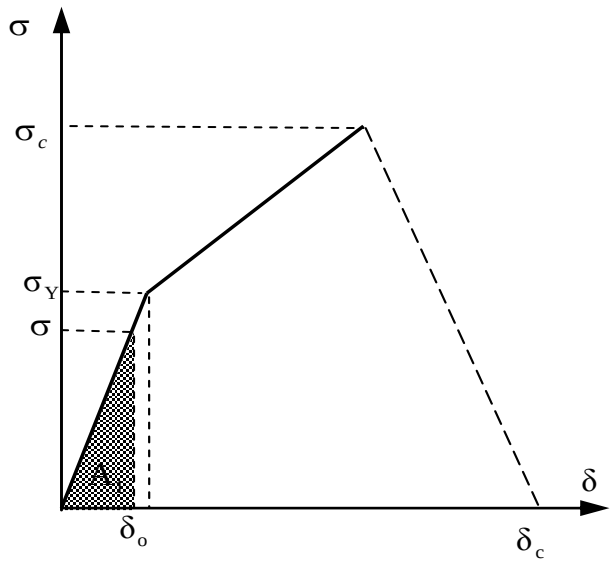

Figure 4.7 The stress-displacement response $(\sigma < \sigma_Y)$ for the slider-spring-cohesive element model

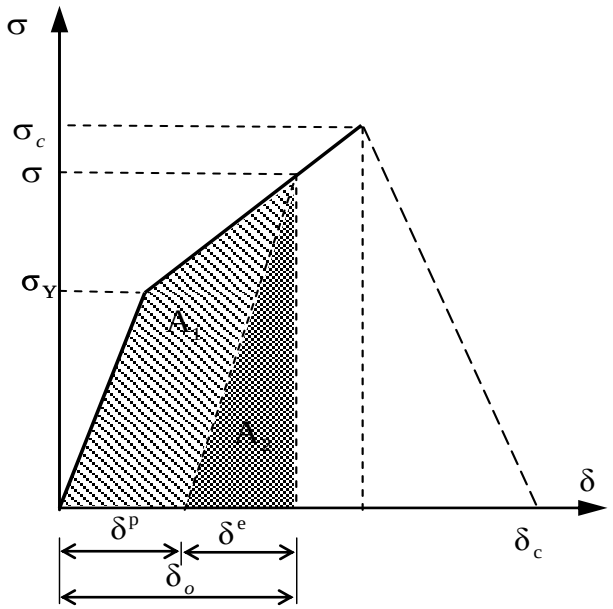

Figure 4.8 The stress-displacement response $(\sigma_Y < \sigma < \sigma_C)$ for the slider-spring-cohesive element model

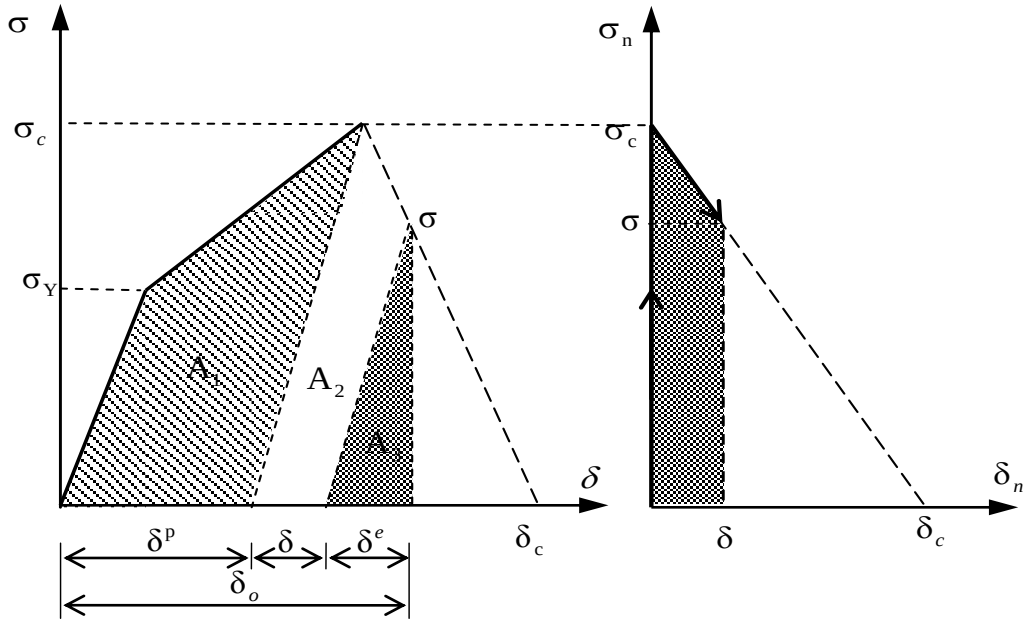

(a) elastic-plastic material (b) cohesive element

Figure 4.9 The stress-displacement response $(\sigma_C < \sigma)$ for the slider-spring-cohesive element model

For $\sigma_Y < \sigma < \sigma_c$, the schematic stress distribution is presented in Figure 4.8. The stored elastic energy per unit area is equal to the area A_3 depicted in the figure.

$$W_e = A_3 = \frac{1}{2}\sigma\left(\delta^e\right) \tag{4.42}$$

In addition, the shaded area A_1 is the plastic energy dissipated per unite area and given by

$$W_p = A_1 = \frac{1}{2}\left(\sigma_Y + \sigma\right)\delta^p \tag{4.43}$$

where σ_Y and δ^p are yield stress and plastic displacement when the bar is unloaded, respectively. The work per unit area done by the applied load is equal to

$$W_d = A_1 + A_2 = \frac{1}{2}\sigma\delta^e + \frac{1}{2}\left(\sigma_Y + \sigma\right)\delta^p = \frac{1}{2}\left[\left(\sigma_Y + \sigma\right)\delta^p + \sigma\delta^e\right] \tag{4.44}$$

Highlight in Figure 4.9(a) for $\sigma > \sigma_c$, is the stored elastic energy per unit area is defined as area A_3 i.e.

$$W_e = A_3 = \frac{1}{2}\sigma\delta^e \tag{4.45}$$

In addition, the shaded area A_1 is the plastic energy per unit area dissipates and is given by

$$W_p = A_1 = \sigma_Y\delta^p + \frac{1}{2}\left(\sigma_c - \sigma_Y\right)\delta^p = \sigma_Y\delta^p + \frac{1}{2}\sigma_c\delta^p - \frac{1}{2}\sigma_Y\delta^p = \frac{1}{2}\left(\sigma_c + \sigma_Y\right)\delta^p \tag{4.46}$$

Also shown in Figure 4.9(b) it is the separation energies per unit area as the area under curve i.e.

$$W_s = \frac{1}{2}\left(\sigma_c - \sigma\right)\delta + \sigma\delta = \frac{1}{2}\sigma_c\delta - \frac{1}{2}\sigma\delta + \sigma\delta = \frac{1}{2}\left(\sigma_c + \sigma\right)\delta \tag{4.47}$$

where $\delta = \delta_o - \left(\delta^e + \delta^p\right)$

It is clear that the shaded area A_2 is equal to the separation energy W_s.

The work done on the system can be calculated by the summation of A_1, A_2 and A_3 to give

$$W_d = \frac{1}{2}\left[\sigma\delta^e + \left(\sigma_c + \sigma_Y\right)\delta^p + \left(\sigma_c + \sigma\right)\delta\right] \quad (4.48)$$

4.7.2.2 Material Properties

The elements shown in Figure 4.6 are attributed with materials properties: the spring has Young's modulus E of 7200 MPa, and the plastic modulus (E_T) of 1.39 GPa is represented a linear isotropic hardening. The Initial length L_o is 10 mm and cross section area A of 1 mm^2, respectively. The cohesive element has critical traction (σ_c) of 340 MPa and the critical energy release rate (Gc) of 30, 25 and 20 N/mm, respectively.

4.7.2.3 Results and Discussion

Figure 4.10 shows curves for different energy and loading conditions for elastic-plastic behaviour. A single source of energy transfer is the work done by an applied load. It can be seen from the figure that only elastic energy appears initially prior to yielding. Beyond the yield load but prior to the critical of traction, the plastic energy appears and then increases with applied loading. However, beyond the critical cohesive traction condition, the plastic energy is completely dissipated but elastic

energy begins to decrease gradually with the appearance of the energy separation. The elastic energy completely vanishes when the separation reaches its maximum value.

Figure 4.11 shows a graph of the various energies normalized with regard to the total energy minus the plastic energy versus the applied displacement. It can be seen from the figure that the elastic energy has the same value as the normalized total energy before the appearance of the normalized separation energy. The normalized elastic energy decreases gradually with the rise of normalized separation energy. It is clear from the figure that the dissipative separation process is driven by the elastic energy. It can be concluded for this model that the separation energy required to create a crack is supplied by the elastic energy. Furthermore, varying the toughness values has limited effect on elastic energy making it essentially invariant which can be contrasted with the separation energy which decreases with toughness.

4.8. Summary

It can be concluded in the cohesive approach that the separation energy required to create a crack is supplied predominantly by the elastic energy for both elastic and elastic-plastic materials. Meanwhile, plastic energy has been assumed to completely dissipate into thermal energy as a consequence of assuming that the material entropy is a function of temperature only.

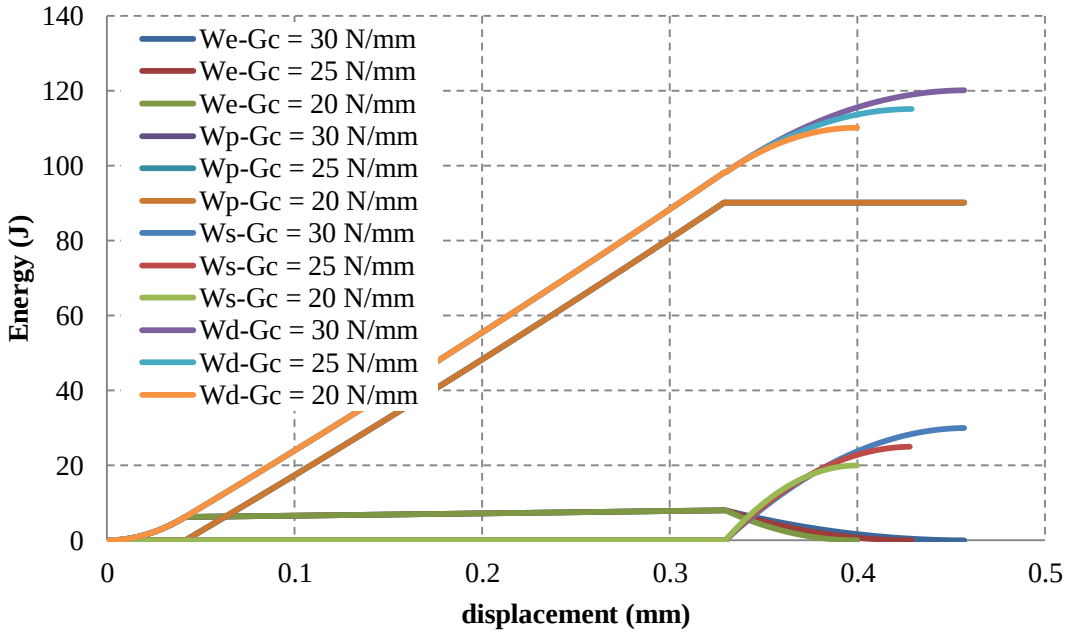

Figure 4.10 The energy comparison for elastic-plastic material

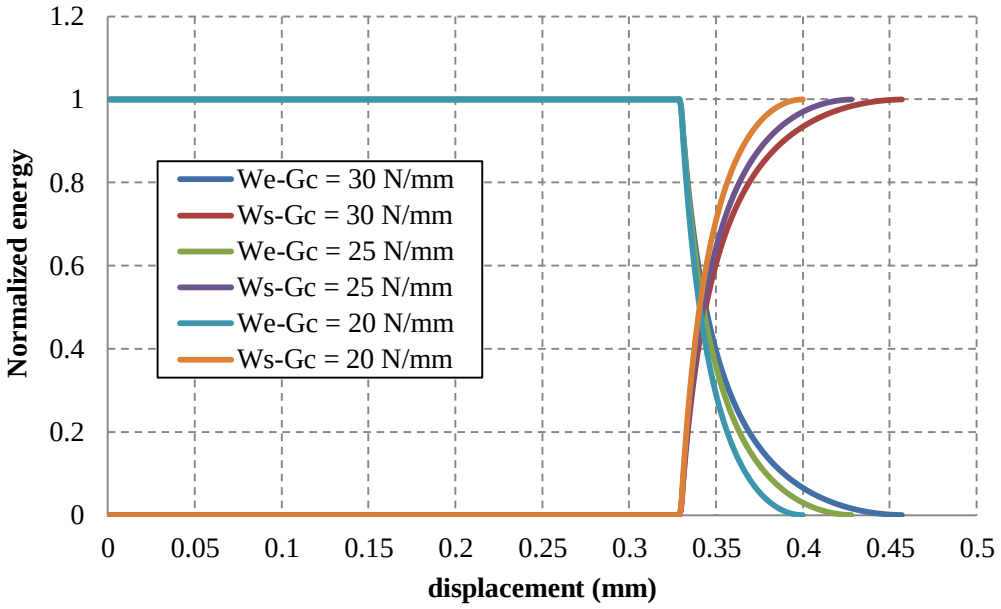

Figure 4.11 The normalized energy comparison for elastic-plastic material

Chapter 5

Cohesive Zone Model

5.1. Introduction

The cohesive zone model is delivered to provide a realistic representation fracture mechanism and also delivers simplicity in simulations of complex cracking processes. From the continuum mechanics point of view, crack extension improve complex failure processes at the microscopic levels such as void nucleation, growth and coalescence in ductile metals, microcrack in ceramics and crazing in certain polymers. If the failure process is limited to a narrow band, such as crazing in polymers and necking in ductile thin-sheet materials as shown in Figure 5.1, the cohesive zone may be utilized to perform the narrow deformation band. The cohesive zone may be regarded as an approximate representation of the crack tip failure process zone, such as microcrack in brittle materials and void growth and coalescence in ductile metals as shown in Figure 5.2.

In general, cohesive zone approach assumes that ahead of the physical crack tip exists a cohesive zone, which consists of upper and lower surfaces called cohesive surfaces held by the cohesive traction. The cohesive traction is related to the separation displacement between the cohesive surfaces by a cohesive law. The application of external loads to the cracked body may cause the two cohesive surfaces to separate gradually and lead to crack growth when the separation of both surfaces at the tail of the cohesive zone (physical crack tip) reaches a critical value. Figure 5.3 shows a cohesive zone ahead of a crack where σ is the cohesive traction and δ is the separation displacement of the cohesive surfaces.

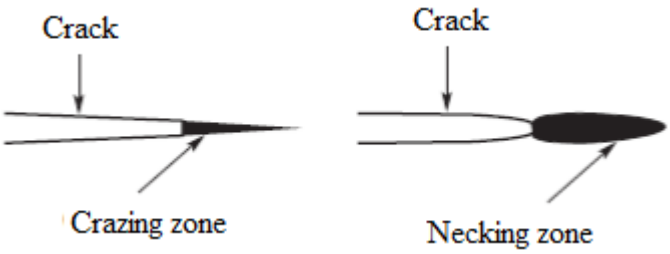

Figure 5.1 (a) Crazing zone ahead of a crack in a polymer, (b) necking zone in a ductile thin-sheet material [66]

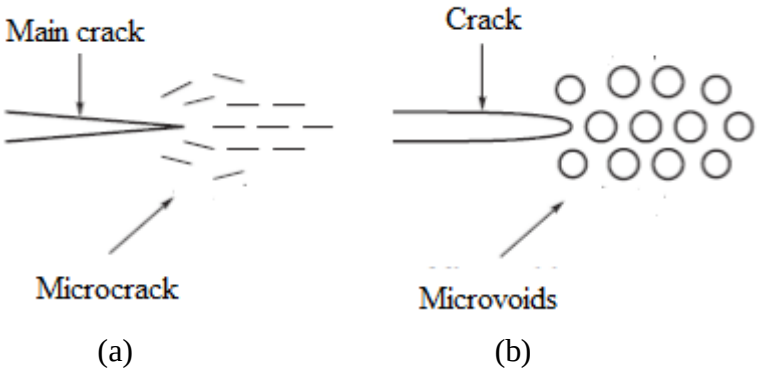

Figure 5.2 (a) Microcrack zone ahead of a crack in a brittle solid (b) voids in a ductile metal [66]

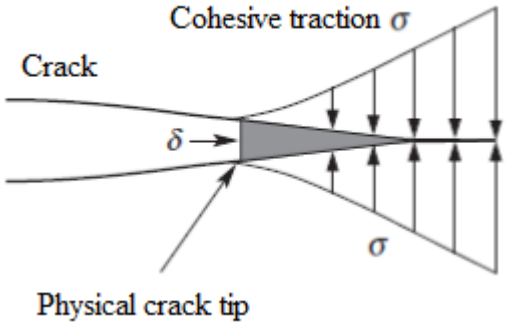

Figure 5.3 A cohesive zone ahead of a crack tip [66]

The basic concept of cohesive zone model was introduced by Dugdale [12] and Barenblatt [13]. In these models, the crack is divided into two parts, one part of the crack surface is stress free, and the other part is loaded by cohesive stresses as shown in Figure 5.4. Dugdale [12] introduced the finite stress to be the yield stress σ_Y applicable only for plane stress, but in practice the crack-opening stresses can be much higher than by yield stress. Barenblatt [13] investigated the fracture of brittle materials, he made several assumptions about the cohesive stresses, i.e. the extension of the cohesive zone is constant for a given material and small compared to other dimensions, the stress in the cohesive zone follow a prescribed distribution yield stress, $\sigma_Y(x)$, where x is ligament coordinate, which is specific for a given material but independent of the global loading conditions.

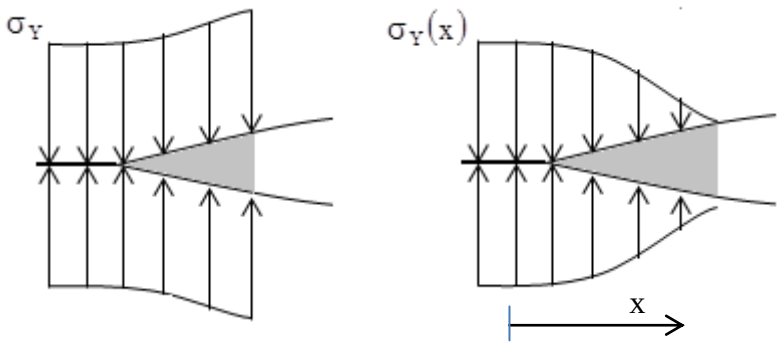

Figure 5.4. (a) Dugdale crack model and (b) Barenblatt crack model

The first application of the cohesive stress at the crack tip in the finite element method and developed crack tip model that involves crack growth was introduced by Hillerborg [14]. He proposed a model which in some respects is similar to the Barenblatt's model for brittle material. The crack is assumed to extend when the stress at the crack tip reaches the tensile strength. When the crack surface opens the stress is not assumed to fall down to zero suddenly, but it will decreases with increasing separation. The stress reaches zero when the crack tip surface reaches prescribed separation distance.

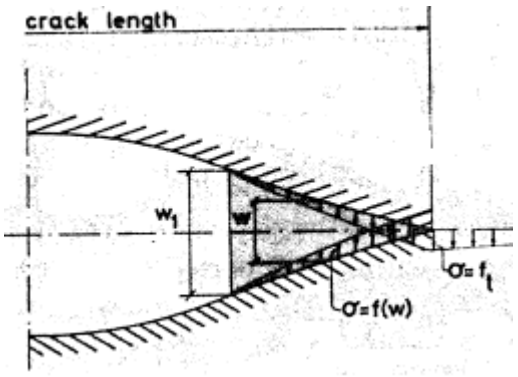

Figure 5.5 Hillerborg model [14]

In the current cohesive zone model, material separation and damage of the structure is classically described by interface elements. The interface elements open when damage occurs and completely lose their stiffness at failure so that continuum elements became disconnected. The crack is limited to propagate only along the element boundaries. The constitutive behaviour of a cohesive element is characterized by the relationship between a crack tip opening value or critical separation δ_c and the critical cohesive traction σ_c.

A large number of phenomenological traction-separation laws have been proposed and illustrated in Figure 5.6 such as bilinear [67-70], trapezoidal [71], polynomial and exponential [72-78]. The qualitative shape of these functions is similar. Starting at the traction free undeformed state, the value of cohesive traction increases with the separation of crack surfaces up to a maximum value σ_c and decreases to zero when complete separation occurs at specific critical separation value δ_c. However, the effect of the cohesive law shape on numerical results of fracture simulations has been investigated by [71, 73, 79, 80]. They revealed that the shape of traction-separation curve does not significantly affect the separation materials behaviour in numerical results.

For fatigue analysis, irreversible cohesive zone model involves a damage evolution mechanism representing gradual degradation of the cohesive traction under cyclic loading. De-Andres [81] considered to add unloading conditions to a traction–separation law used in monotonic loading in conjunction with a cycle dependent

damage variable to study fatigue crack growth under large scale yielding. Nguyen [82] developed a cohesive zone model using irreversible unload–load relations. The model was utilized to study fatigue crack growth in macroscopic aluminium specimens for constant amplitude loading and also to investigate the effects of overloads on fatigue crack growth. Roe and Siegmund [40] and Siegmund [51] proposed irreversible cohesive zone model involving a cyclic damage evolution rule for the cohesive strength to simulate fatigue crack growth.

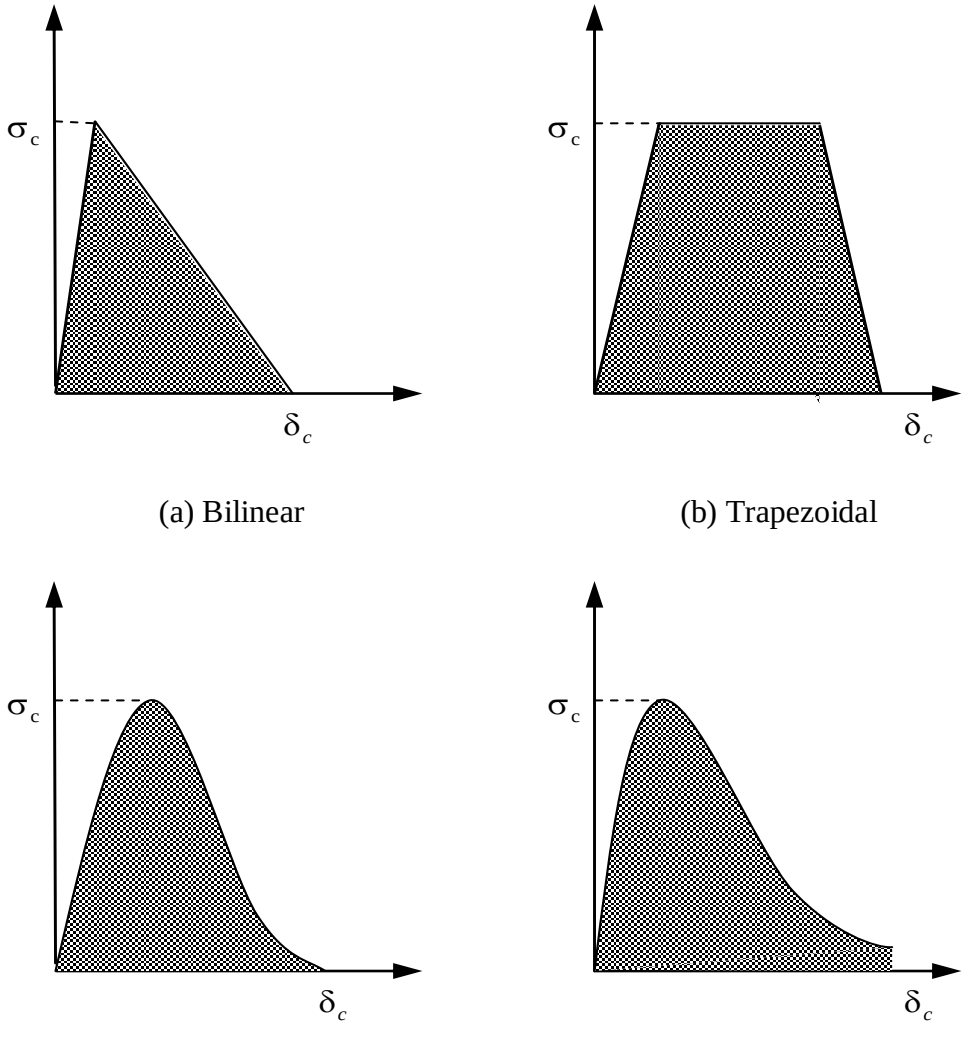

(a) Bilinear (b) Trapezoidal

(c) Polynomial (d) Exponential

Figure 5.6 The various shapes of traction-separation law

Most irreversible cohesive zone models considered the separation will back to zero along with unloading condition. However, in the present study, it is assumed that normal displacement jump or separation under unloading condition is constant. This is caused by the normal separation undergo the plastic deformation in that condition. The irreversible cohesive zone model is defined as the accumulation of the normal displacement jump or normal separation under cyclic loading. The normal separation also relate to the degrading of cohesive traction.

In this chapter, the cohesive zone model in Code_Aster is presented and its implementation for constant amplitude loading and single overloading is studied. The fatigue crack growth curve is provided with various boundary conditions. The effect of critical cohesive traction on the fatigue crack growth rate by using the cohesive zone model due to the single overloading is presented.

5.2. Cohesive Element Law

With the cohesive approach for brittle fracture, the problem of infinite stresses at the crack tip is not relevant anymore, so it is possible to impose a criterion on a cohesive force for crack initiation. Forces acting between particles on both side of the parting of a crack are shown in Figure 5.7.

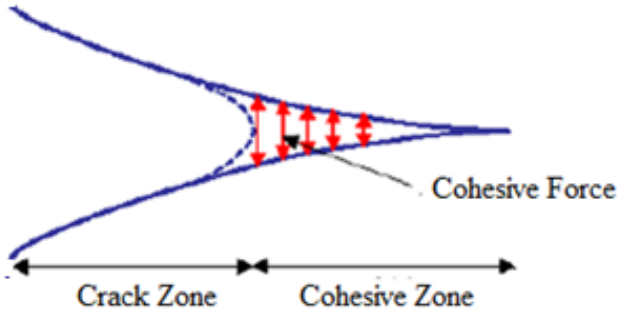

Figure 5.7 Schematic of a crack

It is considered reasonable to assume that the opening crack dissipates energy proportional to its length. The dissipated energy is called the surface energy and is denoted as Ψ. The surface energy defined at a discontinuity Γ representing a crack is considered dependent on the normal displacement jump δ_n of the crack surfaces and an internal variable κ which manages the crack irreversibility. The crack irreversibility is defined to be the accumulation of normal displacement jump during loading cycles as shown in Figure 5.8.

In incremental terms the crack irreversibility is expressed as

$$\kappa^i = \kappa^{i-1} + \left\langle \delta_n^i - \delta_n^{i-1} \right\rangle \tag{5.1}$$

Where $\langle \cdot \rangle$ is positive when its content are positive but zero otherwise. The surface energy is defined as follows

$$\Psi(\delta_n, \kappa) = \int_\Gamma \Pi(\delta_n, \kappa) d\Gamma \tag{5.2}$$

where the surface energy density Π is considered of the form

$$\Pi(\delta_n, \kappa) = \psi(\kappa) + I_{R^+}(\delta_n) \tag{5.3}$$

where ψ is a cohesive energy density and I_{R^+} is indicator function reflecting the impenetrability condition the crack surface. I_{R^+} is defined to be

$$\begin{aligned} I_{R^+}(\delta_n) &= +\infty \quad \text{for } \delta_n < 0 \\ &= 0 \quad \text{for } \delta_n > 0 \end{aligned} \tag{5.4}$$

where the subscript n denotes the normal component ($\delta_n = \underline{\delta} \cdot \underline{n}$ is the opening displacement or separation, $\underline{n}$ is an unit normal at Γ). The indicator function precludes inter penetration since negative displacement jumps would result in an infinite energy (hence not a minimum).

The cohesive energy density ψ can further be defined as

$$\begin{aligned} \psi(\kappa) &= \frac{-\sigma_c^2}{4G_c}\kappa^2 + \sigma_c \kappa \quad \text{for } \kappa \le \frac{2G_c}{\sigma_c} \\ &= G_c \quad \text{for } \kappa \ge \frac{2G_c}{\sigma_c} \end{aligned} \tag{5.5}$$

where σ_c is the maximum traction or critical cohesive traction and G_c is the critical strain energy release rate also known as toughness or cohesive energy. The relationship between the cohesive energy density and the irreversibility of cracking is shown in Figure 5.9.

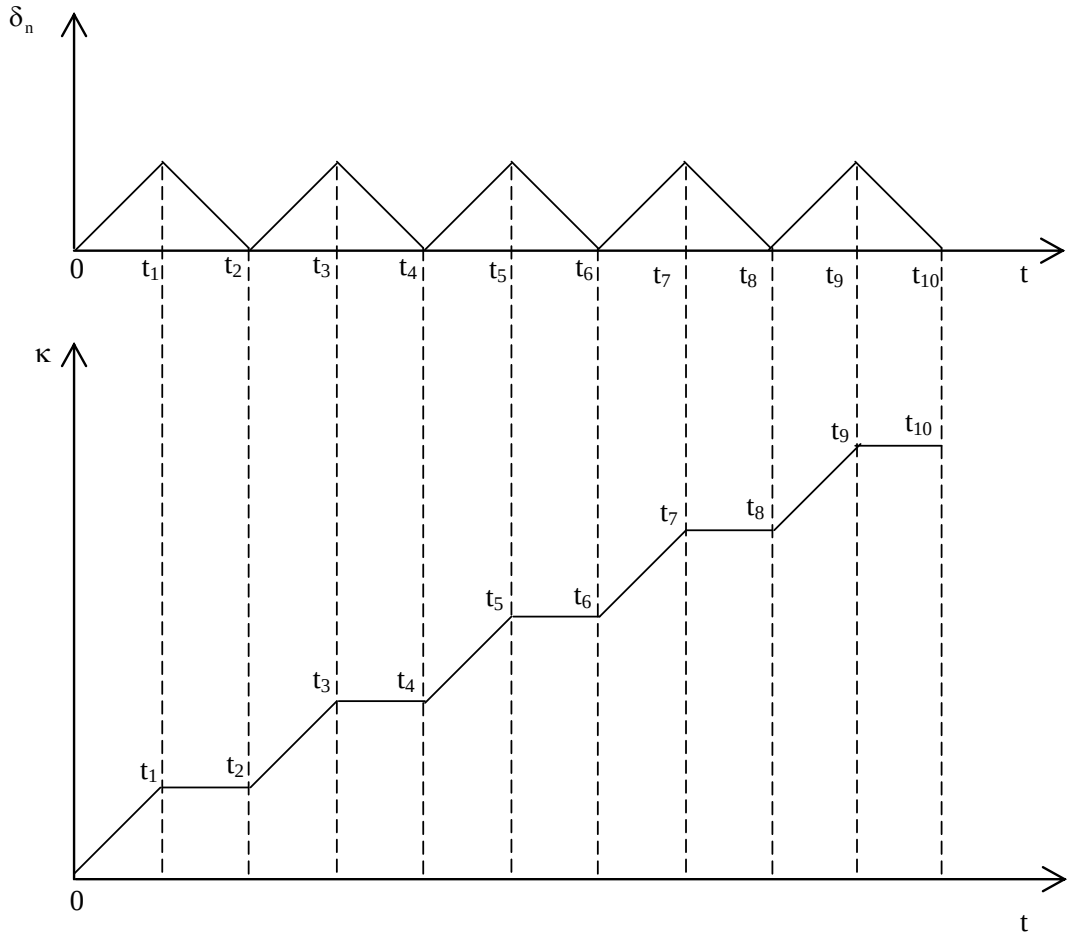

Figure 5.8 The accumulation of normal displacement jump during loading cycles

The stress vector noted traction $\underline{\tau}$ is defined as belonging to a differential of the surface energy density

$$\underline{\tau} = \partial \prod(\delta, \kappa) \tag{5.6}$$

It is possible to define the normal cohesive traction to

$$\sigma_n(\delta_n) = \frac{\partial \psi}{\partial \delta_n} = \frac{\partial \psi}{\partial \kappa} \frac{\partial \kappa}{\partial \delta_n} \tag{5.7}$$

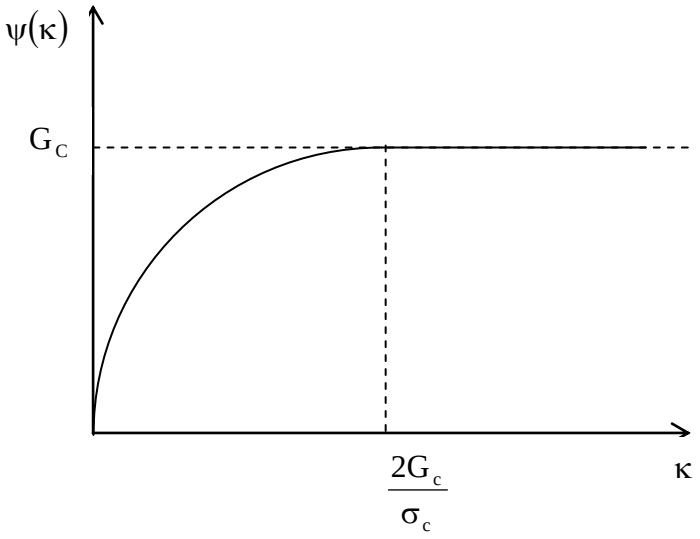

Figure 5.9 The correlation between the cohesive energy density and the irreversibility of cracking

Since differentiation of Equation (5.7) reveals

$$\frac{\partial \psi}{\partial \kappa} = \sigma_c \left(1 - \frac{\kappa}{\delta_c}\right) \quad \text{for } \kappa < \delta_c$$
$$= 0 \qquad \text{for } \kappa \geq \delta_c$$

$$\frac{\partial \kappa}{\partial \delta_n} = 1 \quad \text{for } \dot{\delta}_n > 0 \text{ and } \delta_c \neq 0$$
$$= 0 \quad \text{for } \dot{\delta}_n < 0 \text{ and } \delta_c \neq 0$$

where $\delta_c = 2G_c \cdot \sigma_c^{-1}$ is the critical separation that means beyond this value the rupture of materials occurred. $\dot{\delta}_n$ is the rate of normal separation. The cohesive law can be conveniently classified into three stages: initial stage, damage and post fracture as illustrated in Figure 5.10.

In initial stage, there is no cumulative irreversibility so $\kappa^{i-1}=0$, and consequently the normal cohesive traction is function of current normal separation which can be defined as follows

$$\begin{aligned}\sigma_n\left(\delta_n^i\right)&=\sigma_c\left(1-\frac{\delta_n^i}{\delta_c}\right) \quad \text{for } 0<\delta_n^i\le\delta_c\\ &=0 \qquad\qquad\quad \text{for } \delta_n^i\ge\delta_c\end{aligned} \tag{5.8}$$

and initiation period where $\sigma_n(0)\le\sigma_c$.

The damage stage involves irreversibility, so $0<\kappa^{i-1}<\delta_c$, and normal separation is defined as

$$\begin{aligned}\sigma_n\left(\delta_n^i\right)&=0 &&\text{for } 0<\delta_n^i\le\delta_n^{i-1}\\ &=\sigma_c\left(1-\frac{\kappa^{i-1}+\delta_n^i-\delta_n^{i-1}}{\delta_c}\right) &&\text{for } \delta_n^{i-1}<\delta_n^i<d_c\\ &=0 &&\text{for } \delta_n^i>d_c\end{aligned} \tag{5.9}$$

where $d_c=(\delta_c S_c)\cdot\sigma_c^{-1}$ and $S_c=\sigma_c\cdot\left\{1-\left(\left(\kappa^{i-1}-\delta_n^{i-1}\right)\cdot\delta_c^{-1}\right)\right\}$.

In the post fracture stage identified by $\kappa^{i-1}\ge\delta_c$, where the normal separation can be defined as

$$\sigma_n\left(\delta_n^i\right)=0 \qquad \text{for } 0<\delta_n^i \tag{5.10}$$

Cycle is presented in Figure 5.8 where the $0\le\sigma_n\left(\delta_n^i\right)<\sigma_c\left(1-\left(\kappa^{i-1}\right)\cdot\delta_c^{-1}\right)$ applied. Figure 5.11 presents cyclic condition in the traction-separation curve. One first cycle is identified via path 0-1-2-3-0 then second cycle followed by 0-3-2-4-3 and so on. Since the area under one looping is defined as energy dissipated or separation energy, a crack begins propagation when the accumulation of separation energy

every cycle reaches the cohesive energy G_c .The separation energy dissipated for the one cycle loading as shown in Figure 5.12 can be calculated by

$$\Delta G = \kappa\sigma_c\left(1-\frac{\kappa\sigma_c}{4G_c}\right) \tag{5.11}$$

and then the normalized separation energy is equal to

$$\frac{\Delta G}{G_c} = \frac{\kappa\sigma_c}{G_c}\left(1-\frac{\kappa\sigma_c}{4G_c}\right) \tag{5.12}$$

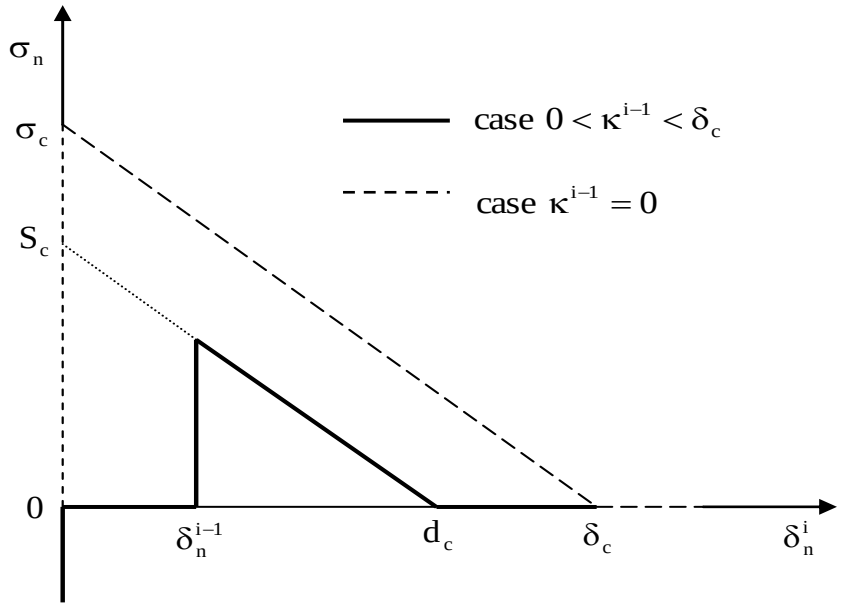

Figure 5.10 Schematic of cohesive law

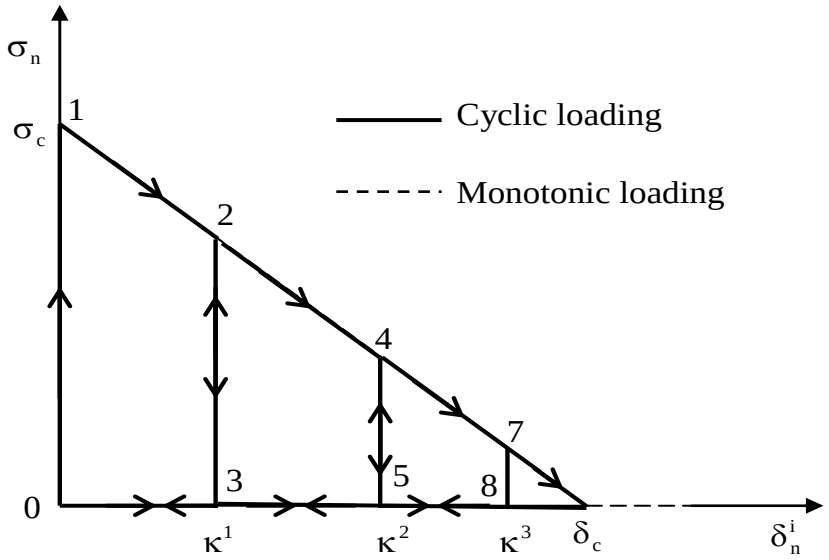

Figure 5.11 Evolution of traction during monotonic and cyclic loading with the cohesive-traction law

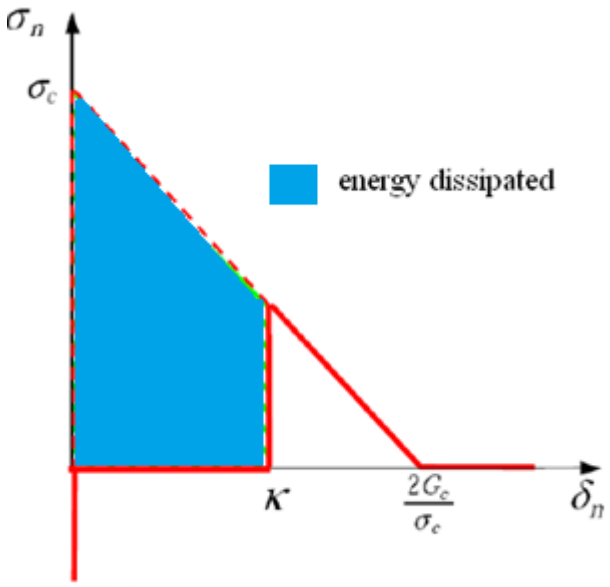

Figure 5.12 The energy dissipated in normal separation for the cohesive-traction law

5.3. Implementation of Cohesive Zone Model

5.3.1 Monotonic Loading

Crack propagation due to monotonic loading is presented here to demonstrate how a crack tip will moves along a defined crack path as load increase. It is shown that the cohesive interface element dissipates energy as normal separation occurs.

5.3.1.1 Model Description

In this present work, a model investigated by Mohanty [83] is considered having dimensions: 17.7 mm notch length, height h of 100 mm and width w of 52 mm. As a consequence of symmetry, only half of the model is considered as shown on Figure 5.13. Crack propagation is constrained to move along the axis of symmetry of the model. The elastic materials are used in this test case. The detail mechanical properties are shown in Table 5.1.

Table 5.1 Mechanical Properties for Monotonic Loading [84]

Young's Modulus E (MPa)	Yield Stress σ_y (MPa)	Poison's ratio	Toughness G_C (N/mm)	Critical Cohesive Traction σ_c (MPa)
72000	300	0.3	9.5	350

.

The size of cohesive interface element L_{cz} was introduced by [76] to generate the stable computation. He concluded that the size of cohesive interface element is no

more than 50 times the critical separation δ_c. The critical separation can be calculated from

$$\delta_c = \frac{2 \times G_c}{\sigma_c} = \frac{2 \times 9.5}{350} = 0.0543 \text{ mm}$$

Therefore it found that the maximum size of cohesive interface element is 2.7 mm.

In this study, the size of cohesive interface element is 0.1 mm. This cohesive interface of 210 elements is arranged along the axis of symmetry of the model. The model is meshed with quadratic triangular of 12680 elements as shown in Figure 5.14.

The stress loading is applied uniformly on the edge top of plate and is increasing from 0 to 60 MPa as a monotonic as shown in Figure 5.15.

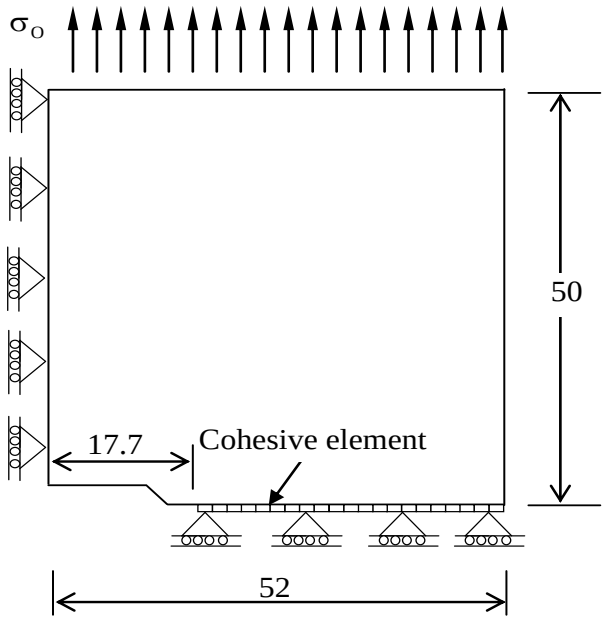

Figure 5.13 The dimension model

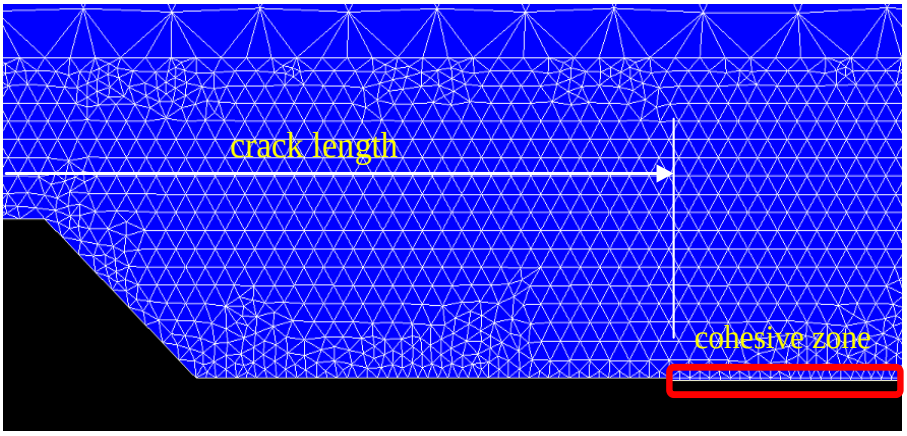

Figure 5.14 The cohesive element model in the finite element modeling

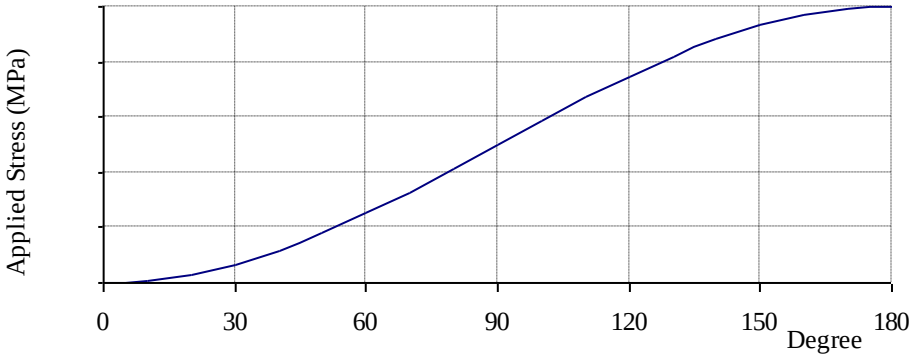

Figure 5.15 The model of applied loading

5.3.1.2 Results and Discussion

The stress distribution in front of the crack tip for different loading conditions is shown in Figure 5.16. It can be seen from the figure that a high stress level (red color) occurs at notch tip at the applied load of 10 MPa. As the loading increases up to 30 MPa, the highest stress level occurs at the first cohesive interface element. Further increase in load up to 60 MPa give rise to the high stress levels over few

cohesive interface elements and the highest stress level completely move from initial crack tip.

The incremental applied loading leads to the release of separation energy in a cohesive interface element. One the stress level has reached the critical cohesive traction as shown in Figure 5.17. The figure illustrates the distribution of normalized separation energy in the cohesive zone for the different applied loads.

Figure 5.18 shows the distribution of normalized normal traction σ_n/σ_c along the cohesive zone at an applied load of 60 MPa. As can be seen from figure, the lowest normal cohesive traction is at the first cohesive element. This phenomenon corresponds to the normal separation where in this position the separation energy has highest value as shown in Figure 5.17. As the crack growths, the normal cohesive traction acting at the crack tip will have already reached a critical value and subsequently continues to decrease down to zero at which point the crack tip separates completely. This phenomenon explains the mechanism of how the crack tip will move to the position where the normal traction has its highest value whilst normal separation energy has lowest value as shown in Figure 5.18.

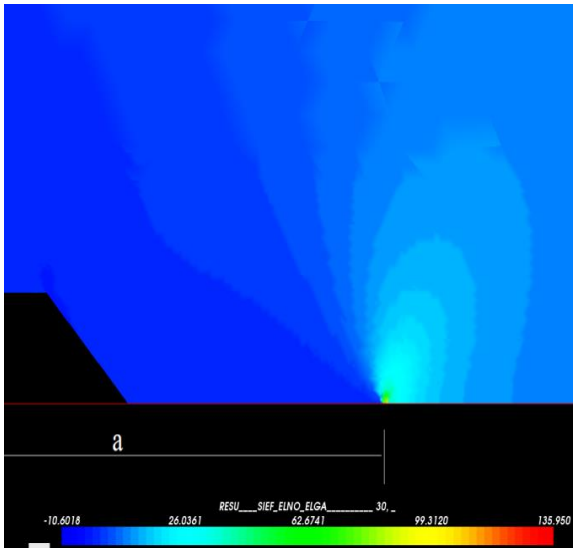

(a) 10 MPa

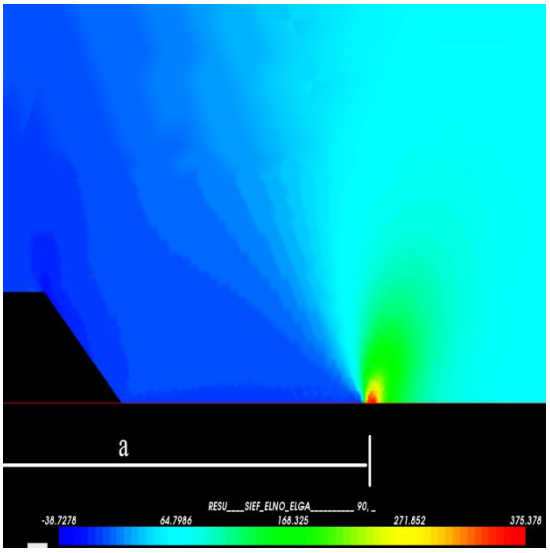

(b) 30 MPa

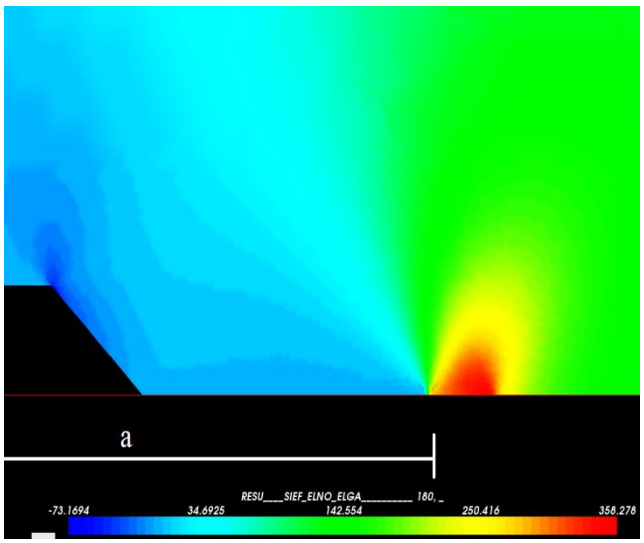

(c) 60 MPa

Figure 5.16 The stress distribution at crack tip for various loading condition

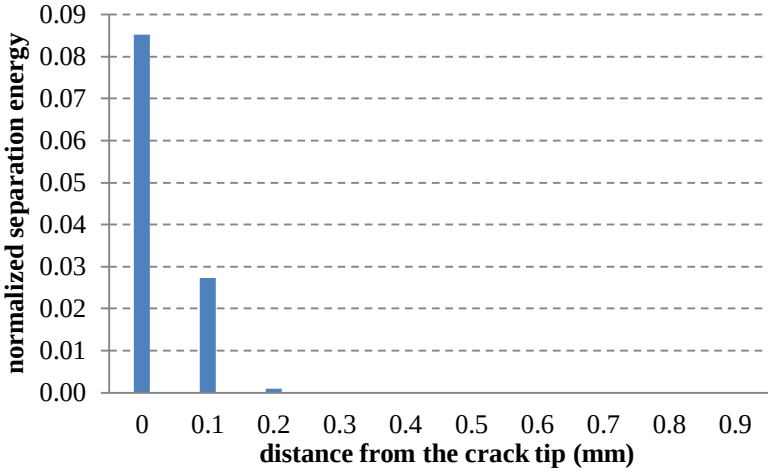

(a) 30 MPa

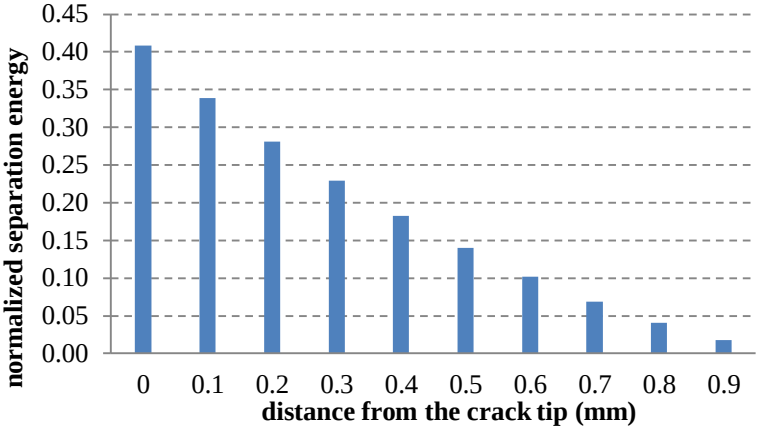

(b) 60 MPa

Figure 5.17 The distribution of normalized separation energy in cohesive zone

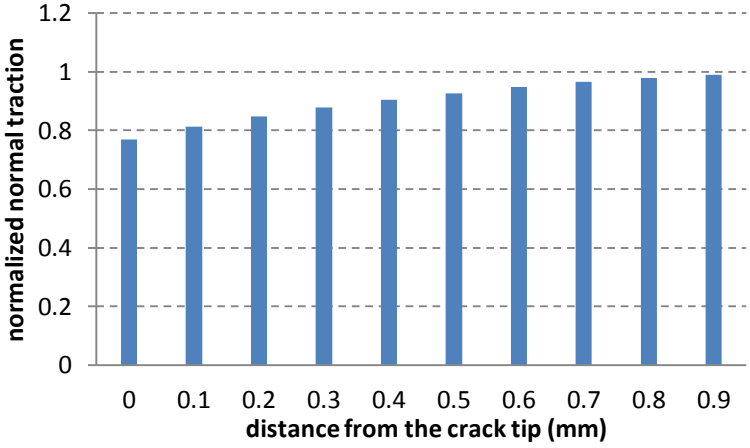

Figure 5.18 The distribution of normalized normal traction in cohesive zone for applied loading of 60 MPa

5.3.2 Cyclic Loading

In this analysis, crack propagation due to cyclic loading is presented. For constant amplitude loading (CAL), the effect of boundary conditions is discussed here. It can be shown that the boundary condition can affect the number of cycles for the crack propagation. For single overloading, the effect of overload is also discussed here.

5.3.2.1 Constant Amplitude Loading

Constant amplitude loading usually refers to a constant applied loading subject to component or materials containing a crack or flaw. The stress around crack tip due to the applied loading will be concerned to analysis the fatigue crack growth. In the traditional approach, the stress intensity factor [16] is one of critical parameter playing a major role in evaluating the fatigue crack growth. However, in the cohesive zone model, the cohesive energy in materials is one of importance parameter considered to see when the crack tip initiate.

5.3.2.1.1 Model Description

In the present work, the model is considered is the same as that presented in section 5.3.1.1. The mechanical properties of the material [84] used for linear elastic-plastic analysis are: E = 72 GPa, $\sigma_Y = 300\,\text{MPa}$, $\nu = 0.3$ and $G_{IC} = 9.5$ N/mm. The critical

cohesive traction σ_c of 350 MPa is taken for plane stress and the ultimate strength of 550 MPa.

The size of cohesive interface element and the meshed model has been explained in section 5.3.1.1. In the case of constant amplitude loading (CAL), a stress loading of 15 MPa is applied uniformly on the edge top of the plate as a sinusoidal function as shown on Figure 5.19(b) with a load ratio $R = S_{min} / S_{max} = 0$. The model has three different boundary conditions as shown in Figure 5.19(a), i.e.

1. Left edge is constrained in x direction, $D_x = 0$ and bottom edge is constrained in y direction $D_y = 0$, whilst right edge is free (LC).
2. Right edge is constrained in x direction, $D_x = 0$ and bottom edge is constrained in y direction, $D_y = 0$, whilst left edge is free (RC).
3. Node A is constrained in x and y direction, $D_x = 0$ and $D_y = 0$, whilst bottom edge is constrained in y direction, $D_y = 0$ (NC).

5.3.2.1.2 Results and Discussion

To calculate stress in y direction along crack path $\theta = 0$, Equation (3.1) may be used

$$\sigma_{yy} = \frac{K_I}{\sqrt{2\pi r}}$$

where r is distance from crack tip and K_I is the stress intensity factor depend on geometric model. The geometric model can be represented in term of boundary condition above which leads to [60]

1. $K_I = \sigma\sqrt{\pi a}\left(\sec\frac{\pi a}{W}\right)$ for LC boundary condition

2. $K_I = Y\sigma\sqrt{a}$ with

   $Y = 1.99 + 0.76\cdot\frac{a}{W} - 8.48\left(\frac{a}{W}\right)^2 + 27.36\left(\frac{a}{W}\right)^3$ for RC boundary condition and

   $Y = 1.99 - 0.41\cdot\frac{a}{W} + 18.7\left(\frac{a}{W}\right)^2 - 38.48\left(\frac{a}{W}\right)^3 + 53.85\left(\frac{a}{W}\right)^4$ for NC boundary condition.

The comparison of the stress distribution ahead of crack tip between analytical and numerical results is presented in Figure 5.20 to 5.22 for three different boundary conditions at the first maximum cyclic loading. It can be seen from the figures that at the crack tip, the stress from the two approach differs with the analytical prediction being infinite as consequence of singularity $1/\sqrt{r}$ whilst numerical prediction has a value less than critical cohesive traction ($\sigma_c = 350\,\mathrm{MPa}$) which shows that the local damage has occurred at the crack tip. In this condition, the location of crack tip is not coincident since local damage ahead of crack tip have occurred in the cohesive zone which has induced stress levels which are less than critical traction. However, this case study reveals that generally the numerical and analytical results show good

agreement in the stress distribution ahead of the crack tip. This result provides some justification for using singular analytical distribution just ahead of the crack tip [13].

Figure 5.23 presents the fatigue crack growth curve for three difference typical boundary condition. As can be seen from the figure, the NC constraint condition has the highest fatigue crack growth rate and the lowest is the LC constraint condition. The high stress levels at the crack tip for the NC constraint have produced the low number of cycles to crack growth. In contrast, for the LC constraint condition, the low stress levels ahead of the crack tip means that a large number of cycles are required to extend the crack.

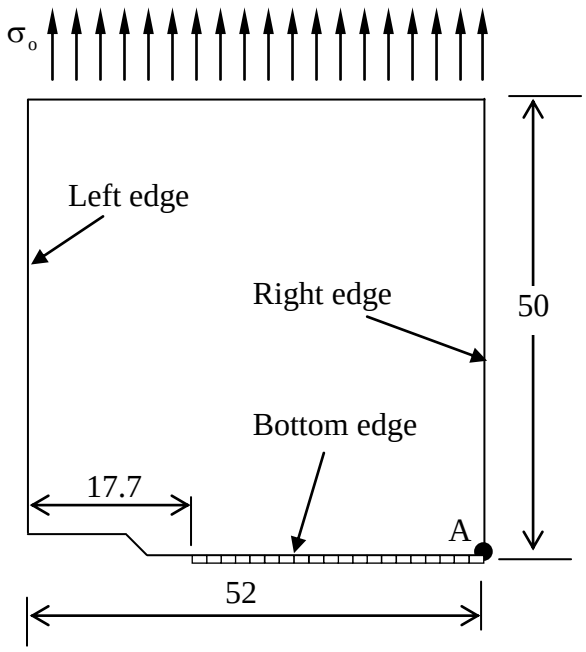

(a) dimensions and boundary condition

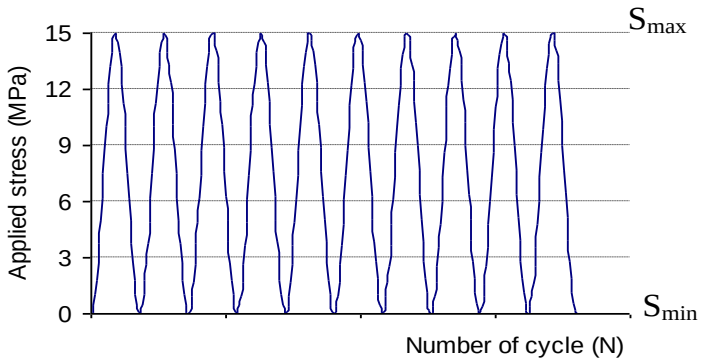

(b) constant amplitude loading

Figure 5.19 The schematics of models

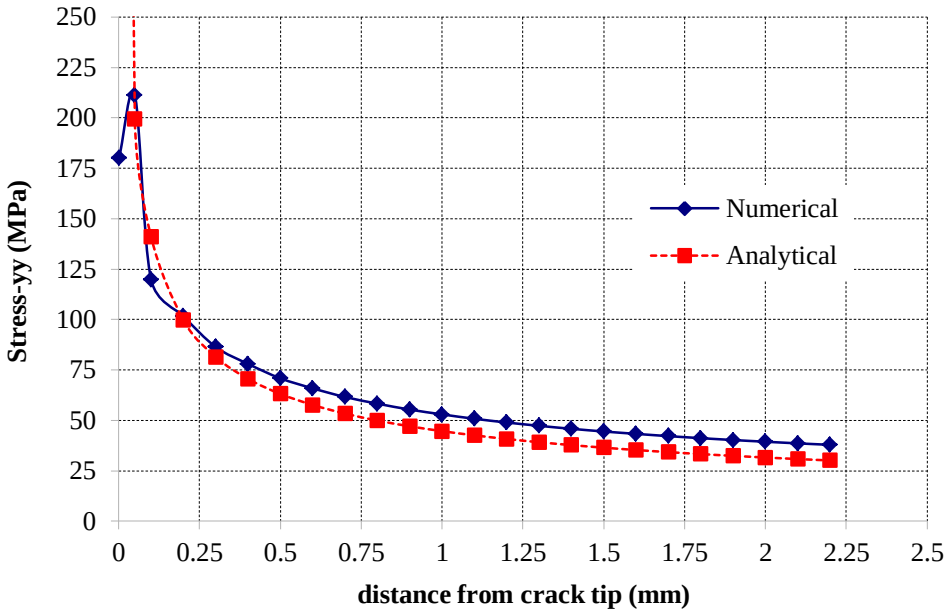

Figure 5.20 The stress distribution in ahead crack tip for numerical and analytical results for LC condition

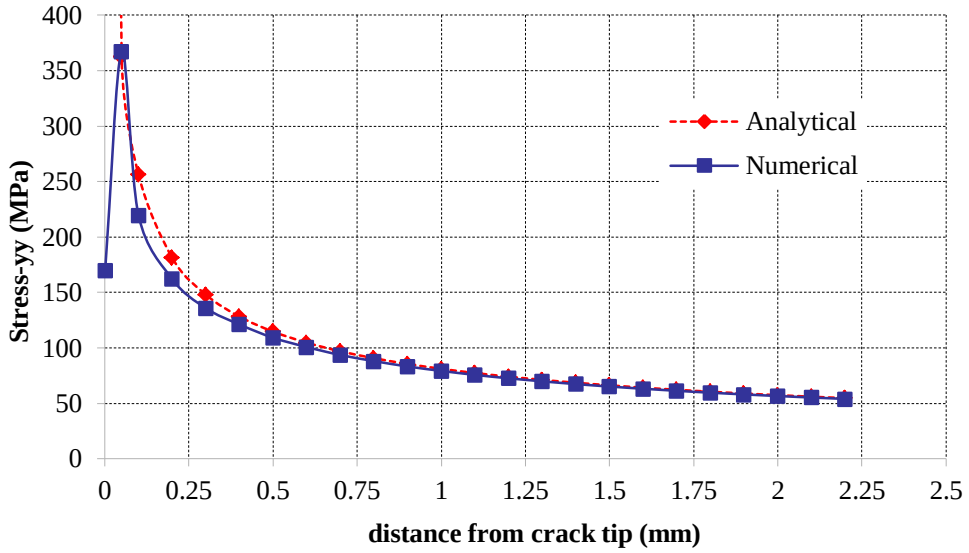

Figure 5.21 The stress distribution in ahead of crack tip for numerical and analytical results for NC condition

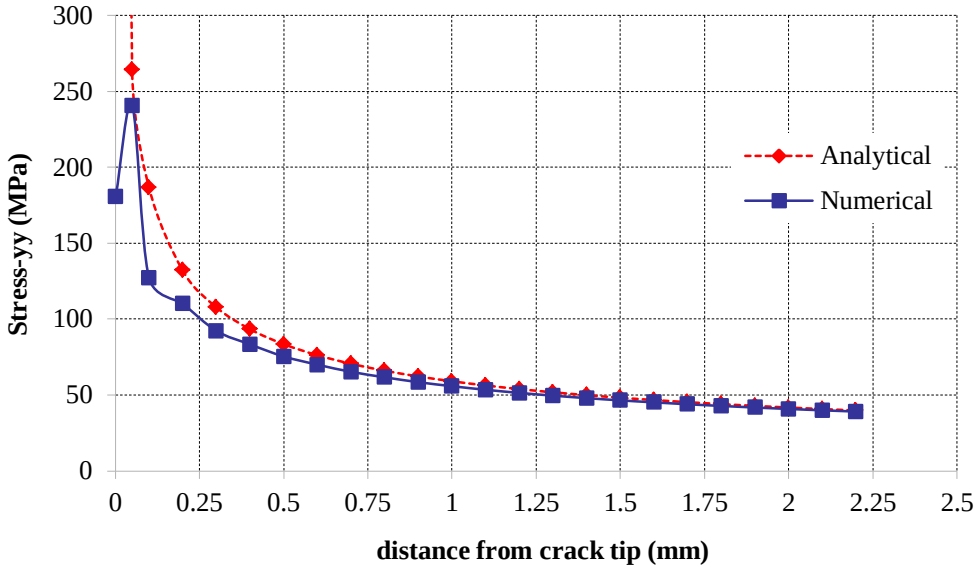

Figure 5.22 The stress distribution in ahead crack tip for numerical and analytical results for RC condition

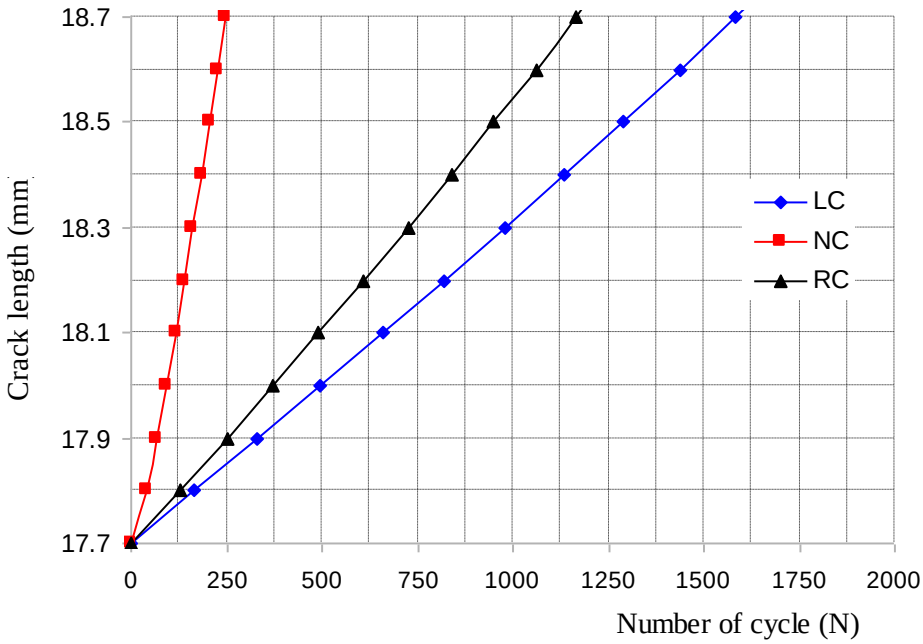

Figure 5.23 The effect of various boundary conditions for fatigue crack growth

5.3.2.2 Single Overloading

Single overloading is typically characterised by one high peak load and then followed by the lower constant amplitude loading. The overloading may lead to retardation or acceleration of fatigue crack growth. This phenomenon is a significant unexplained aspect in fatigue crack growth [63]. Most approaches proposed and developed are empirical which account for the retardation phenomena by means of a plastic zone created due to the high peak loading [46]. In this study, the phenomena overloading is investigated by using the cohesive zone model. The effect of overloading ratio is also studied.

5.3.2.2.1 Model Description

In this study case, the model is considered is the same as that presented in section 5.3.2.1.1. The dimension and mechanical properties are identical and the boundary conditions applied are the constraint left edge and bottom edge, (LC) as shown in Figure 5.24(a). A single stress overloading (S_{ol}) of 22.5, 27.0 and 30.0 MPa is applied at the first cycle and a stress loading (S_{max}) of 15.0 MPa is applied uniformly on the top edge of the plate as a sinusoidal function as shown in Figure 5.24(b). The some overload ratio $SOL = S_{ol}/S_{max} = 1.5,\ 1.8$ and 2.0 and a load ratio $R = S_{min}/S_{max} = 0$ is applied.

5.3.2.2.2 Results and Discussion

Figure 5.25 shows the fatigue crack growth curve for different overloading ratios (SOL). The fatigue crack growth line without overloading is identified by the label SOL-1. The various fatigue crack growth curve for different overloading ratios is shown. It can be seen from the figure that the application of single overloading at the initial crack length may cause the fatigue crack growth retardation for all the overloading ratios considered. The number of cycles increases with overloading ratio (SOL). The largest fatigue crack growth retardation is resulted from the overloading ratio (SOL) of 2.0.

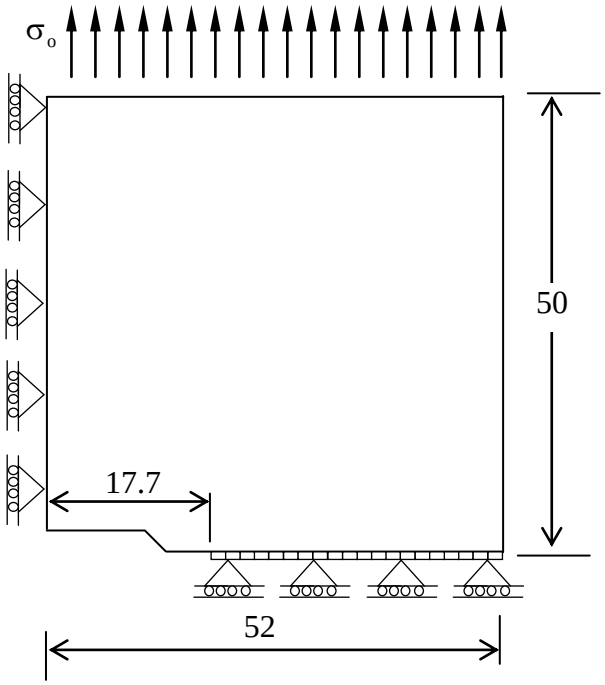

(a)) Dimensions and boundary condition

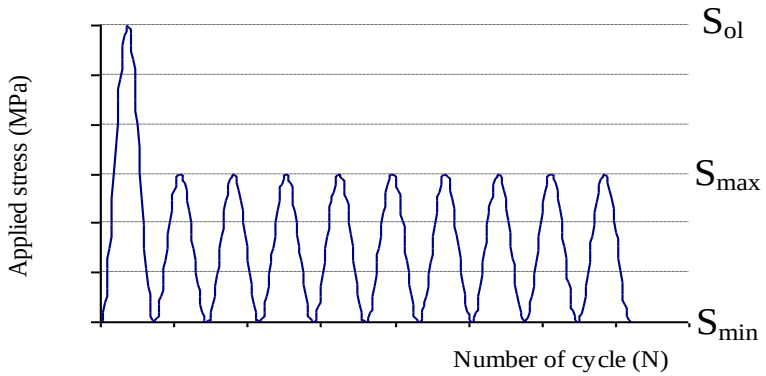

(b)) Single overloading

Figure 5.24 The schematics of models:

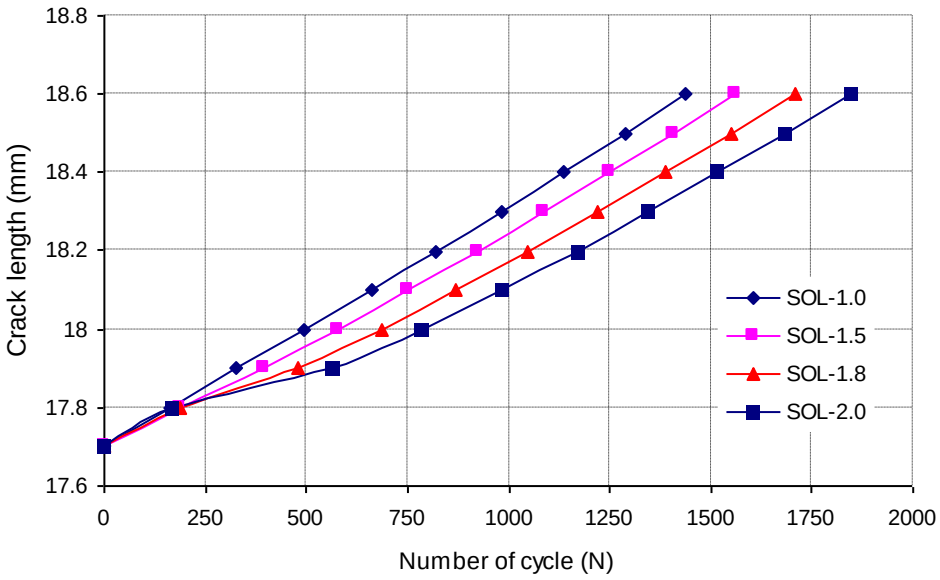

Figure 5.25 The effect of various single overloading ratio (SOL) in crack growth rate

5.3.2.3 The Effect of Critical Traction in Cohesive Law

In cohesive zone model, three parameters are involved in the evaluating of fatigue crack growth i.e. critical cohesive traction σ_c, cohesive energy or toughness and critical separation (δ_c). These parameters relate to the materials behavior in damage zone ahead of the crack tip. Since toughness is a well-established material property, the critical cohesive traction or normal separation is parameters which need to be specified. However, the critical cohesive traction σ_c is a parameter which dictates to some extent the plastic behavior at damage zone ahead of the crack tip. Its value is required to be higher than the yield stress σ_Y for yielding to occur at the crack tip. The plastic zone at the crack tip is recognized to be one of the most important quantities regarding for the retardation and induce crack closure [5].

It is of interest therefore to consider the effect of various critical cohesive tractions σ_c on the fatigue crack growth retardation.

5.3.2.3.1 Model Description

The same model explained in section (5.3.2.2.1) is used here. For single cycle overloading, a single stress overloading (S_{ol}) of 26.25 MPa is applied at the first cycle and then followed by a stress loading (S_{max}) of 15.0 MPa applied uniformly on the top edge of the plate as a sinusoidal function as shown on Figure 5.24(b). An overload ratio $SOL = S_{ol} / S_{max} = 1.75$ with a load ratio $R = S_{min} / S_{max} = 0$ is applied. The material properties used shows in Table 5.2. In this test case, the various critical traction (CS) used to examine the effect on crack propagation are 310 MPa, 320 MPa, 330 MPa, 340 MPa and 350 MPa, respectively.

Table 5.2 Mechanical Properties

Young's Modulus E (MPa)	Yield Stress σ_{ys} (MPa)	Poison's ratio υ	Toughness G_{IC} (N/mm)
72000	300	0.3	9.5

5.3.2.3.2 Results and Discussion

The crack length with respect to the number of cycle in various critical cohesive tractions σ_c is depicted in from Figure 5.26 to 5.30. The figures show the comparison of fatigue crack growth without overloading (SOL-1) and with overloading (SOL-1.75). It can be seen from these figures that for the critical

cohesive traction CS-310 and CS-320 MPa, there is no retardation for an applied single overload as shown in Figure 5.26 and 5.27, respectively. The phenomenon of retardation appears for the critical cohesive traction of 330 MPa and 340 MPa, and is particularly occurs when the critical stress value is 350 MPa as shown in Figure 5.28, 5.29 and 5.30, respectively.

Figure 5.31 shows the relationship between the various critical cohesive tractions and number of cycle to extend a crack. It can be seen from the figure that number of cycle increase significantly for the highest critical cohesive traction at the longest crack length. The relationship between varying critical cohesive traction and the number of cycle is nonlinear for given crack length.

5.4. Summary

One of the more significant findings to emerge from this case study is that the cohesive zone model in Code_Aster can simulate the effect of a single overloading to retard the crack growth rate. If the overloading ratio increases, the stress level at crack tip will increase and larger plastic zone near the crack tip will form. As a consequence, the number of cycles required for crack growth also can increase.

For the case study pertaining for various critical cohesive tractions σ_c, it has been found that generally the critical cohesive traction affects the fatigue crack growth retardation. If the value of critical traction is close to the yield stress, it will not retard fatigue crack growth. Increasing the value of critical cohesive traction increases the extent of plastic zone at the crack tip which causes the fatigue crack growth to retard.

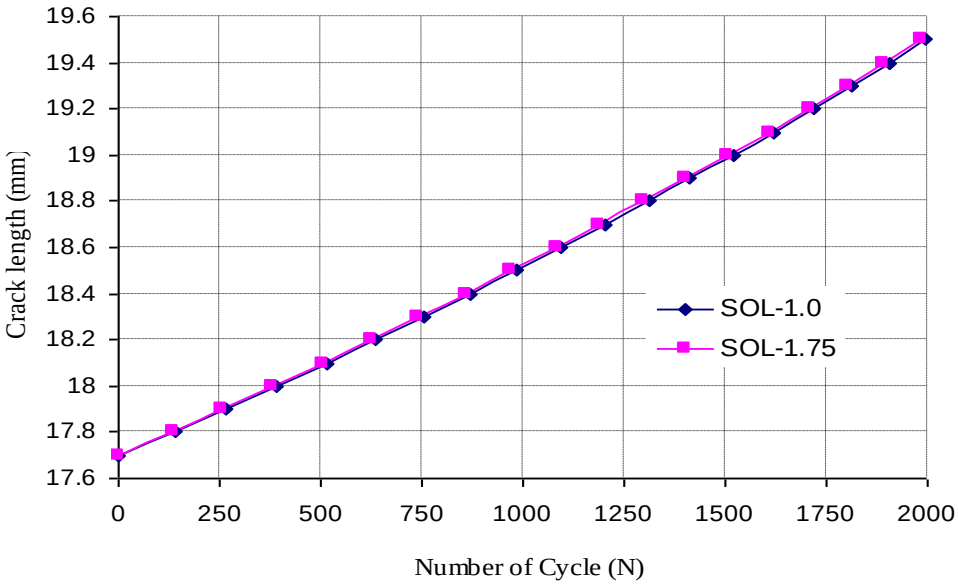

Figure 5.26 The comparison of the crack growth rate for difference type of loading at critical cohesive traction (CS) of 310 MPa

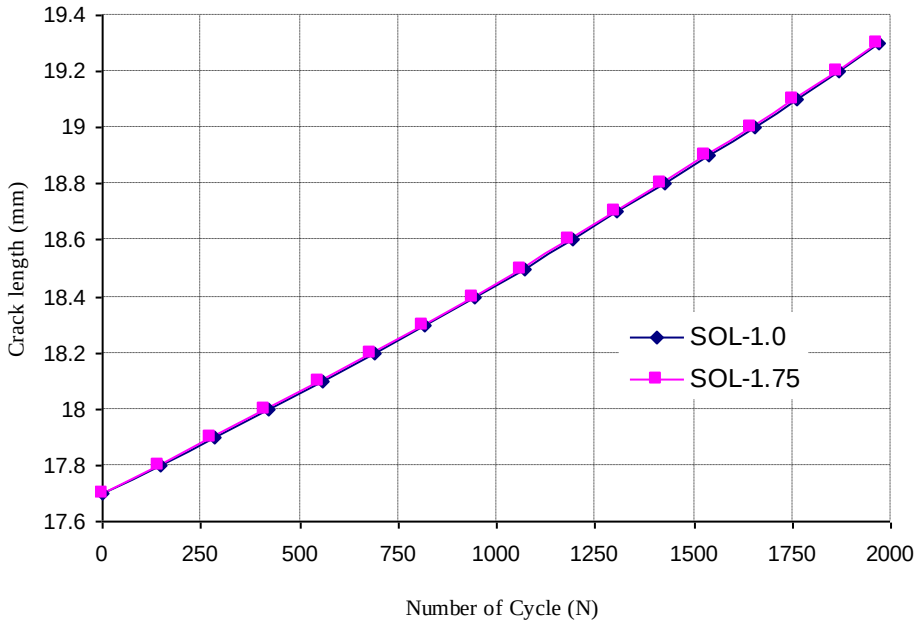

Figure 5.27 The comparison of the crack growth rate for difference type of loading at critical stress (CS) of 320 MPa

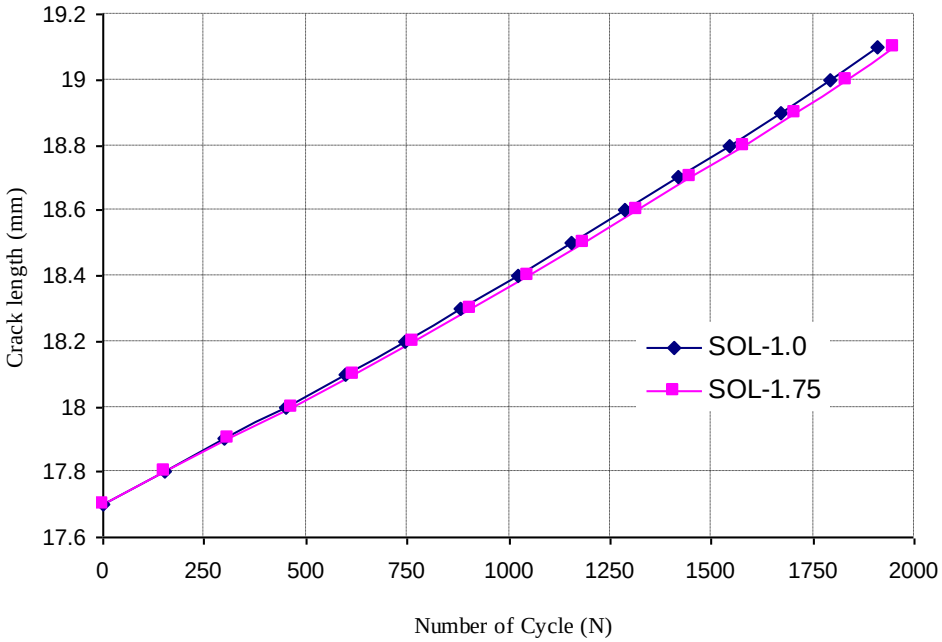

Figure 5.28 The comparison of the crack growth rate for difference type of loading at critical cohesive traction (CS) of 330 MPa

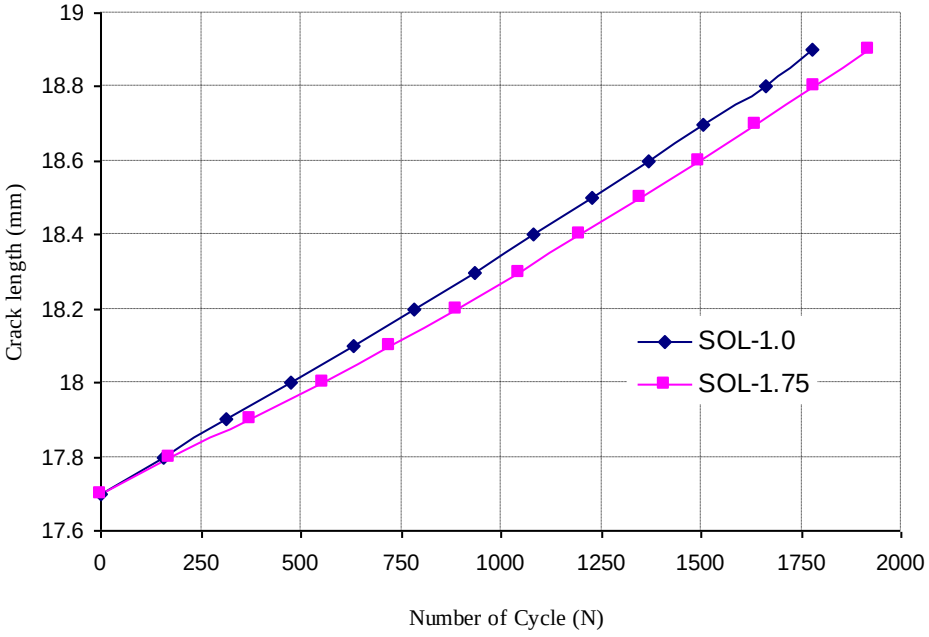

Figure 5.29 The comparison of the crack growth rate for difference type of loading at critical cohesive traction (CS) of 340 MPa

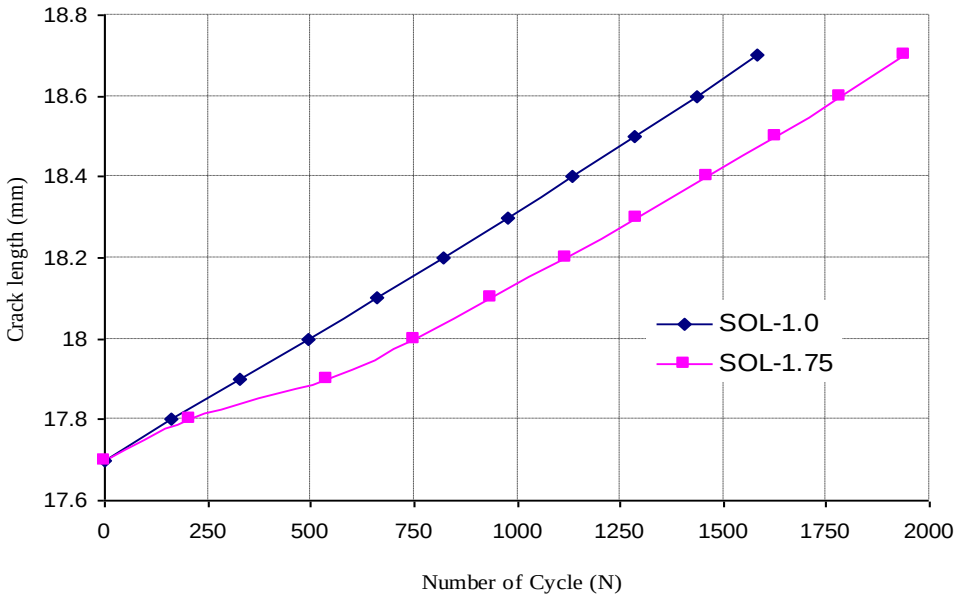

Figure 5.30 The comparison of the crack growth rate for difference type of loading at critical cohesive traction (CS) of 350 MPa

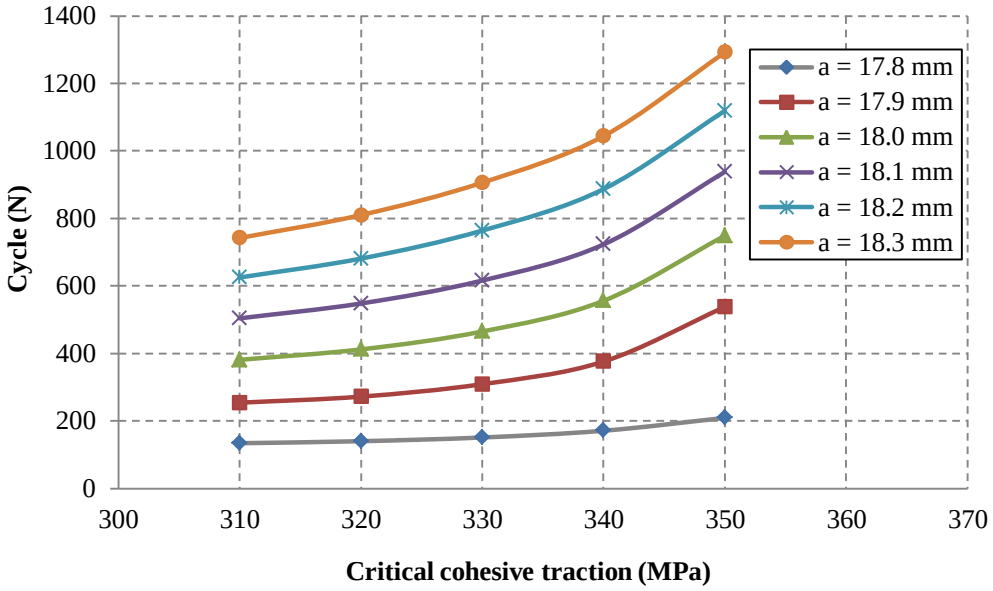

Figure 5.31 The relationship between critical cohesive traction (CS) and number of cycles for different crack length

Chapter 6

The Effect of Variable Toughness in Fatigue Crack Growth

6.1. Introduction

The presence of cracks, flaws or any other sharp discontinuity may invariably reduce the strength of a component or structure. An initial crack will propagate steadily from its initial size to a critical crack size at which final failure occurs under cyclic loading. Fatigue failure is therefore defined as a progressive, localised, and permanent structural damage occurring when a material is subjected to cyclic loading.

In the fatigue failure mechanism, the crack will growth if the energy release rate reaches the critical energy release rate [16] as known as toughness G_c. Fracture toughness is a material property which quantifies the ability of a material containing crack to resist fracture. A material has high fracture toughness it will probably

undergo ductile fracture. Meanwhile, brittle fracture is as a characteristic of materials with low fracture toughness.

In this study, the relationship between the fatigue crack growth rate and the stress intensity factor is presented. The stress intensity factor range is calculated from an equation introduced by Irwin [16] and the fatigue crack growth rate is captured by the cohesive zone model. The Paris law [1] is adopted to evaluate the effect of various toughness value on fatigue crack growth.

In this chapter, varying toughness approach is assumed with fixed critical cohesive traction. The effect of varying toughness for fatigue crack growth and stress distribution along the crack path is shown. The functional relationship between artificial toughness and number of cycles for a fixed incremental crack length is established and gives rise to new approach to for reducing computational time. This method is investigated with an objective to reduce the number of cycles required for crack growth analysis. Since energy criteria can be used in crack growth analysis, it is of interest therefore to examine the effect of varying toughness on elastic and plastic energy.

6.2. Fatigue Crack Growth Model

Fatigue failure process consists of several distinct processes involving initial cyclic damage (cyclic hardening or softening), crack initiation, crack growth, and final catastrophic failure or instability. The crack growth phase considers the concepts of

linear elastic fracture mechanics. Generally, fatigue crack growth in fracture mechanics can be described by schematic diagram as illustrated in Figure 6.1. Typical empirical fracture mechanics models relationship between to the stress intensity factor range ΔK and the fatigue crack growth rate da/dN. The stress intensity factor range can be determined by

$$\Delta K = K^{max} - K^{min} = (1-R)K^{max} \tag{6.1}$$

where $R = K^{min}/K^{max}$ here but presumable can be related to load ratio because of linearity. The fatigue crack growth rate is defined as the crack extension per number of cycle da/dN. The relationship between the fatigue crack growth rate and the stress intensity factor is commonly represented in a log-log diagram as shown in Figure 6.1. According to the curve shape, the fatigue crack growth rate can be divided into three regimes. In regime A, there is a threshold value, K_{th}, where below this value, cracks do not propagate or crack growth is ignored. Above the threshold value, crack growth increase relatively quickly. Regime B defines a stable crack growth region generally is characterized by linear part of the log-log curve. Finally, in regime C, the crack growth rate rises to an asymptote that corresponds to critical fracture toughness value K_c.

There are some empirical or semi-empirical mode describe all region of the crack propagate rate curve by crack growth law. However, only the Paris law [1] is widely used and accepted. The Paris law describes only the linear portion of the curve (Regime B). According to this law, the crack growth rate relates to the stress intensity factor range by a power law that can be expressed as

$$\frac{da}{dN} = C(\Delta K)^m \tag{6.2}$$

where the material parameter C and m depend on mode ratio and must be determined experimentally. The stress intensity factor range ΔK depend on the loading conditions and also on crack length

6.3. Toughness in Cohesive Zone Model

In the cohesive zone model, toughness G_c is recognized as the critical energy release rate, where in the traction-separation curve, the toughness is defined as the area under the curve. In the traction-separation law, when the traction is reduced to zero, new surface is formed. It considers there the variation of toughness with a fixed critical cohesive traction σ_c, then the area under the curve has a different area as shown in Figure 6.2. The "real" toughness is noted as the area under curve for the continuous line. Since the toughness can be expressed as

$$G_c = \frac{1}{2}\sigma_c\delta_c \tag{6.3}$$

the varying toughness with fixed critical cohesive traction σ_c has a relationship between critical normal separation, so if $\delta_{c1} < \delta_{c2} < \delta_{c3} < \ldots < \delta_c$, then $G_{c1} < G_{c2} < G_{c3} < \ldots < G_c$ as shown in Figure 6.2. It is important to appreciate that the critical cohesive traction σ_c has important influence on the extent of plasticity at the crack tip, so it is not free for variation unlike δ_c

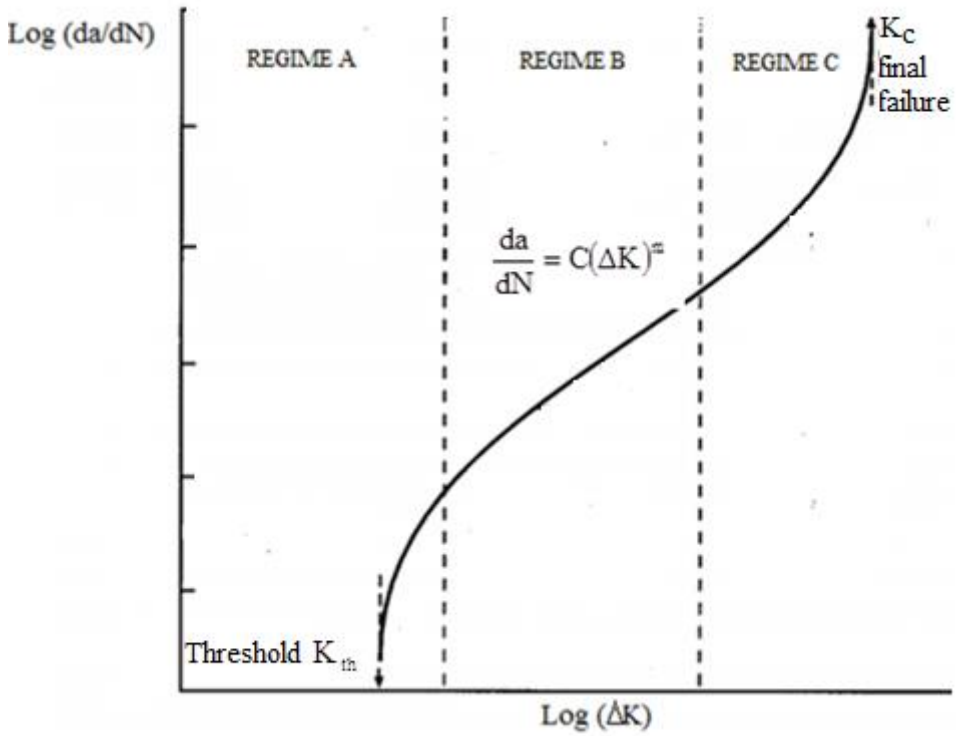

Figure 6.1 Fatigue crack growth rate curve

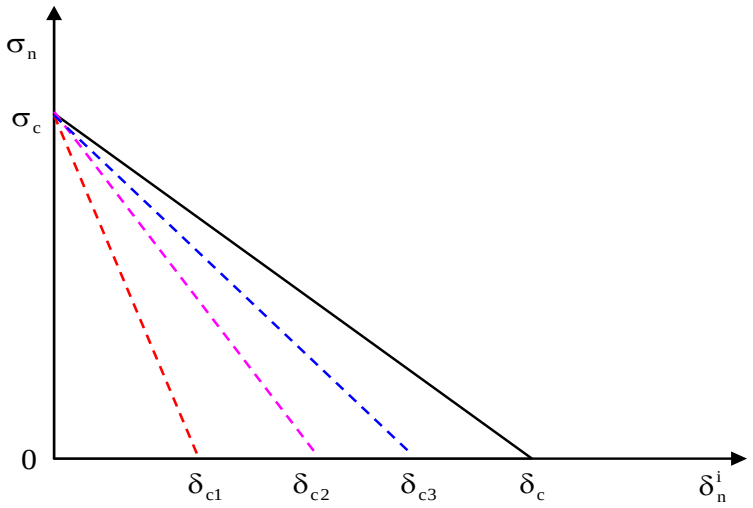

Figure 6.2 Schematics of traction-separation law for varying toughness in fixed critical cohesive traction

The relationship between number of cycle and toughness [35-37] is of the form

$$\frac{da}{dN} = \frac{1}{G_c}\frac{dW}{dN} \tag{6.4}$$

where dW/dN is the total plastic energy per cycle.

However, for a cohesive zone model consideration of the separation energy dissipated per cycle E_{sp} leads to the relationships:

$$\frac{da}{dN} = \frac{1}{G_c}\frac{dW_{sp}}{dN} = \frac{E_{sp}}{G_c} \tag{6.5}$$

which can be integrated under the assumption of invariant E_{sp} to provide a linear relationship between the number of cycles and toughness of the form

$$\Delta N = \frac{G_c}{E_{sp}}\Delta a \tag{6.6}$$

This can be further modified with substitution of the identify $G_c = 0.5\sigma_c\delta_c$ to give

$$\Delta N = \frac{\sigma_c\delta_c}{2E_{sp}}\Delta a \tag{6.7}$$

Equation (6.7) shows that if the increment in crack length Δa is assumed constant along with a fixed value of critical cohesive traction σ_c, that a reduction of critical separation δ_c provides a linear decrease in the number of cycles to propagate a crack.

6.3.1 Model Description

In this analysis, a test model which is adopted from [83] consisting of a 17.7 mm crack length a with 100 mm of height (h) and 52 mm of width w is considered. As a

consequence of symmetry, only half of the model is considered as shown in Figure 6.3(a). The crack is assumed to propagate along the axis of symmetry of the model. The linear elastic-plastic materials are used in this test case. The mechanical properties of the material used for linear-elastic analysis are: Young's modulus E = 72 GPa, the yield stress σ_Y = 300 MPa, and poison ratio $\nu = 0.3$ The critical cohesive traction σ_c is fixed in 340 MPa with four different toughness (G_c) consist of 9.5, 12.5, 15.0 and 18.5 N/mm. The plastic modulus (E_T) is set to 1.39 GPa is represented a linear isotropic hardening. In the case of constant amplitude loading (CAL), a stress loading of 12.5, 15, 17.5, 20, and 22.5 MPa is applied uniformly on the edge top of plate as a sinusoidal function as shown on Figure 6.3(b). A load ratio $R = S_{min} / S_{max} = 0$ is applied for all tests. The boundary conditions is constrained node A in x and y direction, $D_x = 0$ and $D_y = 0$, whilst bottom edge is constrained in y direction, $D_y = 0$.

The size of cohesive interface element L_{cz} is no more than 50 times the critical separation value δ_c [76]. The critical separation can be calculated

$$\delta_c = \frac{2 \times G_c}{\sigma_c} = \frac{2 \times 9.5}{340} = 0.0559 \text{ mm}$$

Therefore it found that the maximum size of cohesive interface element is 2.8 mm.

In this study, the size of cohesive interface element is 0.1 mm. This cohesive interface of 210 elements is therefore arranged along this axis of symmetry of the model. The model is meshed with 12680 quadratic triangular elements.

6.3.2 Results and Discussion

The effect of various toughness values on fatigue crack growth can be shown from Figure 6.5 to 6.9 for different applied loads. It can be seen from all figures that the relationship between incremental crack length and number of cycles is linear for all toughness. This relationship can be expressed in linear regression. Since the fatigue crack growth rate is defined as the incremental crack length per number of cycle (da/dN), from the linear regression equation, the fatigue crack growth can defined as the slope of equation as shown in Table 6.1.

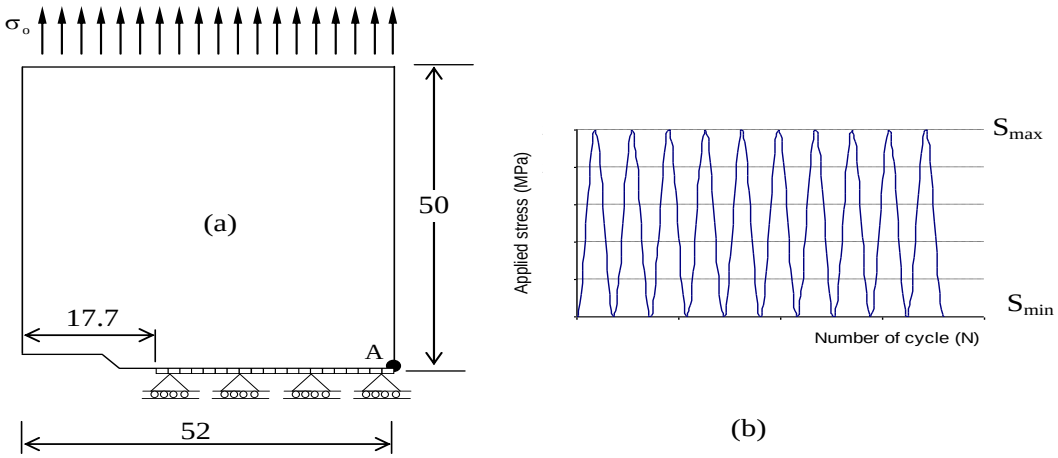

Figure 6.3 The schematics of models: (a) dimensions and boundary condition (NC) (b) constant amplitude cyclic loading (CAL)

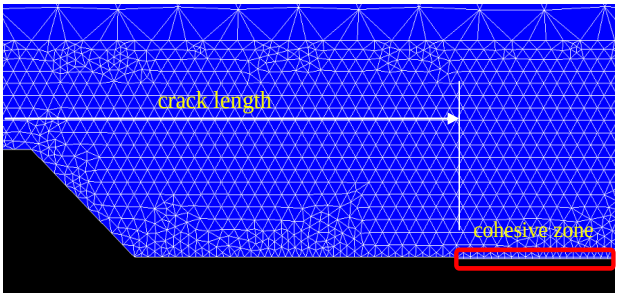

Figure 6.4 The cohesive element model in Code_Aster

As Table 6.1 shows that the highest toughness of 18.5 N/mm has the smallest fatigue crack growth rate of 0.0008 mm/cycle for the applied loading of 12.5 MPa. In addition, the highest toughness has the smallest fatigue crack growth rate for all applied loads. In contrast, the smallest toughness 9.5 N/mm has the largest fatigue crack rate of 0.0179 mm/cycle for 22.5 MPa. Moreover, the smallest toughness of 9.5 N/mm has the largest fatigue crack rate for all applied loading.

Table 6.1 Fatigue crack growth rate for different toughness value

Loading MPa	**ΔK**	**Fatigue crack growth rate (da/dN) (mm/cycle)**			
		G_c = 9.5 N/mm	**G_c = 12.5 N/mm**	**G_c = 15.5 N/mm**	**G_c = 18.5 N/mm**
12.5	170.89	0.0018	0.0013	0.0010	0.0008
15.0	204.50	0.0036	0.0027	0.0022	0.0018
17.5	237.92	0.0066	0.0049	0.0040	0.0033
20.0	271.14	0.0115	0.0086	0.0069	0.0057
22.5	305.03	0.0179	0.0135	0.0107	0.0089

In order to determine the Paris law parameter, the formulation from Equation (6.2) should be expressed in log-log equation of the form

$$\log\left(\frac{da}{dN}\right) = m\log(\Delta K) + \log(C) \tag{6.8}$$

The complete results from the calculation data of Table 6.1 can be seen in Table 6.2. By using the linear regression, the parameter can be determined as shown in Table 6.3.

Table 6.2 log-log fatigue crack growth data

Log (ΔK)	Log (da/dN) (mm/cycle)			
	G_c = 9.5 N/mm	G_c = 12.5 N/mm	G_c = 15.5 N/mm	G_c = 18.5 N/mm
2.2327	-2.7447	-2.8861	-3.0000	-3.0969
2.3107	-2.4437	-2.5686	-2.6576	-2.7447
2.3764	-2.1805	-2.3098	-2.3979	-2.4815
2.4332	-1.9393	-2.0655	-2.1612	-2.2441
2.4843	-1.7471	-1.8697	-1.9706	-2.0506

Table 6.3 Paris law parameter for different toughness

Parameter	G_c = 9.5 N/mm	G_c = 12.5 N/mm	G_c = 15.5 N/mm	G_c = 18.5 N/mm
m	3.99	4.05	4.09	4.15
C	2.1677E-12	1.16E-12	0.75E-12	0.439E-12

The fatigue crack growth rate for five different stress intensity factors (ΔK) via applied loading and four different toughness value (G_c) is also shown in Figure 6.10. The figure illustrate Paris law regime where in this area fatigue crack growth rate should be stable condition. It can be seen from figure that the fatigue crack growth rate has linear relationship with applied loading. The smallest toughness of 9.5 N/mm has the highest fatigue crack growth rate $\left(C = 2.1677 \times 10^{-12}\right)$ for all applied loading. In contrast, the highest toughness of 18.5 N/mm has the smallest fatigue crack growth rate $\left(C = 0.439 \times 10^{-12}\right)$. In addition, the figure also shows that the Paris's law parameter m is around 4 for all toughness G_c.

Figure 6.11 shows the relationships between the number of cycles and variable toughness for every incremental crack length in an applied load of 22.5 MPa. It can be seen from figure that the relationships are linear for given incremental crack length.

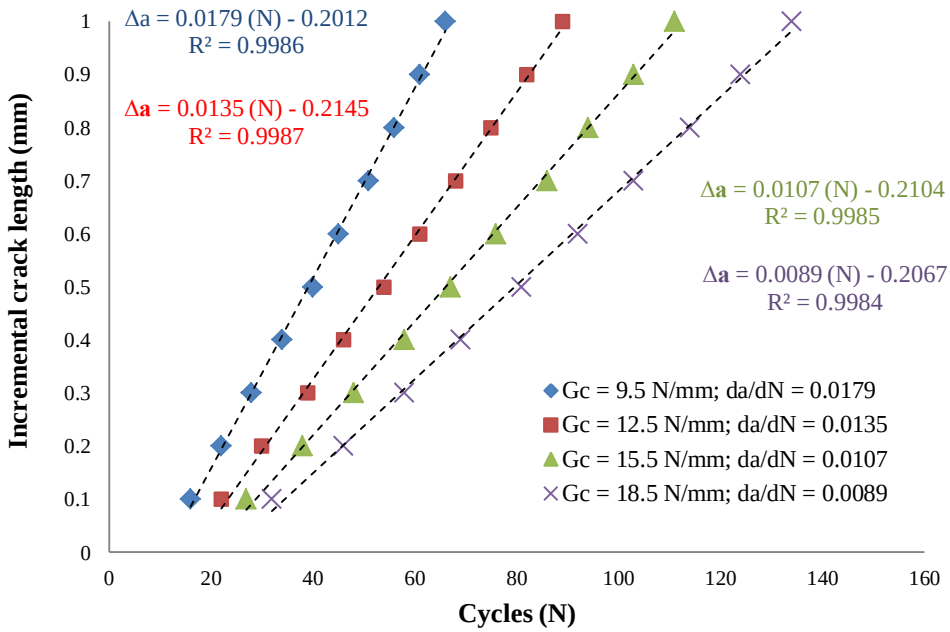

Figure 6.5 The effect of variable toughness in fatigue crack growth for an applied load of 22.5 MPa

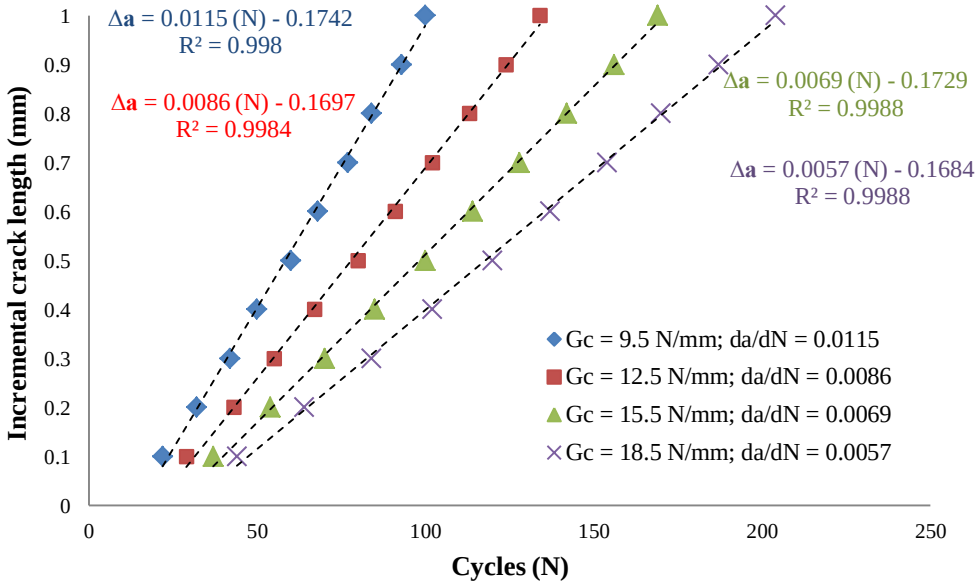

Figure 6.6 The effect of variable toughness in fatigue crack growth for an applied load of 20.0 MPa

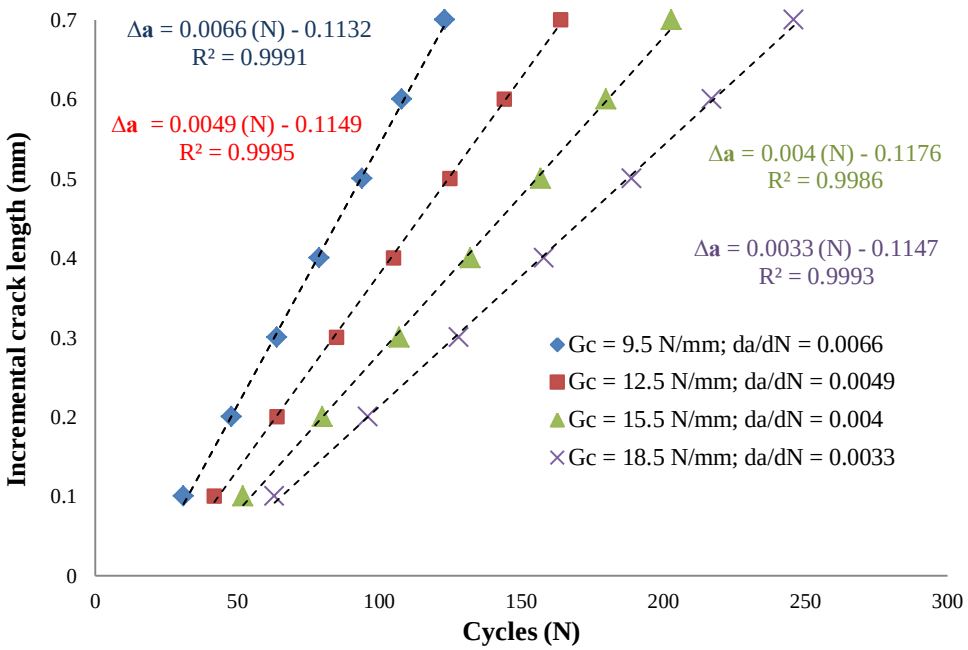

Figure 6.7 The effect of variable toughness in fatigue crack growth for an applied load of 17.5 MPa

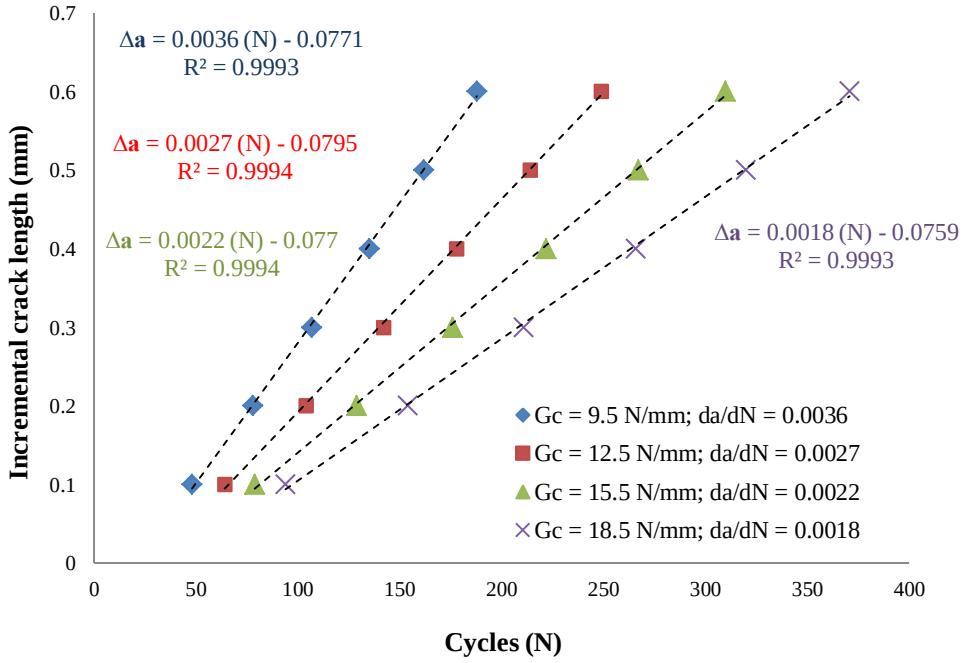

Figure 6.8 The effect of variable toughness in fatigue crack growth for an applied load of 15.0 MPa

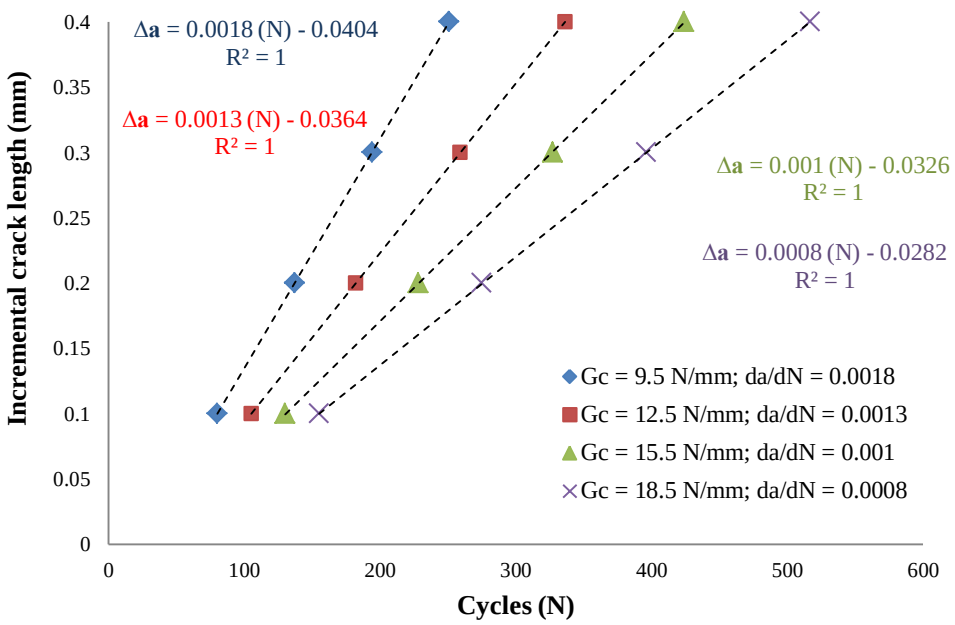

Figure 6.9 The effect of variable toughness in fatigue crack growth for an applied load of 12.5 MPa

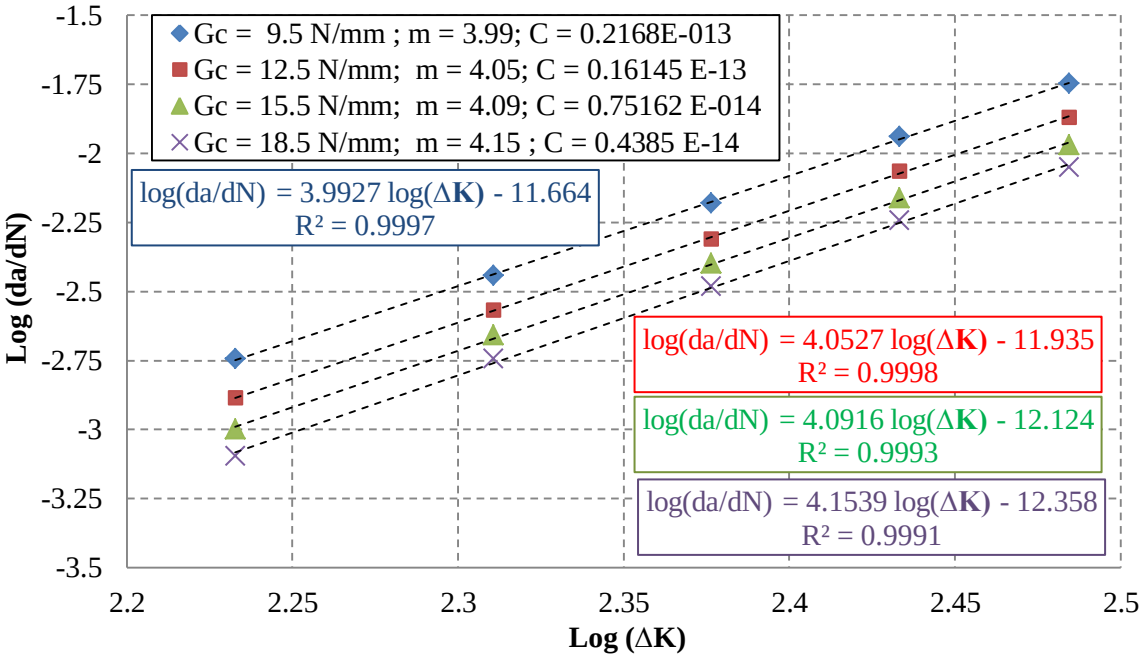

Figure 6.10 The effect of variable toughness for the fatigue crack growth rate

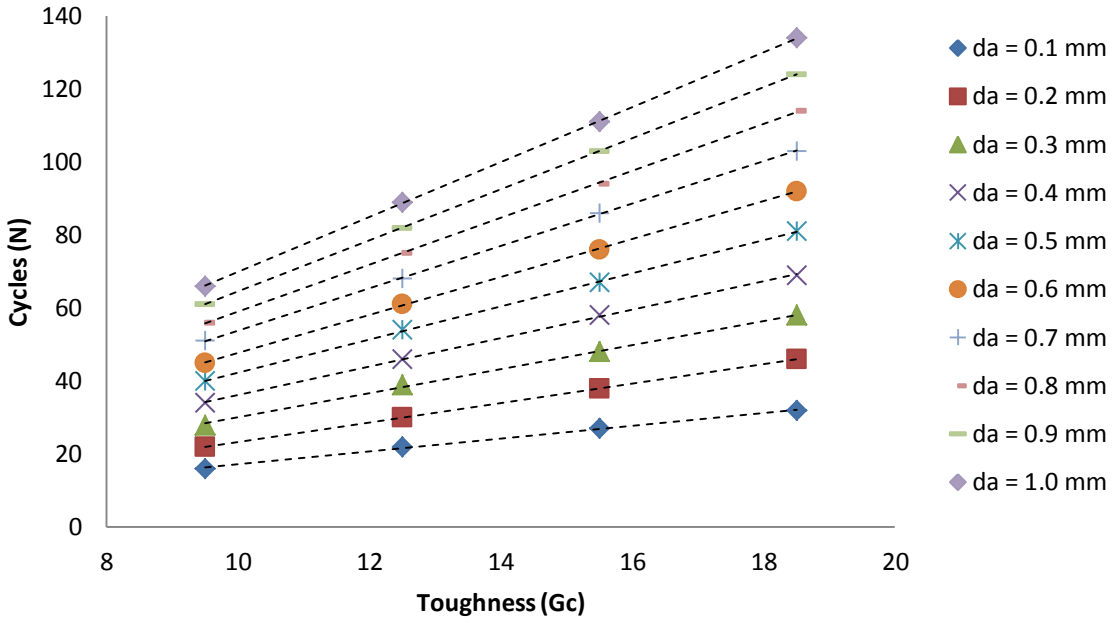

Figure 6.11 The relationships between the number of cycles and variable toughness for every incremental crack length and an applied load of 22.5 MPa

6.4. Stress Distribution in Fatigue Crack Growth

The more ductile material undergoes the more extensive plastic deformation in region high stress concentration. A fracture caused by a crack is nearly always preceded by at least a small amount of plastic deformation at the crack tip. This deformation plays a crucial role in fracture process [34,35]. It is therefore important to examine the stress distribution along a crack path during fatigue growth. However in the cohesive zone model, if the region undergoes high stress which its value is beyond the critical traction value, the region suffers micro structural damage and consequently the stress level in this region is lowered. In fatigue failure, the microstructural damage accumulates to facilitate crack propagation.

As can be seen in Figure 6.12, there are two regions which are identified as the damage zone and the undamaged zone. According to linear elastic fracture mechanics (LEFM) the infinite stress at the crack tip so it is expected that a crack tip should be identified by high stress level. However, the damage zone is identified with the intrinsic microstructural damage mechanisms [15]. In ductile materials, intrinsic damage mechanisms typically involve processes which create microcracks or voids. The process include: dislocation pile-ups or interface decohesion, in the highly stressed region ahead of the tip, leading to classical failure by cleavage; intergranular cracking or microvoid coalescence; and comparable mechanisms under cyclic loading.

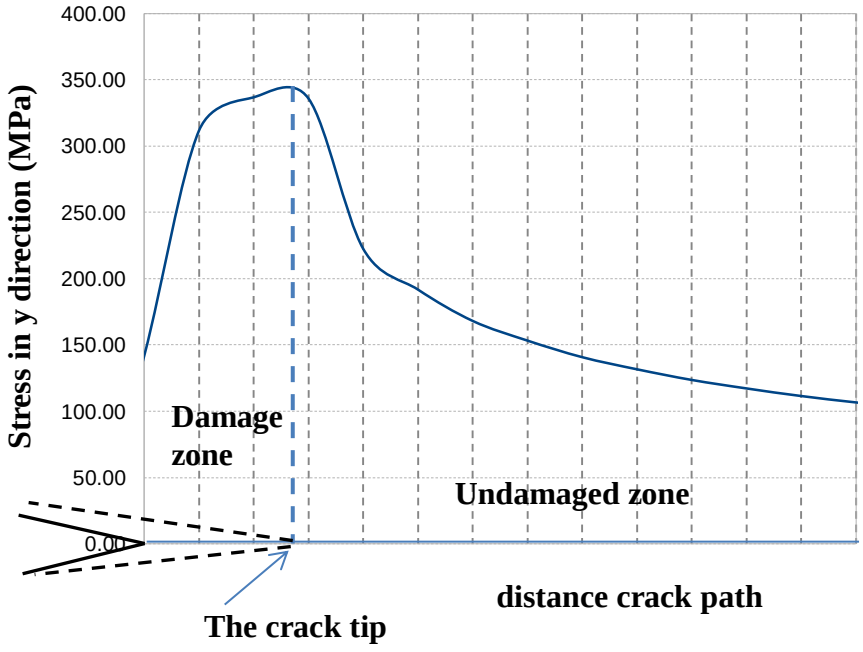

Figure 6.12 Stress distributions in elastic-plastic materials

The stress level at the crack tip is commonly affected by loading condition and crack length. In cyclic loading condition, it is interested in examining the stress level at the crack tip for different number of cycles. Since there is linear relationship between number of cycle and varying toughness, therefore the effect of variable toughness to stress distribution at ahead of crack tip is investigated in this section.

6.5. Energy Criteria in Fatigue Crack Growth

In ductile materials, during fracture process, the energy is supplied by the external applied loads. The material undergoes elastic plastic deformation involving elastic energy, plastic dissipative energy and separation energy to create new surface. Energy is supplied to damage zone in the form of cohesive energy. If the energy required to create new surface reaches a critical energy, a crack will propagate. However before crack growth, the local damage zone occurs within the cohesive zone.

Rate of change in elastic energy is defined by means of a tensor product between stress and elastic strain rate, i.e.

$$\dot{W}_e = \int_{\Omega} \underline{\underline{\sigma}} : \dot{\underline{\underline{\varepsilon}}}^e \, d\Omega \qquad (6.9)$$

where $\dot{\underline{\underline{\varepsilon}}}^e$ is the tensor with components of elastic-strain rate and $\underline{\underline{\sigma}}$ is the Cauchy stress tensor.

In ideal elastic materials, no dissipation of energy takes place and all of the stored energy is recoverable upon unloading. In contrast, plastic energy is identified with

the energy dissipated arising from plastic deformation. In elastic-plastic materials, the plastic strain is unrecoverable upon unloading condition and the dissipation rate takes the form

$$\dot{W}_{pl} = \int_{\Omega} \underline{\underline{\sigma}} : \dot{\underline{\underline{\varepsilon}}}^{pl} \, d\Omega \tag{6.8}$$

where $\dot{\underline{\underline{\varepsilon}}}^{pl}$ is the tensor whose components are rates of plastic strain and $\underline{\underline{\sigma}}$ is the Cauchy stress tensor.

In fracture mechanics, the cohesive energy is the sum of separation energies arising from dissipative processes taking place within the damage zone. The energy dissipated in this zone during the process of separation is known as the separation energy. The rate of change of separation energy is identified with a product of cohesive traction $\underline{\tau}$ and surface separation velocity $\underline{v}$ and is of the form

$$\dot{W}_{sp} = \int_{\Gamma} \underline{\tau} : \underline{v} \, d\Gamma \tag{6.9}$$

In fatigue analysis, material undergoes the accumulation of damage but also involves elastic and plastic deformation. However, the mechanism for crack propagation is by means of the accumulation of separation energy, which when equal to the cohesive energy results in crack extension. Elastic potential energy is recognised to be a state variable and hence in dependent on the current loading conditions, i.e.

$$W_e = W_e^i \tag{6.10}$$

where W_e^i is the elastic energy at the end of the i^{th} cycle.

The total plastic dissipative energy on the other hand is the accumulation of the plastic energy dissipated per cycle and takes the form

$$W_{pl} = \sum_{i=0}^{N} W_{pl}^{i} \tag{6.11}$$

where W_{pl}^{i} is the plastic energy dissipated for each cycles and N is number of cycles. Similarly, the total separation energy is likewise the accumulation of separation energy per cycle which can be written in a similar form as

$$W_{sp} = \sum_{i=0}^{n} W_{sp}^{i} \tag{6.12}$$

where W_{sp}^{i} is the separation energy for each cycle.

In a cohesive zone model, the accumulation of separation energy is one of quantities considered to examine crack growth. It is known that the number of cycles to propagate a crack is dependent on the how many cycles it takes for the accumulation of separation energy to equal the cohesive energy or toughness. Hence it immediately follows that the variable toughness will affect the number of cycles as clearly shown in Figure 6.2. It is observed that the lowest toughness has the smallest area under the curve. Since the area is reduced, the number of cycles to extend a crack is reduced accordingly.

In this section, the effect of variable toughness is investigated further to evaluate its effect on elastic and plastic energy for fatigue failure. Considered here is the amount of energy dissipated for a crack to reach a prescribed length.

6.5.1 Model Description

In this case study, the model is the same as that considered in section 6.3.1. The mechanical properties of the material are shown in Table 6.4. A constant amplitude loading (CAL) is applied with a maximum stress loading of 21.3 MPa with load ratio (R = 0) applied uniformly on the edge top of the plate as a sinusoidal function.

Table 6.4 Mechanical properties

Young's Modulus E (MPa)	**Yield Stress σ_Y (MPa)**	**Poison's ratio** ν	**Critical Cohesive Traction (fixed) σ_c (MPa)**	**Varying Toughness G_c (N/mm)**
72000	300	0.3	340	7.0,10.5,14.0 and 17.5

6.5.2 Results and Discussion

Figure 6.13 to 6.22 show the stress distribution along the crack path for various values of toughness for the incremental crack length Δa of 0.1, 0.2, 0.3, 0.4, 0.5, 0.6, 0.7, 0.8, 0.9 and 1.0 mm, respectively. It can be seen from figures that the stress distribution σ_{yy} along the crack path for same incremental crack length has similar stress levels for different toughness value.

Figure 6.23 shows the comparison of elastic energy for different value of toughness in same incremental crack length. It can be seen from figure, the amount of elastic energy is unaffected by different value of toughness. In contrast elastic energy, Figure 6.24 presents the comparison of plastic energy dissipated for varying toughness in same incremental crack length. It can be seen from figure, the amount

of plastic energy are affected by varying toughness. Since the largest toughness requires the higher number of cycles for crack growth, it is therefore expected to have the highest accumulation of plastic energy dissipated.

Figure 6.25 presents the comparison of separation energy dissipated per cycle for varying toughness in same incremental crack length. It can be seen from figure, the amount of separation energy per cycle are not affected by varying toughness for same incremental crack length. It is therefore expected to the relationship between number of cycle and varying toughness is linear as indicated in Equation (6.8).

6.6. Summary

From the case study of varying toughness, it can be concluded that the variable toughness with fixed critical cohesive traction does not significantly affect the stress levels and elastic energy. The accumulation of damage in different value of toughness shows the same stress level for every incremental crack length. There is a slight difference for the lowest toughness but in general stress level can be concluded to be similar. However there is a significant difference for plastic energy dissipated which increase with toughness. The stress levels might well change if plastic deformation is more significant involved.

Furthermore it also can be deduced that increasing toughness will increase the number of cycles for same incremental crack length. Higher toughness means a larger number of cycles to propagate the crack by the same increment of crack

length. **It has been established that the relationship between the number of cycles and toughness for different value of incremental crack length Δa is linear.**

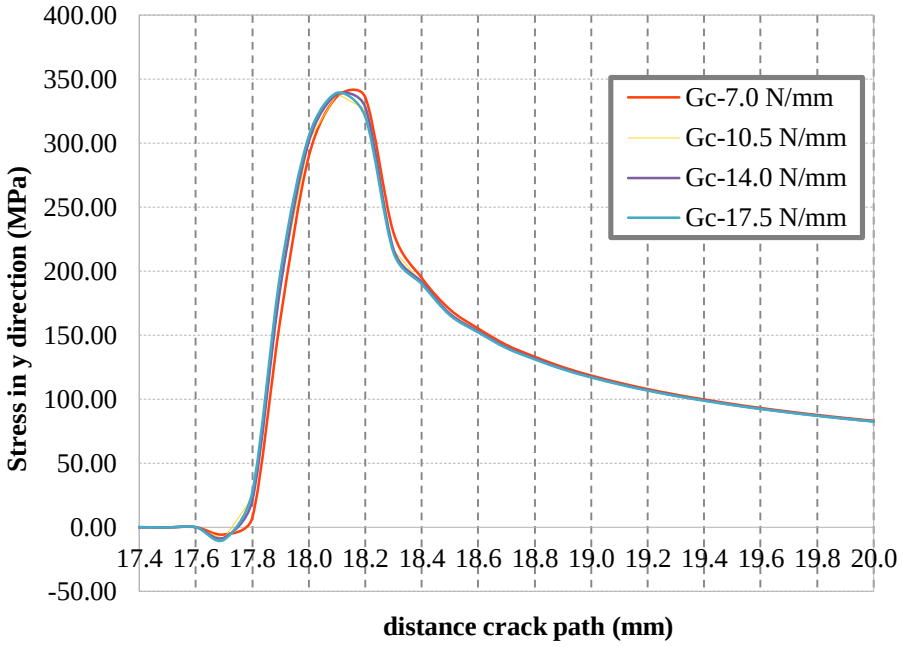

Figure 6.13 Stress distribution along crack path at da = 0.1 mm for peak loading

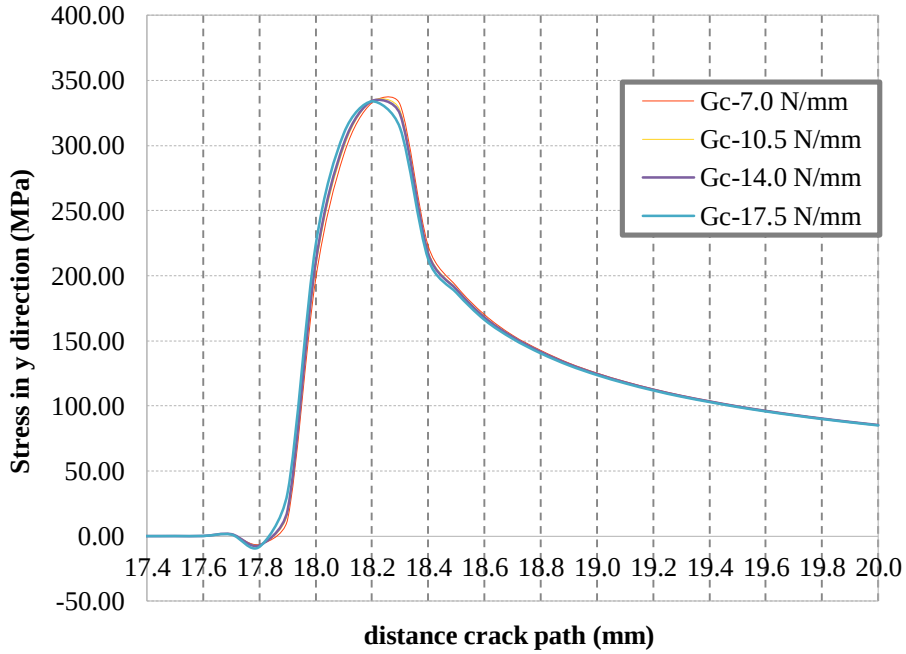

Figure 6.14 Stress distribution along crack path at da = 0.2 mm for peak loading

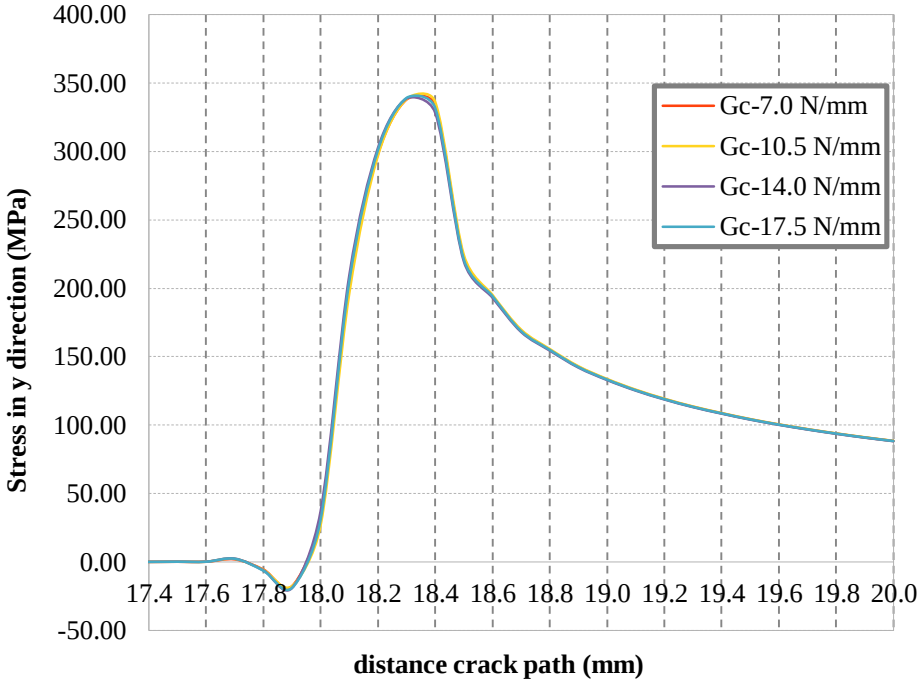

Figure 6.15 Stress distribution along crack path at da = 0.3 mm for peak loading

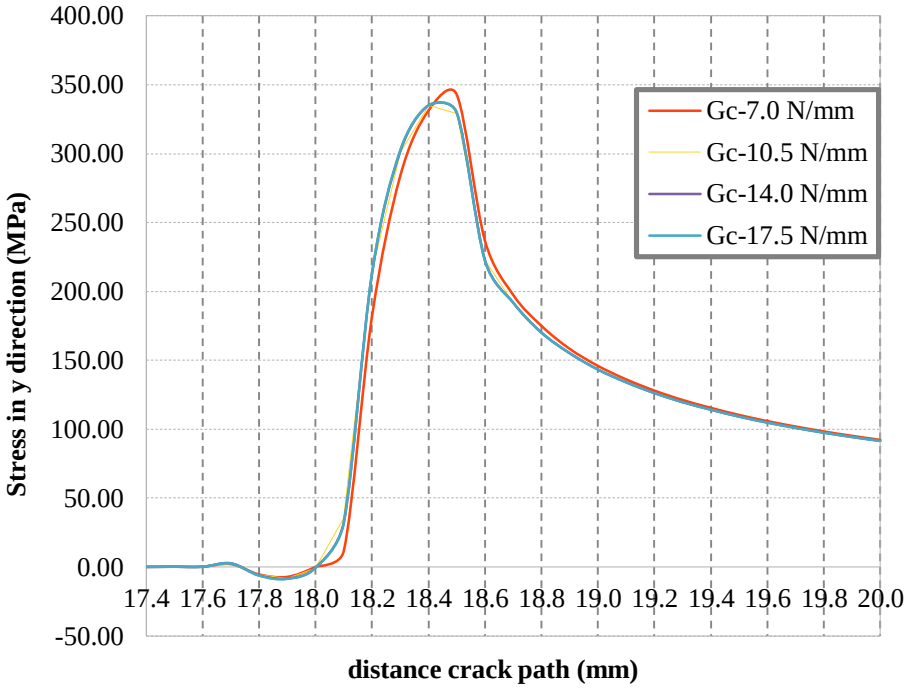

Figure 6.16 Stress distribution along crack path at da = 0.4 mm for peak loading

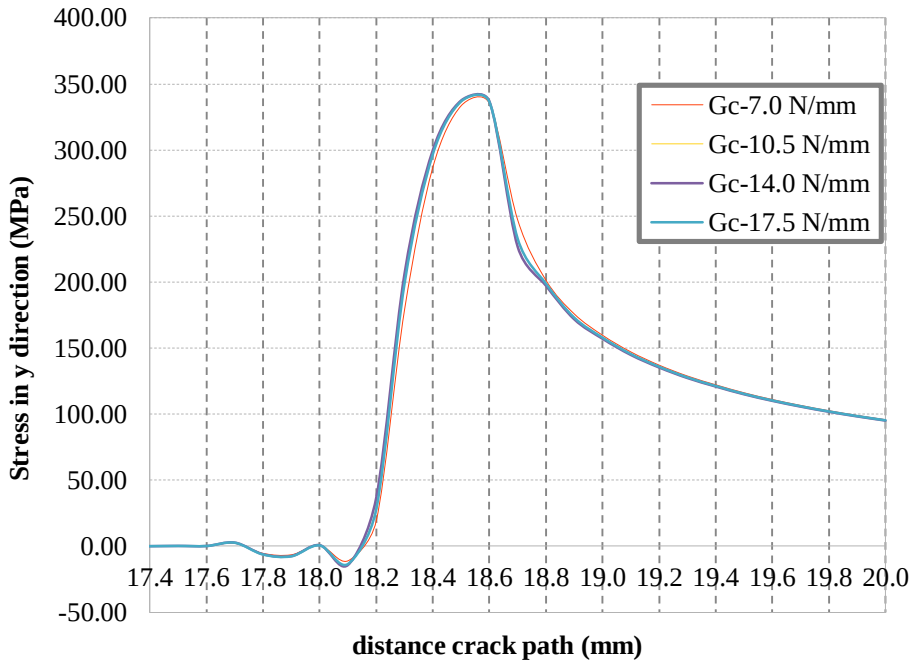

Figure 6.17 Stress distribution along crack path at da = 0.5 mm for peak loading

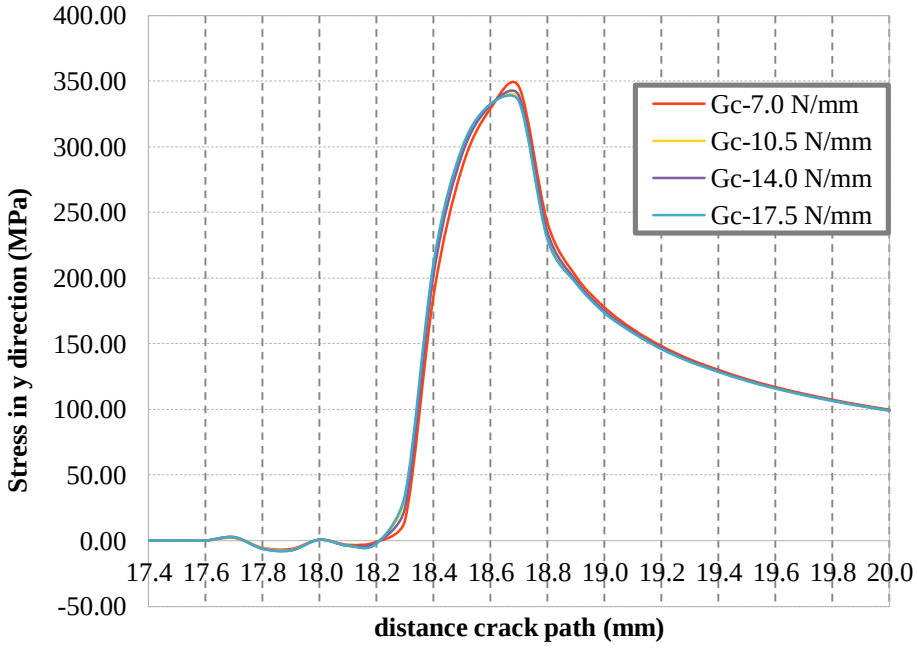

Figure 6.18 Stress distribution along crack path at da = 0.6 mm for peak loading

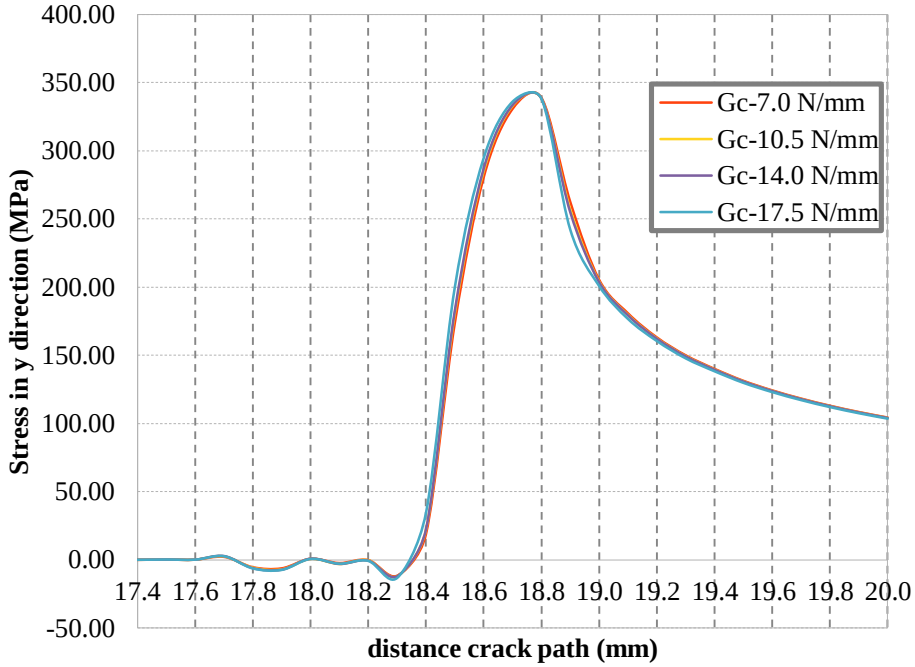

Figure 6.19 Stress distribution along crack path at da = 0.7 mm for peak loading

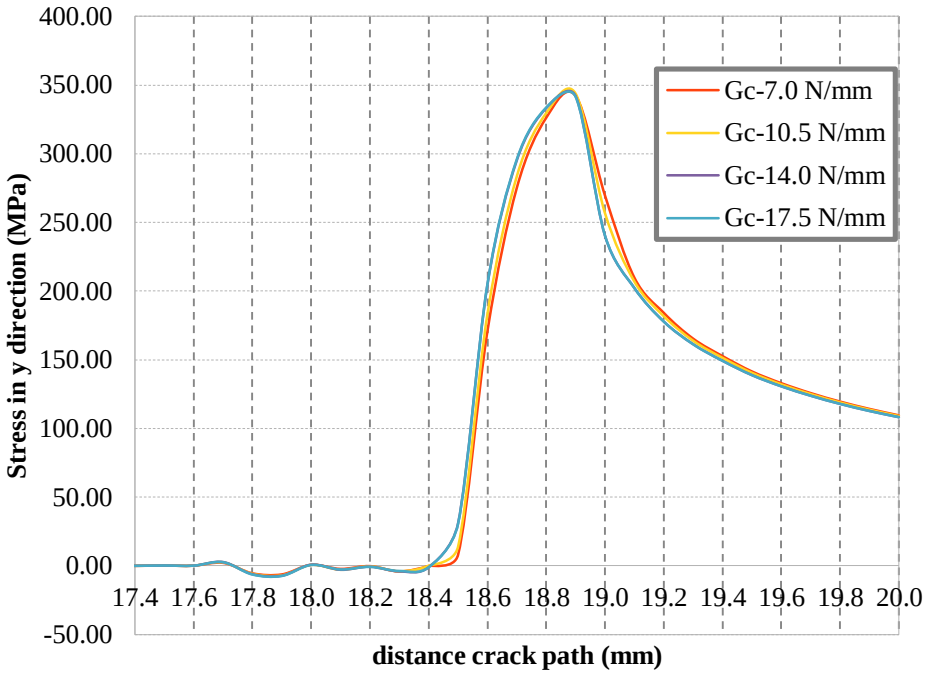

Figure 6.20 Stress distribution along crack path at da = 0.8 mm for peak loading

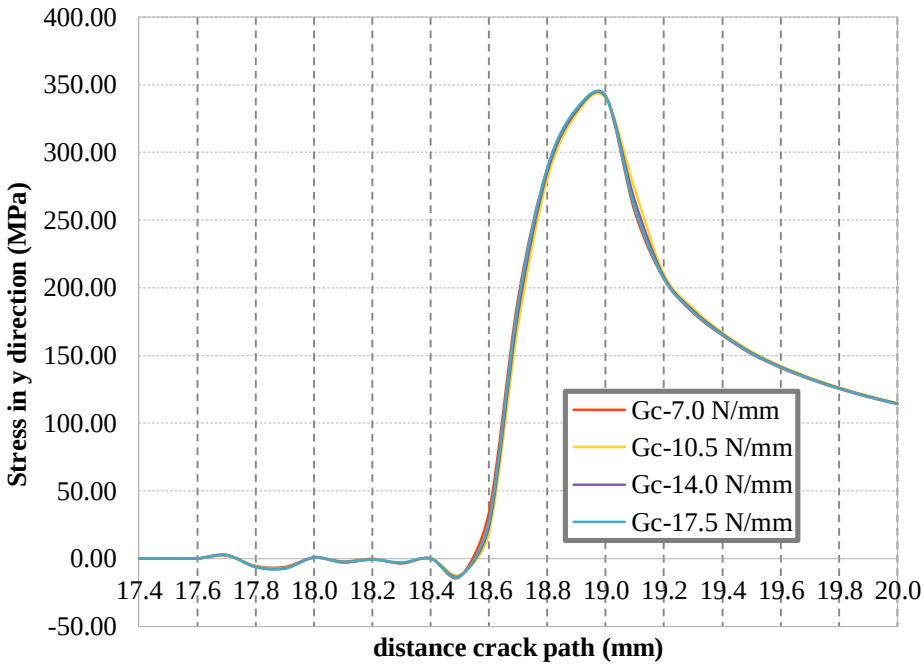

Figure 6.21 Stress distribution along crack path at da = 0.9 mm for peak loading

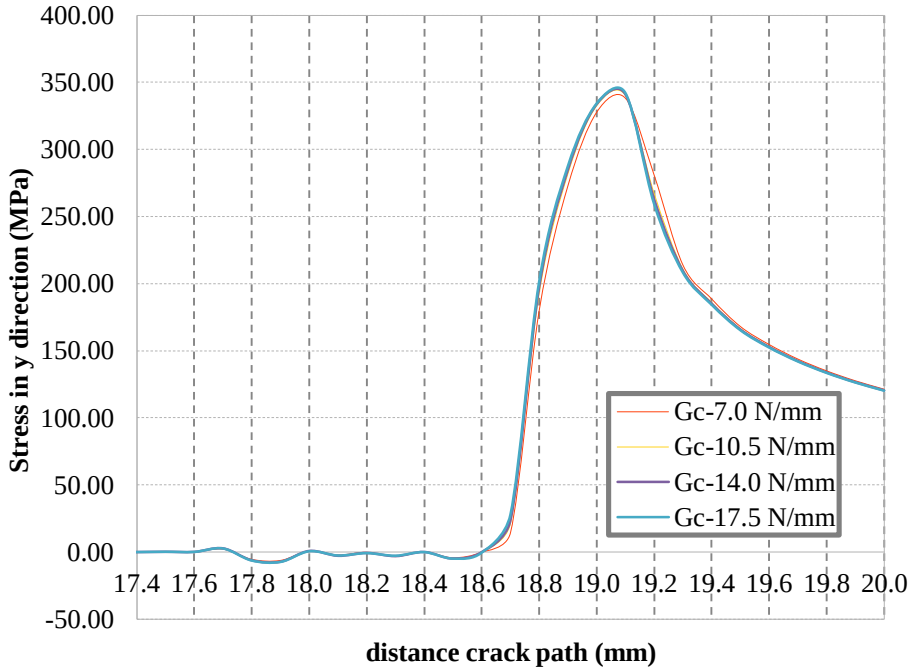

Figure 6.22 Stress distribution along crack path at da = 1.0 mm for peak loading

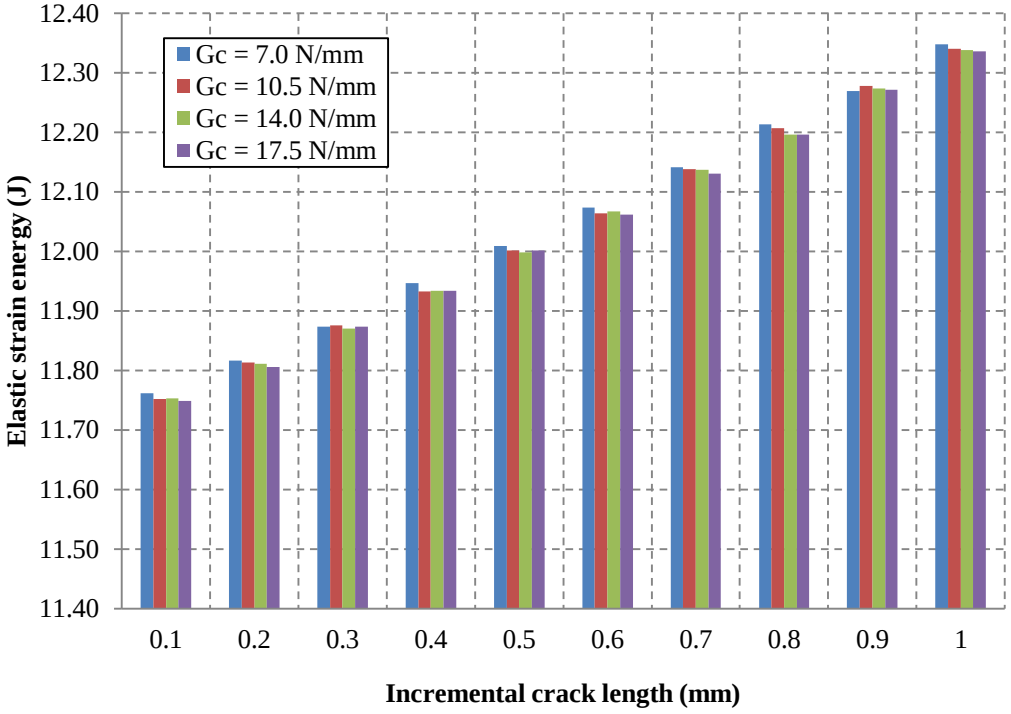

Figure 6.23 The effect of variable toughness for elastic energy

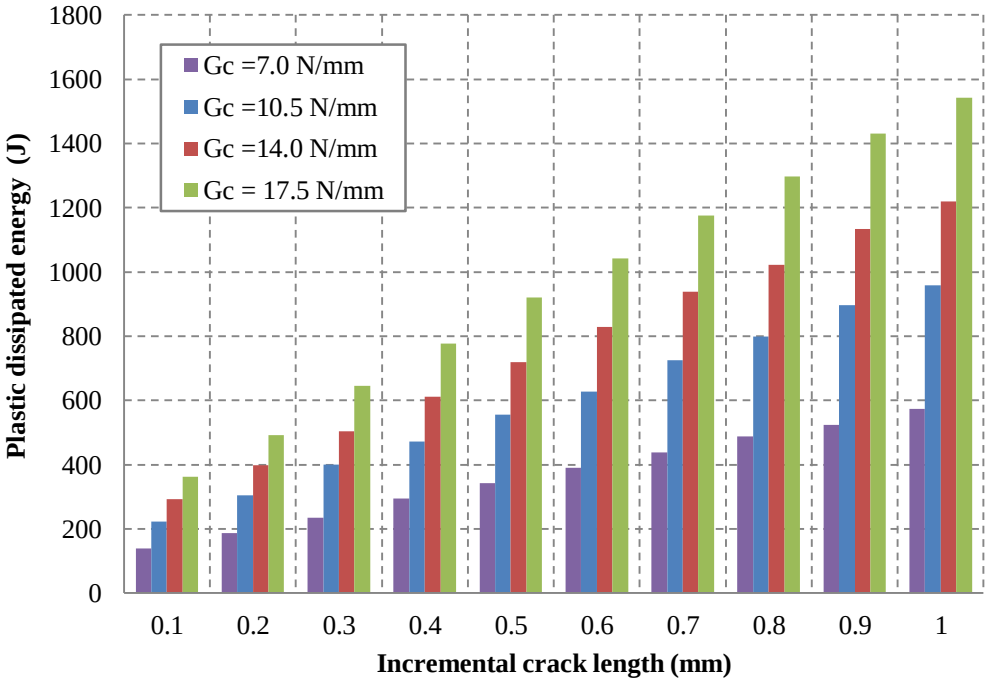

Figure 6.24 The effect of variable toughness for plastic energy

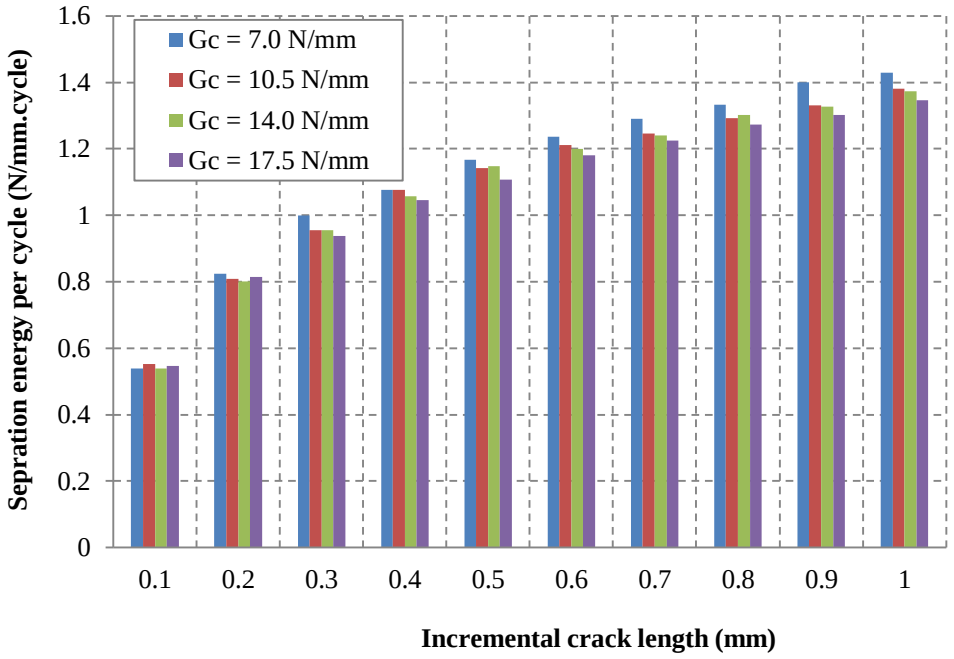

Figure 6.25 The effect of variable toughness for separation energy per cycles

Chapter 7

Fast Track Method for Fatigue Crack Growth

7.1. Introduction

Structures subject to cyclic loading are affected by the slow degradation of material ahead of a crack. This degradation can be represented indirectly in a cohesive zone model by an evolution of stiffness and critical normal traction σ_c. Various cohesive models have been proposed with some incorporating in degrading critical cohesive traction under cyclic loading and unloading [6] along with incremental changes in stiffness [82]. In this work, the degrading peak cohesive traction approach is incorporated along with the adoption of an irreversibility parameter. Care must be taken however to determine the range over which stable computation can be performed, i.e. determine the point at which damage evolution results in structural instability or critical fracture. This section introduces a method that adopts an artificial material property but unfortunately increases the risk of instability, which

might not be reflective of the real process; clearly this should be avoided. Reducing the fracture toughness has the effect of reducing the number of cycles to failure but also could result in fast fracture which is somewhat undesirable. Provided fast fracture can be avoided artificially reduced fracture toughness can result in the whole load computation history being reduced to selected numbers of cycles.

In this chapter, new methodology called the fast-track method is developed as an alternative approach to predict fatigue crack growth. This method is based on modifying toughness value in a cohesive zone model and the existence of a functional relationship between the number of cycles and variable artificial toughness. The linear relationship between variable toughness and the number of cycles established in Chapter 6 is introduced. In this present study, the fast-track method is applied to simulate fatigue crack growth due to the constant amplitude loading and single overloading. The results of the fast-track method are compared with numerical results from finite element method.

To implement a fast-track solution methodology, there are some issues that need to be considered, i.e.

1. To invoke the effect of plasticity on increased resistance, the choice of critical cohesive traction σ_c should be a higher value than the yield stress. Consequently a variation in fracture toughness with a fixed critical cohesive traction is achieved by a variation in critical normal separation δ_c in the traction separation law as shown in Figure 6.2 in Chapter 6.

2. Fast tracking is necessarily limited to stable fatigue crack growth propagates for every given toughness. In this condition, the choice of smallest toughness should be considered which based on the load stability of structure containing a certain crack length. The stability of which can be assessed by using the failure assessment diagram (FAD).
3. Curve fitting is used to establish a relationship between artificial toughness and the number of cycles to failure.

7.2. Failure Assessment Diagram

The failure assessment diagram (FAD) is provided to predict the instability loads of a structure containing crack. The diagram is based on a safety or failure plane defined by the ratio between stress intensity factor and fracture toughness K_r as the ordinate and the applied load or plastic collapse load ratio L_r as the abscissa shown in Figure 7.1. The plastic collapse load is defined as the applied load causing plastic collapse of the cracked geometry in a model made from elastic perfectly-plastic material. If the assessment point lies inside the failure assessment curve, the crack growth can occur in stable manner, otherwise the assessment point lies outside the curve, and then unstable crack growth is likely to occur.

The common FAD is presented [85] as

$$K_r = \left(1 - 0.14L_r^2\right)\left[0.3 + 0.7\exp\left(-0.65L_r^6\right)\right] \tag{7.1}$$

where $K_r = \frac{K_I}{K_{IC}}$ and $L_r = \frac{P_a}{P_c}$ (7.2)

K_I and K_{IC} are the stress intensity factor for current crack length and the fracture toughness, respectively. P_a and P_c are denoted as the applied load and maximum plastic load, respectively.

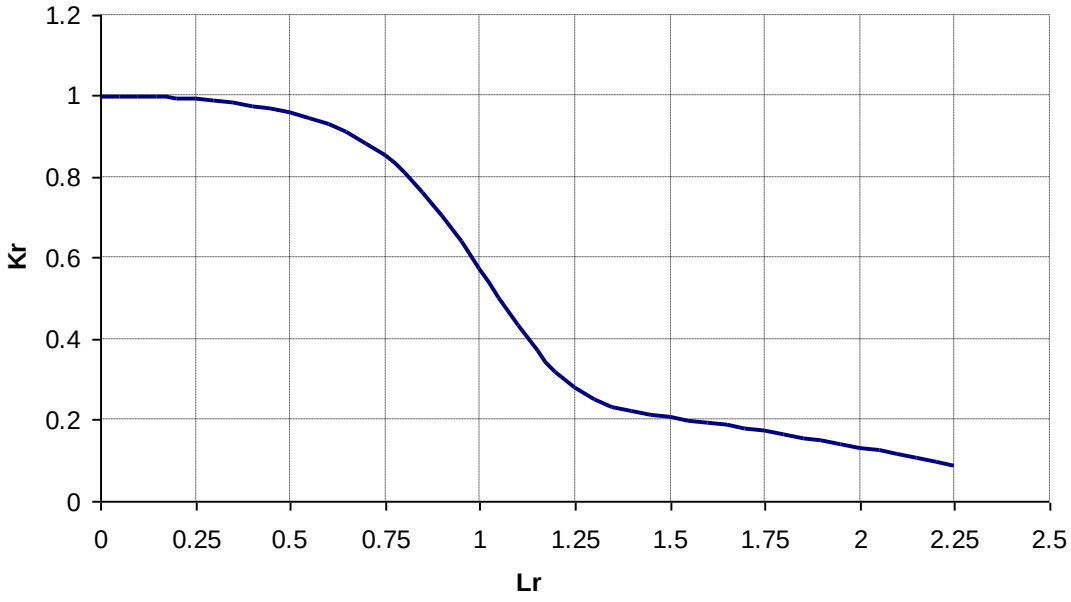

Figure 7.1 Failure Assessment Diagram (FAD)

7.3. Method of Least Squares

Method of Least Squares is a procedure to determine the best fit line to data. In this present study, the basic problem is to define the best fit straight line $y = ax + b$ for given data. Consider data $\{(x_1, y_1), \ldots, (x_n, y_n)\}$ to be known, the error which associated with straight line $y = ax + b$, is defined as

$$E(a,b) = \sum_{i=1}^{n} (y_i - (ax_i + b))^2 \qquad (7.3)$$

The objective is to find values of a and b with minimize the error. The condition for $E(a,b)$ to be minimum will be expresses as

$$\frac{\delta E}{\delta a} = -2\sum_{i=1}^{n} x_i\left(y_i - (ax_i + b)\right) = 0 \tag{7.4}$$

$$\frac{\delta E}{\delta b} = -2\sum_{i=1}^{n} \left(y_i - (ax_i + b)\right) = 0 \tag{7.5}$$

Equation (7.4) and (7.5) can be rewritten as

$$a\sum_{i=1}^{n} x_i^2 + b\sum_{i=1}^{n} x_i = \sum_{i=1}^{n} x_i y_i \tag{7.6}$$

$$a\sum_{i=1}^{n} x_i + nb = \sum_{i=1}^{n} y_i \tag{7.7}$$

Equation (7.6) multiplied by n and equation (7.7) multiplied by $\sum_{i=1}^{n} x_i$ lead to

$$na\sum_{i=1}^{n} x_i^2 + nb\sum_{i=1}^{n} x_i = n\sum_{i=1}^{n} x_i y \tag{7.8}$$

$$a\left(\sum_{i=1}^{n} x_i\right)^2 + nb\sum_{i=1}^{n} x_i = \sum_{i=1}^{n} y_i \sum_{i=1}^{n} x_i \tag{7.9}$$

By solving both equation, the values of a and b are

$$a = \frac{n\sum_{i=1}^{n} x_i y_i - \sum_{i=1}^{n} x_i \sum_{i=1}^{n} y_i}{n\sum_{i=1}^{n} x_i^2 - \left(\sum_{i=1}^{n} x_i\right)^2} \tag{7.10}$$

$$b = \frac{\sum_{i=1}^{n} y_i \sum_{i=1}^{n} x_i^2 - \sum_{i=1}^{n} x_i \sum_{i=1}^{n} x_i y_i}{n\sum_{i=1}^{n} x_i^2 - \left(\sum_{i=1}^{n} x_i\right)^2} \tag{7.11}$$

.

7.4. The Number of Cycles Estimation Strategy

Consider the data $\{(G_1, N_1), \ldots, (G_n, N_n)\}$ to be known, where G_i is the varying toughness and N_i is the number of cycles to propagate a crack to presented length. To predict the number of cycle N_{n+1} with associated with G_{n+1}, the power law from Paris's equation modified is applied, i.e.

$$\frac{dN}{dG} = mG^c \tag{7.12}$$

With the application of natural logarithms, the values of m and c can be obtained although the relationship between toughness and number of cyclic transpires to be essentially linear and thus the value of c = 0 give

$$\frac{dN}{dG} = m \tag{7.13}$$

Application of a best fit straight line $y = ax + b$ to data set with a Least Square measure provides the gradient of best fit straight line given by $\frac{dy}{dx} = a = m$, with the value of m equal to

$$m = a = \frac{n\sum_{i=1}^{n} x_i y_i - \sum_{i=1}^{n} x_i \sum_{i=1}^{n} y_i}{n\sum_{i=1}^{n} x_i^2 - \left(\sum_{i=1}^{n} x_i\right)^2} = \frac{n\sum_{i=1}^{n} G_i N_i - \sum_{i=1}^{n} G_i \sum_{i=1}^{n} N_i}{n\sum_{i=1}^{n} G_i^2 - \left(\sum_{i=1}^{n} G_i\right)^2} \tag{7.14}$$

The next number of cycles N_{n+1} can be predicted by using

$$\int_{N_n}^{N_{n+1}} dN = m \int_{G_n}^{G_{n+1}} dG \tag{7.15}$$

By solving Equation. (7.15), the number of cycle N_{n+1} can be predicted by using

$$N_{n+1} = N_n + m[G_{n+1} - G_n] \tag{7.16}$$

where N_n is the last number of cycle in set of data, G_n is the last toughness in set of data and G_{n+1} is the toughness for the predicted number of cycle N_{n+1}.

7.5. Model Description

In this analysis, the model is the same as that considered in section 6.3.1. A constant amplitude loading (CAL) is considered with a maximum stress loading of 21.3 MPa (load ratio R = 0) applied uniformly on the edge top of plate as a sinusoidal function as shown in Figure 7.2(a). For overloading case study, a single overloading (S_{ol}) of 27.3 MPa is applied at the first cycle and then followed by loads (S_{max}) of 21.3 MPa is applied uniformly on the top edge of the plate as a sinusoidal function as shown in Figure 7.2(b). A load ratio $R = S_{min} / S_{max} = 0$ is applied as shown in Figure 7.2. The mechanical properties are tabulated in Table 7.1.

Table 7.1 Mechanical properties

Young's Modulus E (MPa)	**Yield Stress σ_{ys} (MPa)**	**Poison's ratio ν**	**Critical Cohesive Traction σ_c (MPa)**	**Toughness G_c (N/mm)**
72000	300	0.3	340	124.3

7.5.1 Estimation of the Smallest Toughness

The smallest toughness should be defined first to obtain the given load is in a stable condition for plate containing crack as shown in Figure 7.3. In the constant amplitude loading (CAL) study, the cracked plate subjected to the maximum uniform stress of 21.3 MPa.

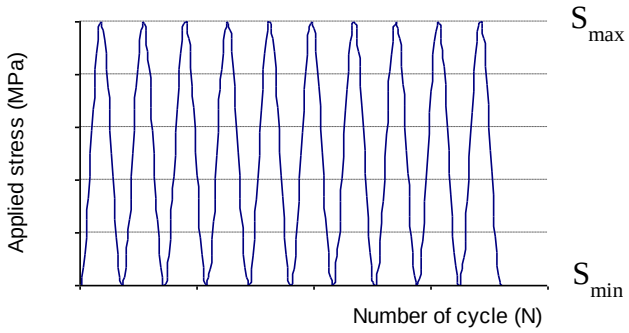

(a) constant amplitude loading

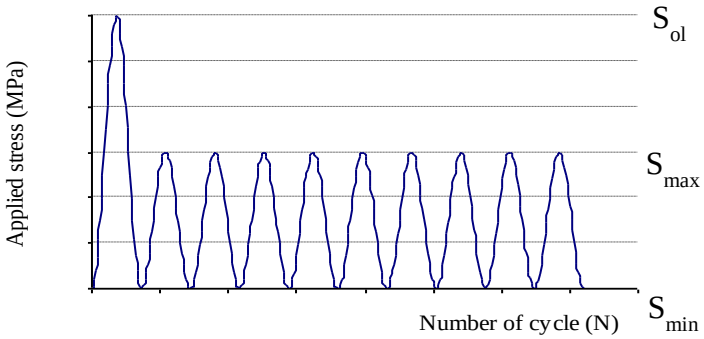

(b)) single overloading

Figure 7.2 The schematic of applied loading

The parameter of L_r can be calculated as

$$L_r = \frac{P_a}{P_c} = \frac{\sigma_o w}{\sigma_Y (w-a)} = \frac{21.3 \times 52}{300 \times (52-17.7)} = 0.11$$

The parameter of K_r can be obtained

$$K_r = \left(1-0.14(0.11)^2\right)\left[0.3+0.7\exp\left(-0.65(0.11)^6\right)\right]$$
$$= 0.9984$$

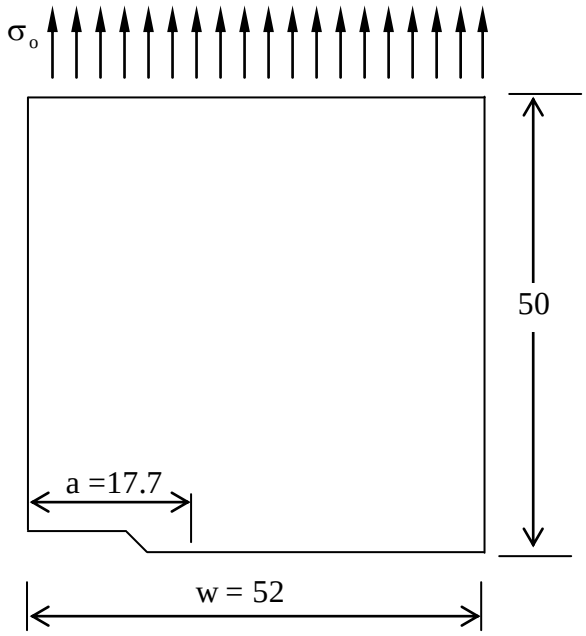

Figure 7.3 The cracked plate subjected to uniform stress

The smallest fracture toughness can be calculated by using the equation

$$K_{IC} = \frac{K_I}{K_r} = \frac{\sigma_o Y\sqrt{a}}{K_r}$$

where Y is a dimensionless geometric of parameter which defined [60] as following form

$$\begin{aligned} Y &= 1.99 - 0.41\cdot\frac{a}{W} + 18.7\left(\frac{a}{W}\right)^2 - 38.48\left(\frac{a}{W}\right)^3 + 53.85\left(\frac{a}{W}\right)^4 \\ &= 1.99 - 0.41\cdot\frac{17.7}{52} + 18.7\left(\frac{17.7}{52}\right)^2 - 38.48\left(\frac{17.7}{52}\right)^3 + 53.85\left(\frac{17.7}{52}\right)^4 \\ &= 3.2224 \end{aligned}$$

Therefore,

$$K_{IC} = \frac{21.3\times 3.2224\sqrt{17.7}}{0.9984} = 289.23\ \text{MPa}\sqrt{\text{mm}}$$

The relationship between a critical stress intensity factor (fracture toughness) K_{IC} and a critical energy release rate G_{IC} can be expressed as

$$G_{IC} = \frac{K_{IC}^2}{E} = \frac{289.23^2}{72000} = 1.16 \text{ N/mm}$$

In the constant amplitude loading, the smallest toughness chosen is $G_{IC} = 3.5 \text{ N/mm}$.

In the single overloading (SOL) study, the cracked plate subjected to the maximum uniform stress of 27.3 MPa. The parameter of L_r can be calculated as

$$L_r = \frac{P_a}{P_c} = \frac{\sigma_o w}{\sigma_Y (w-a)} = \frac{27.3 \times 52}{300 \times (52-17.7)} = 0.1379$$

The parameter of K_r can be obtained

$$\begin{aligned} K_r &= \left(1 - 0.14(0.1379)^2\right)\left[0.3 + 0.7\exp\left(-0.65(0.1379)^6\right)\right] \\ &= 0.9973 \end{aligned}$$

The fracture toughness is

$$K_{IC} = \frac{27.3 \times 3.2224\sqrt{17.7}}{0.9973} = 371.0892 \text{ MPa}\sqrt{\text{mm}}$$

The relationship between a critical stress intensity factor (fracture toughness) K_{IC} and a critical energy release rate G_{IC} can be expressed as

$$G_{IC} = \frac{K_{IC}^2}{E} = \frac{371.0892^2}{72000} = 1.92 \text{ N/mm}$$

In the constant amplitude loading, the smallest toughness chosen is $G_{IC} = 5.9 \text{ N/mm}$.

In the constant amplitude loading study, a fast-track method (FTM) is implemented to find the effect of relatively large change in artificial toughness applied along with various number of data points as illustrated in Table 7.2. The number of cycle results from numerical calculation for difference toughness with data range ΔG = 3.5 N/mm in incremental crack length is provided in Table 7.3. Furthermore, for the number of cycle results from numerical calculation for seven difference toughness (n = 7) with data range ΔG = 0.5 N/mm in incremental crack length and completely calculation using the Fast-Track Method (FTM) can be seen shown in Table 7.15.

Table 7.2 Set up data for varying toughness

Data (n)	**Toughness (N/mm)**						
	Interval data (ΔG = 3.5)						
2	3.5	7.0					
3	3.5	7.0	10.5				
4	3.5	7.0	10.5	14.0			
5	3.5	7.0	10.5	14.0	17.5		
6	3.5	7.0	10.5	14.0	17.5	21.0	
	Interval data (ΔG = 0.5)						
7	3.5	4.0	4.5	5.0	5.5	6.0	6.5

Table 7.3 Number of cycle data for difference toughness in incremental crack length

		Variable toughness (N/mm)					
Incremental crack length (mm)	**Δa**	**3.5**	**7**	**10.5**	**14**	**17.5**	**21**
	0.1	6	13	19	26	32	38
	0.2	8	17	26	35	43	52
	0.3	10	21	33	44	56	67
	0.4	12	26	39	53	67	81
	0.5	14	30	46	62	79	95
	0.6	15	34	52	71	89	108
	0.7	17	38	59	80	100	121
	0.8	19	42	65	87	110	133
	0.9	20	45	71	96	121	146
	1.0	22	49	76	103	130	157

From data in Table 7.3 for every incremental crack length (Δa), the number of cycle (N) and toughness G (N/mm) will be rearranged as shown in Table 7.4.

Table 7.4 Number of cycle data versus six difference toughness (n = 6) for every incremental crack length

Incremental crack length (mm)	Δa	Cycles (N)	G (N/mm)
	0.1	6	3.5
		13	7.0
		19	10.5
		26	14.0
		32	17.5
		38	21.0
	0.2	8	3.5
		17	7.0
		26	10.5
		35	14.0
		43	17.5
		52	21.0
	0.3	10	3.5
		21	7.0
		33	10.5
		44	14.0
		56	17.5
		67	21.0
	0.4	12	3.5
		26	7.0
		39	10.5
		53	14.0
		67	17.5
		81	21.0
	0.5	14	3.5
		30	7.0
		46	10.5
		62	14.0
		79	17.5
		95	21.0

Incremental crack length	Δa	Cycles (N)	G (N/mm)
	0.6	15	3.5
		34	7.0
		52	10.5
		71	14.0
		89	17.5
		108	21.0
	0.7	17	3.5
		38	7.0
		59	10.5
		80	14.0
		100	17.5
		121	21.0
	0.8	19	3.5
		42	7.0
		65	10.5
		87	14.0
		110	17.5
		133	21.0
	0.9	20	3.5
		45	7.0
		71	10.5
		96	14.0
		121	17.5
		146	21.0
	1.0	22	3.5
		49	7.0
		76	10.5
		103	14.0
		130	17.5
		157	21.0

By using Equation (7.14), for incremental crack length (Δa) of 0.1 mm and n = 2, the gradient m can be defined as

$$m = \frac{n\sum_{i=1}^{n} G_i N_i - \sum_{i=1}^{n} G_i \sum_{i=1}^{n} N_i}{n\sum_{i=1}^{n} G_i^2 - \left(\sum_{i=1}^{n} G_i\right)^2} = \frac{2\times 112 - 10.5\times 19}{2\times 61.250 - 110.250} = 2.000$$

All results and calculations for every incremental crack length (da) and n =2, 3, 4, 5 and 6 can be shown from Table 7.5 to 7.9, respectively.

Table 7.5 The gradient m for two different toughness (n = 2)

Incremental crack length (mm)	Δa	$\sum_{i=1}^{n} N_i$	$\sum_{i=1}^{n} G_i$	$\sum_{i=1}^{n} N_i G_i$	$\sum_{i=1}^{n} G_i^2$	$\left(\sum_{i=1}^{n} G_i\right)^2$	m
	0.1	19	10.5	112	61.250	110.250	2.000
	0.2	25	10.5	147	61.250	110.250	2.571
	0.3	31	10.5	182	61.250	110.250	3.143
	0.4	38	10.5	224	61.250	110.250	4.000
	0.5	44	10.5	259	61.250	110.250	4.571
	0.6	49	10.5	290.5	61.250	110.250	5.429
	0.7	55	10.5	325.5	61.250	110.250	6.000
	0.8	61	10.5	360.5	61.250	110.250	6.571
	0.9	65	10.5	385	61.250	110.250	7.143
	1.0	71	10.5	420	61.250	110.250	7.714

Table 7.6 The gradient m for three different toughness (n = 3)

Incremental crack length (mm)	Δa	$\sum_{i=1}^{n} N_i$	$\sum_{i=1}^{n} G_i$	$\sum_{i=1}^{n} N_i G_i$	$\sum_{i=1}^{n} G_i^2$	$\left(\sum_{i=1}^{n} G_i\right)^2$	m
	0.1	38	21	311.5	171.500	441.000	1.857
	0.2	51	21	420	171.500	441.000	2.571
	0.3	64	21	528.5	171.500	441.000	3.286
	0.4	77	21	633.5	171.500	441.000	3.857
	0.5	90	21	742	171.500	441.000	4.571
	0.6	101	21	836.5	171.500	441.000	5.286
	0.7	114	21	945	171.500	441.000	6.000
	0.8	126	21	1043	171.500	441.000	6.571
	0.9	136	21	1130.5	171.500	441.000	7.286
	1.0	147	21	1218	171.500	441.000	7.714

Table 7.7 The gradient m for four different toughness (n = 4)

Incremental crack length (mm)	Δa	$\sum_{i=1}^{n} N_i$	$\sum_{i=1}^{n} G_i$	$\sum_{i=1}^{n} N_i G_i$	$\sum_{i=1}^{n} G_i^2$	$\left(\sum_{i=1}^{n} G_i\right)^2$	m
	0.1	64	35	675.500	367.500	1225.000	1.886
	0.2	86	35	910.000	367.500	1225.000	2.571
	0.3	108	35	1144.500	367.500	1225.000	3.257
	0.4	130	35	1375.500	367.500	1225.000	3.886
	0.5	152	35	1610.000	367.500	1225.000	4.571
	0.6	172	35	1830.500	367.500	1225.000	5.314
	0.7	194	35	2065.000	367.500	1225.000	6.000
	0.8	213	35	2261.000	367.500	1225.000	6.486
	0.9	232	35	2474.500	367.500	1225.000	7.257
	1.0	250	35	2660.000	367.500	1225.000	7.714

Table 7.8 The gradient m for five different toughness (n = 5)

Incremental crack length (mm)	Δa	$\sum_{i=1}^{n} N_i$	$\sum_{i=1}^{n} G_i$	$\sum_{i=1}^{n} N_i G_i$	$\sum_{i=1}^{n} G_i^2$	$\left(\sum_{i=1}^{n} G_i\right)^2$	m
	0.1	96	52.5	1235.500	673.750	2756.250	1.857
	0.2	129	52.5	1662.500	673.750	2756.250	2.514
	0.3	164	52.5	2124.500	673.750	2756.250	3.286
	0.4	197	52.5	2548.000	673.750	2756.250	3.914
	0.5	231	52.5	2992.500	673.750	2756.250	4.629
	0.6	261	52.5	3388.000	673.750	2756.250	5.286
	0.7	294	52.5	3815.000	673.750	2756.250	5.943
	0.8	323	52.5	4186.000	673.750	2756.250	6.486
	0.9	353	52.5	4592.000	673.750	2756.250	7.229
	1.0	380	52.5	4935.000	673.750	2756.250	7.714

Table 7.9 The gradient m for six different toughness (n = 6)

Incremental crack length (mm)	Δa	$\sum_{i=1}^{n} N_i$	$\sum_{i=1}^{n} G_i$	$\sum_{i=1}^{n} N_i G_i$	$\sum_{i=1}^{n} G_i^2$	$\left(\sum_{i=1}^{n} G_i\right)^2$	m
	0.1	134	73.5	2033.500	1114.750	5402.250	1.829
	0.2	181	73.5	2754.500	1114.750	5402.250	2.506
	0.3	231	73.5	3531.500	1114.750	5402.250	3.273
	0.4	278	73.5	4249.000	1114.750	5402.250	3.935
	0.5	326	73.5	4987.500	1114.750	5402.250	4.637
	0.6	369	73.5	5656.000	1114.750	5402.250	5.298
	0.7	415	73.5	6356.000	1114.750	5402.250	5.935
	0.8	456	73.5	6979.000	1114.750	5402.250	6.498
	0.9	499	73.5	7658.000	1114.750	5402.250	7.208
	1.0	537	73.5	8232.000	1114.750	5402.250	7.714

By using the gradient m results from Table 7.5 for incremental crack length (Δa) of 0.1 mm and n = 2, the next number of cycle can be predicted by using Equation (7.16) i.e.

$$\begin{aligned} N_{n+1} &= N_n + m[G_{n+1} - G_n] \\ &= 13 + 2.0[124.3 - 7] \\ &= 248 \end{aligned}$$

The complete results and calculations of predicted number of cycles N_{n+1} for every incremental crack length (Δa) can be shown in Table 7.10 to 7.14 for data number of 2, 3, 4, 5 and 6, respectively.

Table 7.10 Predicted number of cycles N_{n+1} for two different toughness (n = 2)

Incremental crack length (mm)	Δa	m	G_n	G_{n+1}	N_n	N_{n+1}
	0.1	2.000	7	124.3	13	248
	0.2	2.571	7	124.3	17	319
	0.3	3.143	7	124.3	21	390
	0.4	4.000	7	124.3	26	495
	0.5	4.571	7	124.3	30	566
	0.6	5.429	7	124.3	34	671
	0.7	6.000	7	124.3	38	742
	0.8	6.571	7	124.3	42	813
	0.9	7.143	7	124.3	45	883
	1.0	7.714	7	124.3	49	954

Table 7.11 Predicted number of cycles N_{n+1} for three different toughness (n = 3)

Incremental crack length (mm)	Δa	m	G_i	G_{i+1}	N_i	N_{i+1}
	0.1	1.857	10.500	124.300	19	230
	0.2	2.571	10.500	124.300	26	319
	0.3	3.286	10.500	124.300	33	407
	0.4	3.857	10.500	124.300	39	478
	0.5	4.571	10.500	124.300	46	566
	0.6	5.286	10.500	124.300	52	654
	0.7	6.000	10.500	124.300	59	742
	0.8	6.571	10.500	124.300	65	813
	0.9	7.286	10.500	124.300	71	900
	1.0	7.714	10.500	124.300	76	954

Table 7.12 Predicted number of cycles N_{n+1} for four different toughness (n = 4)

Incremental crack length (mm)	Δa	m	G_i	G_{i+1}	N_i	N_{i+1}
	0.1	1.886	14.000	124.300	26	234
	0.2	2.571	14.000	124.300	35	319
	0.3	3.257	14.000	124.300	44	403
	0.4	3.886	14.000	124.300	53	482
	0.5	4.571	14.000	124.300	62	566
	0.6	5.314	14.000	124.300	71	657
	0.7	6.000	14.000	124.300	80	742
	0.8	6.486	14.000	124.300	87	802
	0.9	7.257	14.000	124.300	96	896
	1.0	7.714	14.000	124.300	103	954

Table 7.13 Predicted number of cycles N_{n+1} for five different toughness (n = 5)

Incremental crack length (mm)	Δa	m	G_i	G_{i+1}	N_i	N_{i+1}
	0.1	1.857	17.500	124.300	32	230
	0.2	2.514	17.500	124.300	43	312
	0.3	3.286	17.500	124.300	56	407
	0.4	3.914	17.500	124.300	67	485
	0.5	4.629	17.500	124.300	79	573
	0.6	5.286	17.500	124.300	89	654
	0.7	5.943	17.500	124.300	100	735
	0.8	6.486	17.500	124.300	110	803
	0.9	7.229	17.500	124.300	121	893
	1.0	7.714	17.500	124.300	130	954

Table 7.14 Predicted number of cycles N_{n+1} for six different toughness (n = 6)

Incremental crack length (mm)	Δa	m	G_i	G_{i+1}	N_i	N_{i+1}
	0.1	1.829	21.000	124.300	38	227
	0.2	2.506	21.000	124.300	52	311
	0.3	3.273	21.000	124.300	67	405
	0.4	3.935	21.000	124.300	81	487
	0.5	4.637	21.000	124.300	95	574
	0.6	5.298	21.000	124.300	108	655
	0.7	5.935	21.000	124.300	121	734
	0.8	6.498	21.000	124.300	133	804
	0.9	7.208	21.000	124.300	146	891
	1.0	7.714	21.000	124.300	157	954

Table 7.15 Number of cycle data for seven different toughness (n = 7) and ΔG = 0.5 N/mm in incremental crack length

		Toughness (N/mm)						
Incremental crack length (mm)	Δa	3.5	4.0	4.5	5.0	5.5	6.0	6.5
	0.1	6	7	8	9	10	11	12
	0.2	8	9	10	12	13	14	15
	0.3	10	12	13	15	17	18	20
	0.4	12	14	16	18	20	22	24
	0.5	14	16	18	21	23	25	28
	0.6	15	18	21	23	26	29	31
	0.7	17	20	23	26	29	32	35
	0.8	19	22	25	29	32	35	38
	0.9	20	24	27	31	35	38	42
	1.0	22	26	30	33	37	41	45

From data in Table 7.15 for every incremental crack length (Δa), the number of cycle (N) and toughness G (N/mm) will be rearranged as shown in Table 7.16.

Table 7.16 Number of cycle data versus six difference toughness (n = 7) for every incremental crack length

	Δa	Cycles (N)	G (N/mm)
Incremental crack length (mm)	0.1	6	3.5
		7	4.0
		8	4.5
		9	5.0
		10	5.5
		11	6.0
		12	6.5
	0.2	8	3.5
		9	4.0
		10	4.5
		12	5.0
		13	5.5
		14	6.0
		15	6.5
	0.3	10	3.5
		12	4.0
		13	4.5
		15	5.0
		17	5.5
		18	6.0

	Δa	Cycles (N)	G (N/mm)
Incremental crack length (mm)	0.6	15	3.5
		18	4.0
		21	4.5
		23	5.0
		26	5.5
		29	6.0
		31	6.5
	0.7	17	3.5
		20	4.0
		23	4.5
		26	5.0
		29	5.5
		32	6.0
		35	6.5
	0.8	19	3.5
		22	4.0
		25	4.5
		29	5.0
		32	5.5
		35	6.0

		20	6.5
	0.4	12	3.5
		14	4.0
		16	4.5
		18	5.0
		20	5.5
		22	6.0
		24	6.5
	0.5	14	3.5
		16	4.0
		18	4.5
		21	5.0
		23	5.5
		25	6.0
		28	6.5

		38	6.5
	0.9	20	3.5
		24	4.0
		27	4.5
		31	5.0
		35	5.5
		38	6.0
		42	6.5
	1.0	22	3.5
		26	4.0
		30	4.5
		33	5.0
		37	5.5
		41	6.0
		45	6.5

From Table 7.16, and by using Equation (7.14), for every incremental crack length (Δa), the gradient m can be defined as shown in Table 7.17.

Table 7.17 The complete calculation and results of gradient m for seven different toughness (n = 7) and ΔG = 0.5 N/mm

Incremental crack length (mm)	Δa	$\sum_{i=1}^{n} N_i$	$\sum_{i=1}^{n} G_i$	$\sum_{i=1}^{n} N_i G_i$	$\sum_{i=1}^{n} G_i^2$	$\left(\sum_{i=1}^{n} G_i\right)^2$	**m**
	0.1	63	35	329.000	182.000	1225.000	2.000
	0.2	81	35	422.000	182.000	1225.000	2.429
	0.3	105	35	548.000	182.000	1225.000	3.286
	0.4	126	35	658.000	182.000	1225.000	4.000
	0.5	145	35	757.500	182.000	1225.000	4.643
	0.6	163	35	852.500	182.000	1225.000	5.357
	0.7	182	35	952.000	182.000	1225.000	6.000
	0.8	200	35	1045.000	182.000	1225.000	6.429
	0.9	217	35	1136.000	182.000	1225.000	7.286
	1.0	234	35	1223.000	182.000	1225.000	7.571

By using the gradient m results from Table 7.17 for every incremental crack length, the next number of cycle can be predicted by using Equation (7.16) and the result is tabulated in Table 7.18.

Table 7.18 The complete calculation and results of predicted number of cycles N_{n+1} for seven difference toughness (n = 7) and ΔG = 0.5 N/mm

Incremental crack length	da	m	G_{i+1}	G^1_{i+1}	G^2_{i+1}	G^3_{i+1}	G^4_{i+1}	G^5_{i+1}	G^6_{i+1}	G^7_{i+1}
	0.1	2.00	6.50	7.00	10.50	14.00	17.50	21.00	24.50	124.30
	0.2	2.43	6.50	7.00	10.50	14.00	17.50	21.00	24.50	124.30
	0.3	3.29	6.50	7.00	10.50	14.00	17.50	21.00	24.50	124.30
	0.4	4.00	6.50	7.00	10.50	14.00	17.50	21.00	24.50	124.30
	0.5	4.64	6.50	7.00	10.50	14.00	17.50	21.00	24.50	124.30
	0.6	5.36	6.50	7.00	10.50	14.00	17.50	21.00	24.50	124.30
	0.7	6.00	6.50	7.00	10.50	14.00	17.50	21.00	24.50	124.30
	0.8	6.43	6.50	7.00	10.50	14.00	17.50	21.00	24.50	124.30
	0.9	7.29	6.50	7.00	10.50	14.00	17.50	21.00	24.50	124.30
	1.0	7.57	6.50	7.00	10.50	14.00	17.50	21.00	24.50	124.30

Incremental crack length	da	N_{i+1}	N^1_{i+1}	N^2_{i+1}	N^3_{i+1}	N^4_{i+1}	N^5_{i+1}	N^6_{i+1}	N^7_{i+1}
	0.1	12	13	20	27	34	41	48	248
	0.2	15	16	25	33	42	50	59	301
	0.3	20	22	33	45	56	68	79	407
	0.4	24	26	40	54	68	82	96	495
	0.5	28	30	47	63	79	95	112	575
	0.6	31	34	52	71	90	109	127	662
	0.7	35	38	59	80	101	122	143	742
	0.8	38	41	64	86	109	131	154	795
	0.9	42	46	71	97	122	148	173	900
	1.0	45	49	75	102	128	155	181	937

In the single overloading study, a fast-track method (FTM) is also implemented using various number of data points as illustrated in Table 7.19. The procedures are the same as in previous section. The results for calculation of gradient m are shown in Table 7.20 and then the predicted number of cycle is tabulated in Table 7.21.

Table 7.19 Number of cycle data for four difference toughness (n = 4) in incremental crack length for the single overloading case

		Variable Toughness (N/mm)			
Incremental crack length (mm)	da	5.9	10.5	14	17.5
	0.1	9	17	24	30
	0.2	12	23	32	41
	0.3	16	32	44	57
	0.4	19	39	55	70
	0.5	23	46	63	81
	0.6	26	52	72	92
	0.7	29	58	80	102
	0.8	32	64	88	113
	0.9	36	70	96	123
	1.0	38	76	104	132

Table 7.20 The gradient m for four difference toughness (n = 4) in incremental crack length for the single overloading case

Incremental crack length (mm)	Δa	$\sum_{i=1}^{n} N_i$	$\sum_{i=1}^{n} G_i$	$\sum_{i=1}^{n} N_i G_i$	$\sum_{i=1}^{n} G_i^2$	$\left(\sum_{i=1}^{n} G_i\right)^2$	m
	0.1	80	47.9	1092.60	647.31	2294.41	1.83
	0.2	108	47.9	1477.80	647.31	2294.41	2.50
	0.3	149	47.9	2043.90	647.31	2294.41	3.52
	0.4	183	47.9	2516.60	647.31	2294.41	4.41
	0.5	213	47.9	2918.20	647.31	2294.41	4.99
	0.6	242	47.9	3317.40	647.31	2294.41	5.69
	0.7	269	47.9	3685.10	647.31	2294.41	6.29
	0.8	297	47.9	4070.30	647.31	2294.41	6.97
	0.9	325	47.9	4443.90	647.31	2294.41	7.49
	1.0	350	47.9	4788.20	647.31	2294.41	8.10

Table 7.21 The predicted number of cycles N_{n+1} for four difference toughness (n = 4) in incremental crack length for the single overloading case

Incremental crack length (mm)	Δa	m	G_i	G_{i+1}	N_i	N_{i+1}
	0.1	1.83	17.5	124.3	30	225
	0.2	2.50	17.5	124.3	41	308
	0.3	3.52	17.5	124.3	57	433
	0.4	4.41	17.5	124.3	70	541
	0.5	4.99	17.5	124.3	81	614
	0.6	5.69	17.5	124.3	92	700
	0.7	6.29	17.5	124.3	102	774
	0.8	6.97	17.5	124.3	113	857
	0.9	7.49	17.5	124.3	123	923
	1.0	8.10	17.5	124.3	132	997

7.6 Results and Discussion

Figure 7.4 to 7.8 show the comparison of fatigue crack growth result between the fast-track method (FTM) and numerical results for different number of data points. It can be seen from figures that the number of data points affects the accuracy of the prediction. The detailed results for number of cycles for difference number of toughness are shown in Table 7.22.

The accuracy of the prediction can be considered from the relative error on results. Relative error $= \{\text{abs}(N_r - N_p)/N_r\} \times 100\%$, where N_r and N_p are the reference of the number of cycles and the prediction of the number of cycles, respectively. Figure 7.9 shows the relative error of results from using the fast-track method versus every incremental crack length for difference number of data. The largest error is 9.56 % in incremental crack length of 0.1 mm for two different toughness (n = 2). The smallest error is 0.02 % in incremental crack length of 0.9 mm for two different value of toughness (n = 2). However the average relative error has small value (0.51 %) for six different value of toughness (n = 6). The detail comparison of relative error between the fast-track method (FTM) and numerical results for varying number of data can be seen in Table 7.23. It can be seen from table that the number of data affect the accuracy of the prediction results. Large number of data can reduce the error of prediction results.

The CPU time (seconds) for different value of toughness can be shown in Table 7.24. There are two possible computational platforms that produce different relative efficiencies. Relative efficiency is define as $\{\text{abs}(t_r - t_p)/t_r\} \times 100\%$, t_r and t_p are the computational time to calculate the number of cycles for real toughness, and computational

time to calculate the prediction of number of cycles for artificial toughness, respectively. The first one is the use of a series computer where fatigue crack growth data is obtained sequentially for each toughness value on one computer. This means that for six different value of toughness, the total CPU time is the sum of each CPU time for each individual toughness value. The second possibility is a parallel computer where fatigue crack growth data for all toughness is obtained simultaneously on more than one computer processor. This means that for six different value of toughness, the total CPU time is dictated by the highest CPU time among different value of toughness. Figure 10 shows the relative efficiencies (%) for parallel and series computers. The use of the fast-track method can where relative efficiencies of some 91.49 % on a parallel computer system and 73.40 % on a series computer system. It is revealed that fast-track method can reduce significantly the CPU time.

The comparison of number of cyclic results between the fast-track method (FTM) and numerical results (Num) for different value of toughness using data range ΔG = 0.5 N/mm provided completely in Table 7.25. Table 7.26 shows the largest relative error is 9.56 % at 0.1 mm of incremental crack length for 124.3 N/mm of toughness. The largest average relative error is 2.53 % for 124.3 N/mm of toughness. Otherwise, the smallest average relative error is 1.34 % for 7 N/mm of toughness. It can be concluded that even though small toughness data range (ΔG = 0.5 N/mm) is considered, the fast-track method gives a good agreement generally in the prediction results.

Figure 7.11 shows the comparison of fatigue crack growth result between the fast-track method (FTM) using for two different interval toughness (ΔG = 0.5 and ΔG =

3.5 N/mm) and numerical (real toughness G_c = 124.3 N/mm). It can be seen that the interval toughness ΔG = 0.5 N/mm has some large difference result from numerical, particularly for 0.1 mm of incremental crack length. It is clearly seen from the relative error for two different interval toughness ΔG = 0.5 and ΔG = 3.5 N/mm as shown in Figure 7.12. It is shown that the interval toughness ΔG should be considered to increase the accuracy of prediction results in the fast-track method.

In the case study for single overloading, Table 7.27 provides a comparison of the number of cycles between the fast-track method and numerical results for three different value of toughness. Numerical results are obtained from computation approach for given toughness. It can be seen from table that the fast-track method provides the good accuracy for small variable toughness, but for larger toughness increase some error. The highest relative error of 10.1 % is for the incremental crack length (Δa) of 0.2 mm. In contrast, the smallest relative error of 1.32 % is for the incremental crack length (Δa) of 0.3 mm.

7.7 Summary

It can be concluded that the fast-track method provides good accuracy for small change toughness, but for larger change error increase. The highest relative error of 10.1 % is obtained for an incremental crack length (Δa) of 0.2 mm. In contrast, the smallest relative error of 1.32 % is recorded for the incremental crack length (Δa) of 0.3 mm. However in general the proposed method shows the excellent agreement to the numerical results obtained from a commercial package for constant amplitude

loading and single overloading. The fast-track methodology provides accurate prediction over a limited range of crack length extensions.

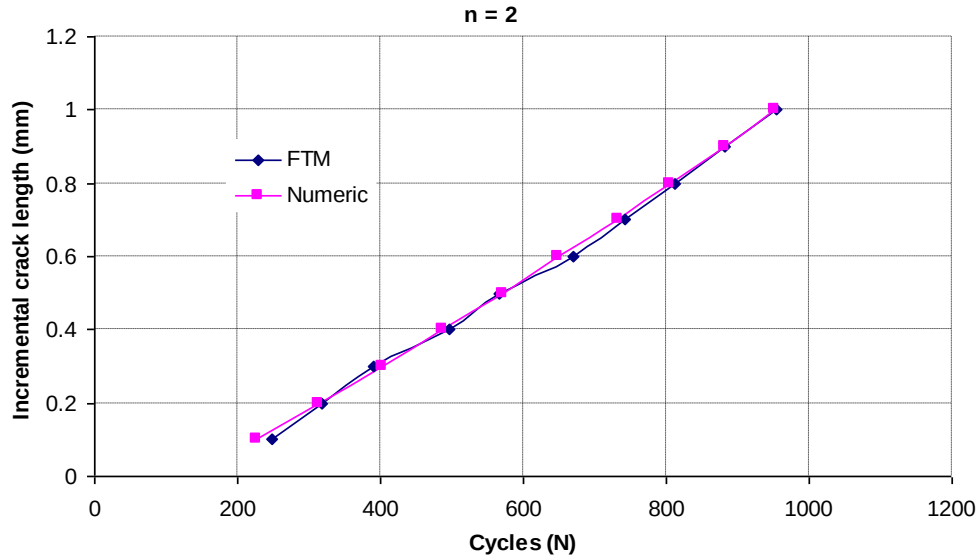

Figure 7.4 The comparison of fatigue crack growth result between the Fast-Track Method (FTM) and Numerical results for number of data n = 2

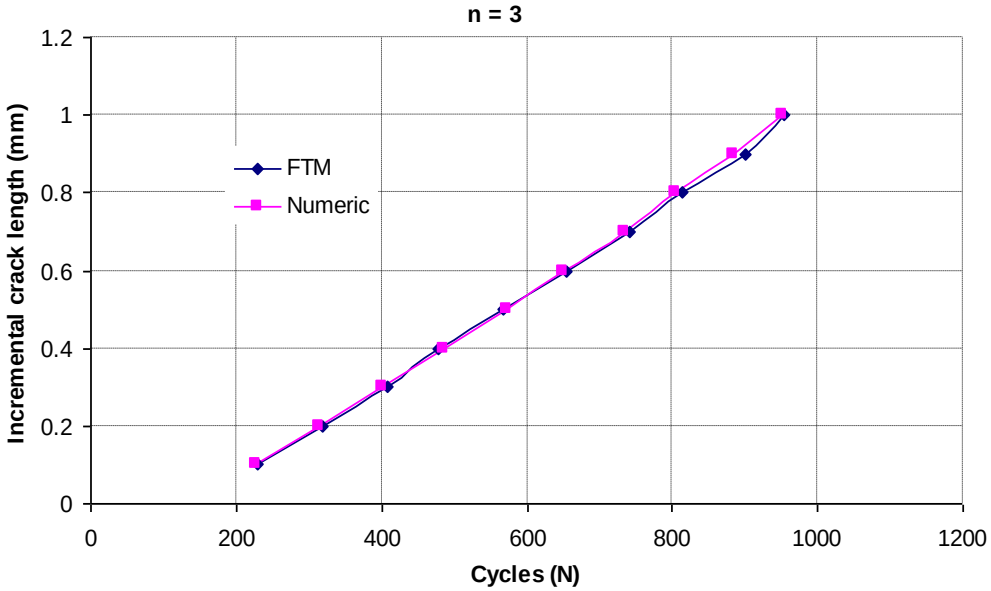

Figure 7.5 The comparison of fatigue crack growth result between the Fast-Track Method (FTM) and Numerical results for number of data n = 3

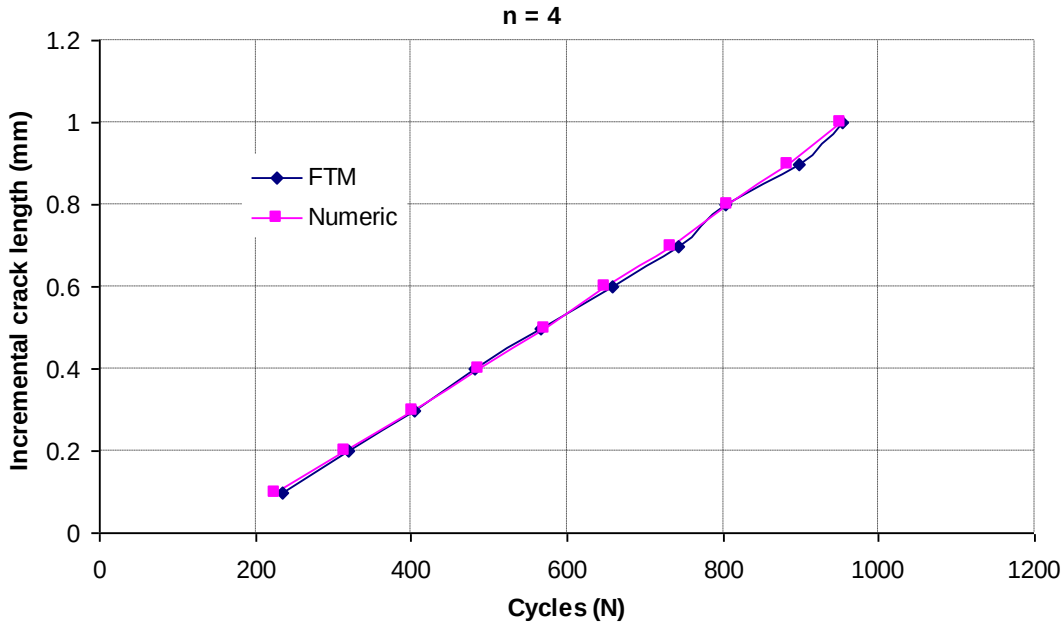

Figure 7.6 The comparison of fatigue crack growth result between the Fast-Track Method (FTM) and Numerical results for number of data n = 4

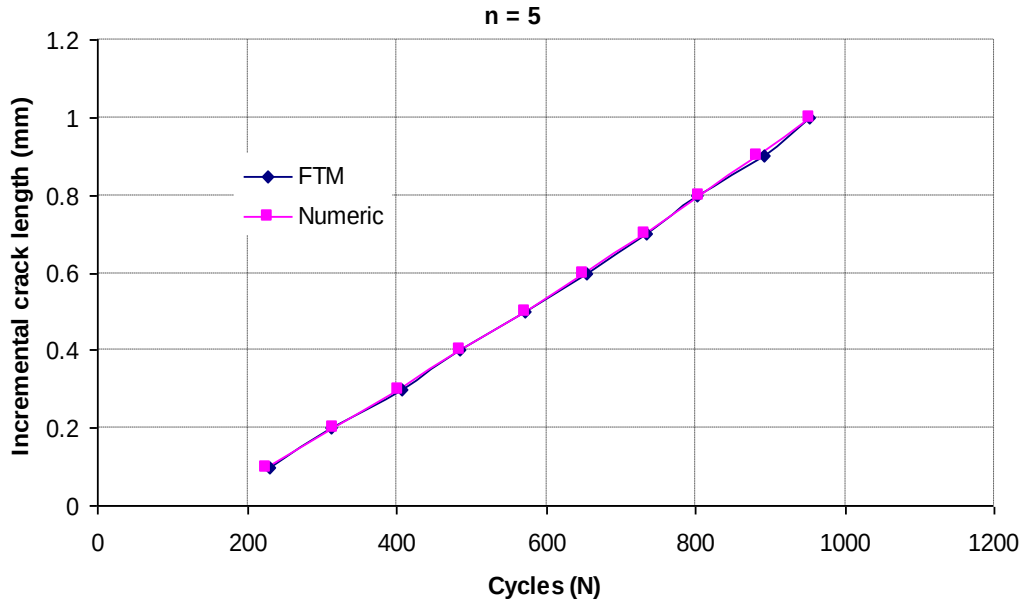

Figure 7.7 The comparison of fatigue crack growth result between the Fast-Track Method (FTM) and Numerical results for number of data n = 5

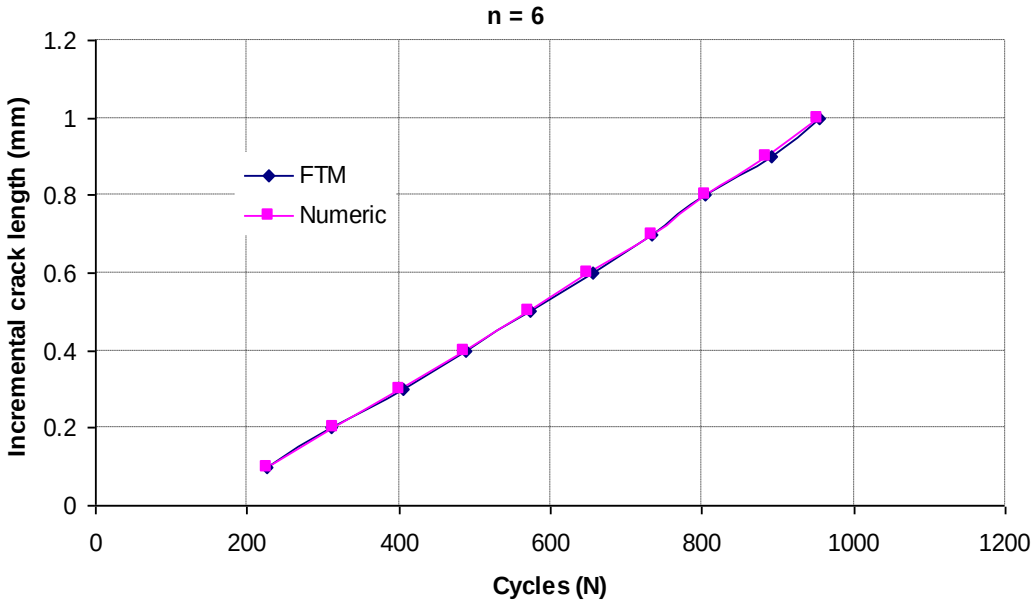

Figure 7.8 The comparison of fatigue crack growth result between the Fast-Track Method (FTM) and Numerical results for number of data n = 6

Table 7.22 The comparison of the number of cycle result between the Fast-Track Method (FTM) and Numerical results for varying number of data

		Fast-Track Method					Numerical
Incremental crack length (mm)	Δa	n =2	n = 3	n = 4	n = 5	n = 6	
	0.1	248	230	234	230	227	226
	0.2	319	319	319	312	311	314
	0.3	390	407	403	407	405	402
	0.4	495	478	482	485	487	486
	0.5	566	566	566	573	574	572
	0.6	671	654	657	654	655	649
	0.7	742	742	742	735	734	733
	0.8	813	813	802	803	804	805
	0.9	883	900	896	893	891	883
	1.0	954	954	954	954	954	952

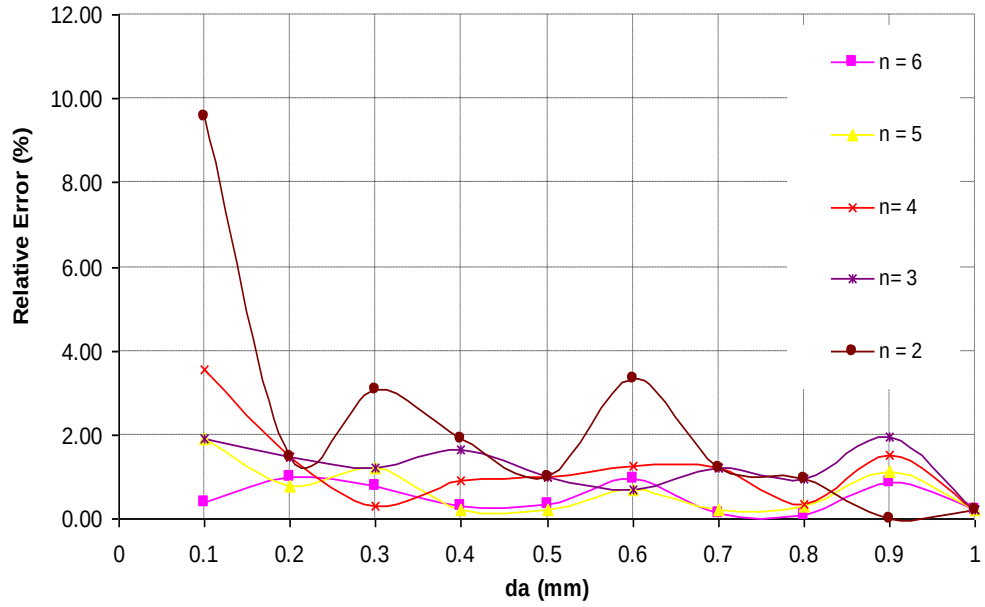

Figure 7.9 The comparison of relative error for varying number of data

Table 7.23 The comparison of relative error between the Fast-Track Method (FTM) and Numerical results for varying number of data

		Relative Error (%)				
Incremental crack length (mm)	Δa	n =2	n = 3	n = 4	n = 5	n = 6
	0.1	9.56	1.92	3.54	1.92	0.39
	0.2	1.47	1.47	1.47	0.79	0.99
	0.3	3.07	1.22	0.31	1.22	0.78
	0.4	1.89	1.66	0.91	0.20	0.30
	0.5	1.01	1.01	1.01	0.23	0.35
	0.6	3.35	0.70	1.26	0.70	0.97
	0.7	1.20	1.20	1.20	0.23	0.14
	0.8	0.97	0.97	0.33	0.29	0.09
	0.9	0.02	1.94	1.52	1.13	0.86
	1	0.20	0.20	0.20	0.20	0.20
Average		**2.27**	**1.23**	**1.17**	**0.69**	**0.51**

Table 7.24 CPU Time (second) for difference toughness

	Artificial Toughness (N/mm)							
	3.5	**7.0**	**10.5**	**14.0**	**17.5**	**21.0**	**Total**	**124.3**
CPU time	3375.6	5854.91	8790.09	11957.77	15477.32	21364.97	66820.66	251166.8

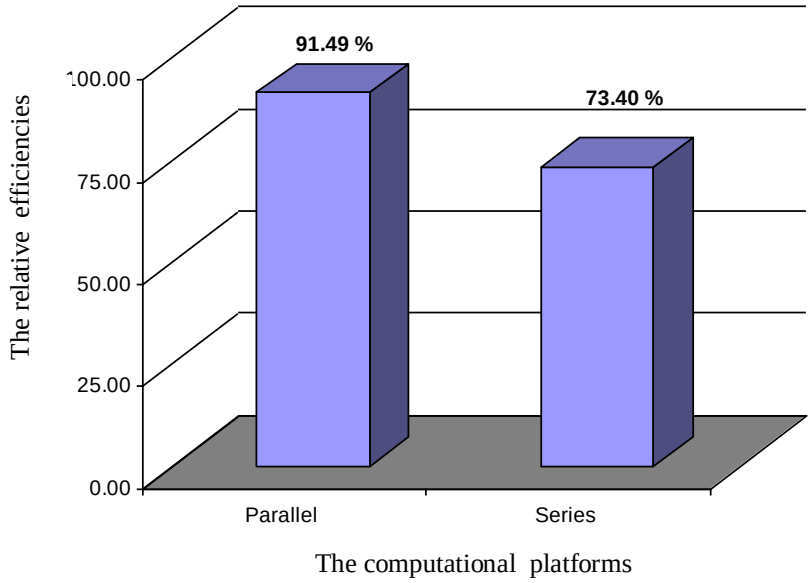

Figure 7.10 The relative efficiencies of CPU Time

Table 7.25 The comparison of number of cyclic results between the Fast-Track Method (FTM) and Numerical (Num) for difference toughness using interval data ΔG = 0.5 N/mm

Incremental crack length (mm)	Δa	14 N/mm		17.5 N/mm		21 N/mm		24.5 N/mm		124.3 N/mm	
		Num	FTM	Num	FTM	Num	FTM	Num	FTM	Num	FTM
	0.1	26	27	32	34	38	41	45	48	226	248
	0.2	35	33	43	42	52	50	61	59	314	301
	0.3	44	45	56	56	67	68	79	79	402	407
	0.4	53	54	67	68	81	82	95	96	486	495
	0.5	62	63	79	79	95	95	111	112	572	575
	0.6	71	71	89	90	108	109	126	127	649	662
	0.7	80	80	100	101	121	122	142	143	733	742
	0.8	87	86	110	109	133	131	156	154	805	795
	0.9	96	97	121	122	146	148	171	173	883	900
	1.0	103	102	130	128	157	155	184	181	952	937

Table 7.26 The relative error (%) for difference toughness using interval data ΔG = 0.5 N/mm

Incremental crack length (mm)	Δa	Relative Error (%)						
		7.0 N/mm	**10.5 N/mm**	**14 N/mm**	**17.5 N/mm**	**21 N/mm**	**24.5 N/mm**	**124.3 N/mm**
	0.1	0.00	5.26	3.85	6.25	7.89	6.67	9.56
	0.2	4.62	4.95	5.10	2.99	3.43	3.75	4.11
	0.3	3.06	0.43	1.46	0.26	0.96	0.18	1.26
	0.4	0.00	2.56	1.89	1.49	1.23	1.05	1.89
	0.5	1.07	1.24	1.32	0.09	0.34	0.51	0.51
	0.6	0.95	0.82	0.25	1.04	0.63	1.13	2.01
	0.7	0.00	0.00	0.00	1.00	0.83	0.70	1.20
	0.8	1.87	1.98	0.90	1.17	1.34	1.47	1.21
	0.9	1.43	0.20	0.67	0.94	1.13	1.25	1.95
	1.0	0.44	0.94	1.18	1.32	1.41	1.48	1.58
Average		1.34	1.84	1.66	1.66	1.92	1.82	2.53

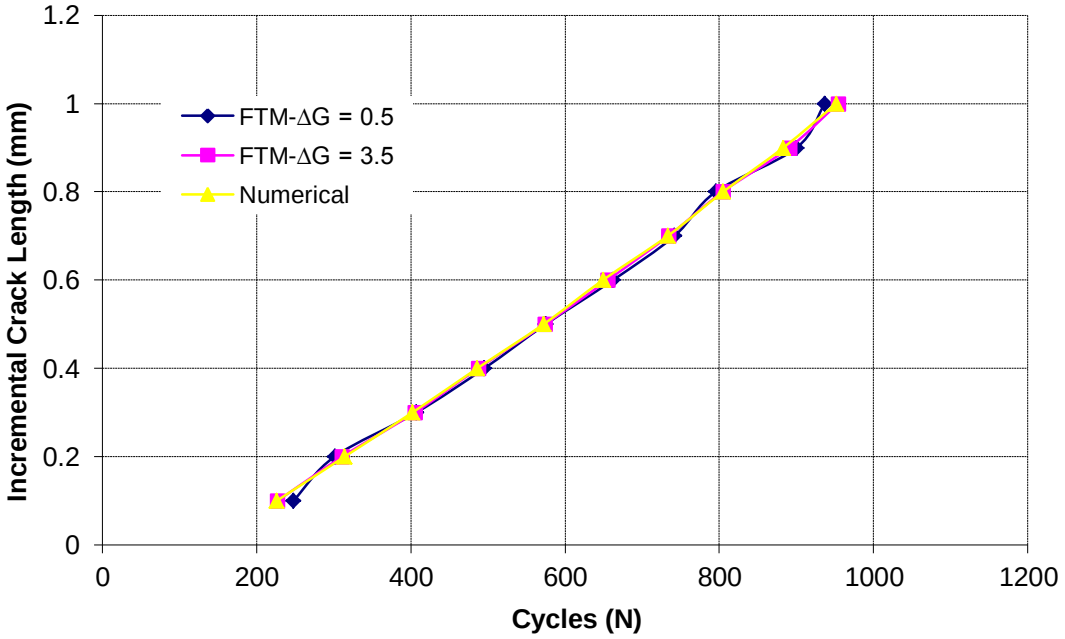

Figure 7.11 The comparison of fatigue crack growth result between the Fast-Track Method (FTM) and Numerical results for two difference interval artificial toughness ΔG = 0.5 and ΔG = 3.5 N/mm

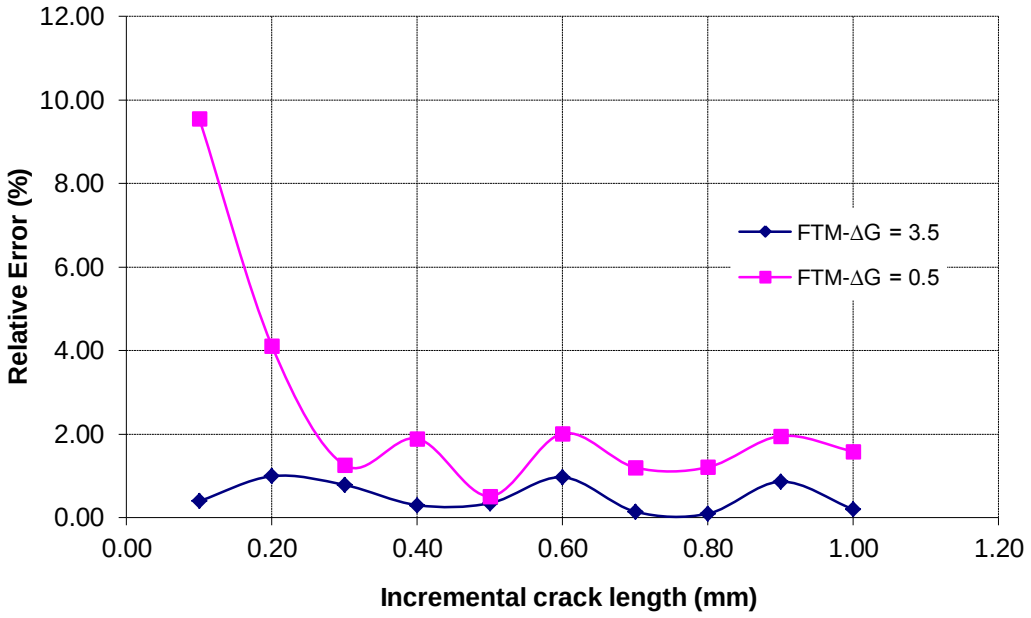

Figure 7.12 The comparison of relative error between the Fast-Track Method (FTM) and Numerical results for two difference interval toughness ΔG = 0.5 and ΔG = 3.5 N/mm

Table 7.27 The comparison results of the Fast-Track Method (FTM) and Numerical results for the single overloading case

Incremental crack length (mm)	Δa	21 N/mm		Relative Error	24.5 N/mm		Relative Error	124.3 N/mm		Relative Error
		Numerical	FTM		Numerical	FTM		Numerical	FTM	
	0.1	36	36	0	42	42	0	232	225	3.00
	0.2	50	50	0	59	59	0	278	308	10.91
	0.3	69	69	0	82	82	0	439	433	1.32
	0.4	85	85	0	100	100	0	561	541	3.53
	0.5	98	98	0	116	116	0	628	614	2.30
	0.6	112	112	0	131	131	0	715	700	2.13
	0.7	124	124	0	147	147	0	799	774	3.12
	0.8	137	137	0	161	161	0	876	857	2.13
	0.9	149	149	0	175	175	0	952	923	3.06
	1.0	161	161	0	189	189	0	1024	997	2.64

Chapter 8

Unified Fast Track Method and Extrapolation Methodology for Fatigue Crack Growth

8.1. Introduction

Recent developments in the field of fracture mechanics have led to increased interest in the prediction of fatigue life. The accurate prediction of component or structure service life is a common and current concern in many industries. The service life depends on material response due to service loading. In the case cyclic loading, material failure occurs as damage accumulates a phenomenon known as fatigue failure.

Fatigue crack growth analysis is conducted with the development of empirical models designed to predict growth rates. These models establishes relationship for stress intensity factor at the crack tip [16]. The relationship between the stress

intensity factor range and the crack propagation rate da/dN in fatigue problem was firstly introduced by Paris [1] and subsequently extended by some modification. These models are limited to the constant amplitude cyclic loading although in principle can be extended to piecewise constant loading using Milner's Rule.

In service loading, fatigue failure in materials may occur however under variable amplitude loading. Variable amplitude loading might only involve one high peak loading occurring during loading. This loading pattern is called overload. This type of loading modifies the fatigue crack behaviour, since fatigue crack growth rate depends greatly on the loading pattern. A high peak load can induce large incremental crack growth, and sometimes can retard crack growth in the following cycles. The retardation phenomenon is dependent on the overloading ratio. The overloading ratio is defined as the ratio of high peak loading over constant amplitude loading. An empirical model has been developed [47] to predict retarded fatigue crack growth rates. This model is based on experimental observations and modifications of a model used for constant amplitude loading. However, a major problem with this kind of empirical model for both constant and variable amplitude loading is the requirement to experimentally determine the various model parameters. These parameters depend on the material and need a number of experiments to be conducted.

This chapter is concerned with the development of a new methodology to predict the fatigue crack growth subject to small scale yielding. Small scale yielding occurs when the radius of the plastic zone at the crack tip is less than the current crack

length. The approach involves the combination of the fast-track method for preliminary simulation of fatigue crack growth as explained in Chapter 7 and new extrapolation methodology. The set of data obtained from the fast-track method is used to define parameters in an empirical model. The fatigue crack growth curve obtained from the new approach is compared with Forman empirical model and experimental results for the constant amplitude loading. It is demonstrated here how the new approach captures fatigue crack growth retardation due to variable amplitude loading. The retardation parameter is defined by evaluating the fatigue crack growth retardation in the application of varying toughness using the cohesive zone model.

8.2. Constant Amplitude Loading

In this study, a unified approach is presented combining the fast-track solution methodology and an extrapolation procedure. The fatigue crack growth curves for materials subject to constant amplitude loading (CAL) are developed. As explained in Chapter 7, the fast-track method establishes a functional relationship between the number of cycles and an artificial variable toughness. Underpinning the approach is an assumed linear relationship between variable toughness and the number of cycles. This assumption is only valid for small changes in crack length. To cater for longer changes, an alternative method is required.

The results obtained from the fast-track method in terms of the functional relationship between the number of cycles and the crack length provides starting

point for the fatigue crack growth prediction. The fast-track method is essentially on interpolation method and further crack growth prediction is to be achieved by means of an extrapolation procedure where an empirically established growth law is assumed applicable. The series of data which generated by the fast-track method can be used to determine parameters in an empirical model, i.e. C and n for Forman or Paris models, by means of curve fitting technique. Once the parameters are determined, the new function may be used to calculate the fatigue crack growth. The detail unified methodology can be seen in following flowchart.

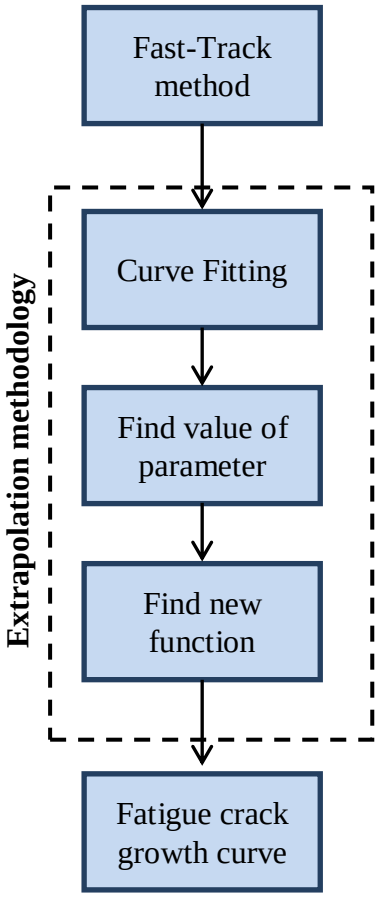

Figure 8.1 The flow chart of the unified Fast-track method and extrapolation methodology

8.2.1 Extrapolation Methodology

A modification to Paris's model is the one introduced by the Forman equation [3]. This model is widely used because it includes the effect of load ratio R and fracture toughness K_c. Forman equation takes into account the unstable crack growth rate as the maximum stress intensity factor approaches the fracture toughness. The equation can be shown in the following form

$$\frac{da}{dN} = \frac{C(\Delta K)^n}{(1-R)K_c - \Delta K} \tag{8.1}$$

where C and n are material parameters that are commonly determined by experiment. However in this current study, both parameters are defined by an alternative method involving on a best fit through a set of data obtained numerically from the fast-track solution.

Curve fitting is a method for determining an approximation function $p(x)$ which is "best fit" for a given set of data. The function $p(x)$ can then be used to find points anywhere along the curve. Since the set of data is expected to fit a specific function $f(x)$ so using an approximation function $p(x)$ means limited the accuracy. The accuracy is a measure of "closeness" of the approximate solution to the exact solution or the set of data. The accuracy is typically characterized by an error which is obtained from the difference between $p(x)$ and $f(x)$. The error in this study are calculated in terms of

$$E_x = \max_{a \le x \le b} \left(\frac{f(x) - p(x)}{f(x)} \right)^2 \tag{8.2}$$

where a and b are interval data in function $p(x)$.

In this study, the approximation function $p(x)$ has been determined by using the Forman equation from equation (8.1).

$$\frac{da}{dN} = p(a) \tag{8.3}$$

where $p(a) = \left(C(\Delta K)^n\right) \cdot \left((1-R)K_c - \Delta K\right)^{-1}$ and a is crack length.

Since the number of cycle is of interest, Equation (8.3) can be integrated to give

$$\int_{N_i}^{N_{i+1}} dN = \int_{a_i}^{a_{i+1}} \frac{1}{p(a)} da \tag{8.4}$$

By using the trapezoidal rule, the integration can be resolved numerical to give

$$N_{i+1} = N_i + \left\{0.5 \times \left(\frac{\Delta a}{p(a_{i+1})} + \frac{\Delta a}{p(a_i)}\right)\right\} \tag{8.5}$$

Parameter n and C are selected to obtain the best fit through set of data obtained from the fast-track solution. This is obtained by the minimization of the error using Equation (8.2).

8.2.2 Case Study

8.2.2.1 Material Properties

The value of cohesive energy or toughness G_c of 124.3 N/mm for AL2024-T3 has been calculated from the fracture toughness value of $K_c = 95.31\ MPa\sqrt{m}$ [83]. The value of the critical cohesive traction σ_c for various cohesive laws has been

estimated mostly based on the initial yield stress σ_Y and sometimes based on the ultimate tensile strength σ_u. Li and Siegmund [86] suggested that the ratio σ_c/σ_Y ranges from 1.2 to 4 for different conditions and for their model. They used $2\sigma_y$ as the critical cohesive traction. In this current study, the critical cohesive traction is 1.3 σ_Y in line with the assumption of the small scale yielding. The materials properties are tabulated in Table 8.1.

Table 8.1 Mechanical properties [83]

Young's Modulus E **(MPa)**	**Yield Stress** σ_Y **(MPa)**	**Poison's ratio** ν	**Critical Cohesive Traction** σ_c **(MPa)**	**Toughness** G_c **(N/mm)**
73100	324	0.3	421.2	124.3

8.2.2.2 Model Description

In this analysis, a model consisting [83] of 17.7 mm crack length (a) with 50 mm of height (h) and 52 mm of width (w) as shown on Figure 8.2(a). The crack is assumed to propagate along the axis of symmetry of the model. The cohesive interface of 210 elements is therefore arranged along the axis of symmetry of the model. The model is meshed with 12680 quadratic triangular elements. The constant amplitude loading (CAL) subjected to the model with a maximum stress loading (S_{max}) of 21.3 MPa and 29.3 MPa with load ratio $R = S_{min}/S_{max}$ = 0 applied uniformly on the edge top of plate as a sinusoidal function.

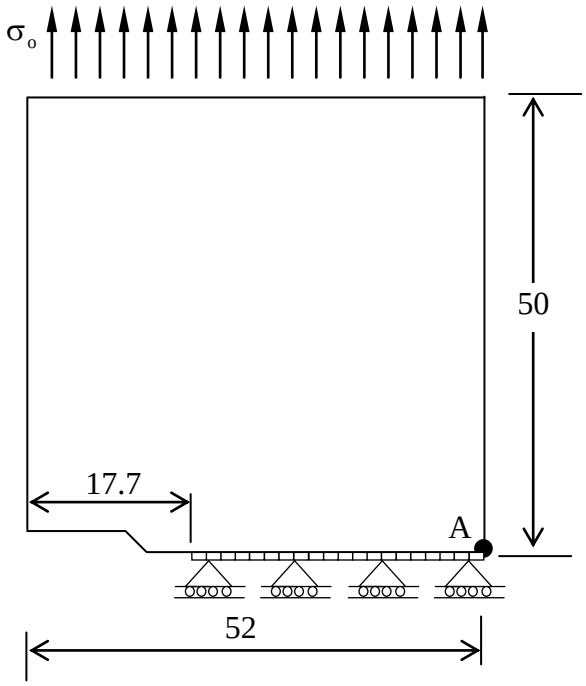

(a) Model geometry

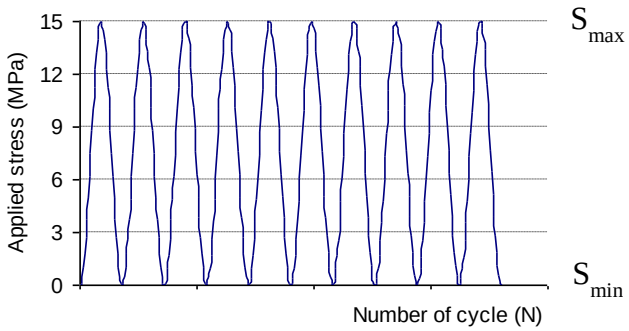

(b) Constant amplitude loading

Figure 8.2 The schematics test model loading and constraint

8.2.2.3 The Fast-Track Solution Methodology

In this study, the number of variable toughness required to apply the fast track methodology is divided into two groups as presented in Table 8.2. The first group consists of two different toughness values, i.e. the lowest and the highest value of

artificial toughness. The second group has six different value of artificial toughness. The results from fast-track solution are compared with the Forman equation. The values of Forman constants for the material considered are $C = 1 \times 10^{-5}$ and $n = 3.2094$ [83].

Table 8.2 The number of data for variable toughness

Data (n)	Variable Toughness (N/mm)					
2	5.00	17.50				
6	5.00	7.50	10.00	12.45	15.00	17.50

8.2.2.4 Results and Discussion

8.2.2.4.1 Fast-Track Solution

Table 8.3 and 8.4 present the results obtained from the preliminary computation of the number of cycles for different toughness value for the applied loading of 21.3 MPa and 29.3 MPa, respectively. The number of cycles for each incremental crack length (Δa) is shown in both tables. As preliminary computation, the fast-track method considers total crack extension of 1 mm. From the available data, the number of cycles for the real toughness (G_c= 124.3 N/mm) is predicted as shown in Table 8.5 and 8.6.

Table 8.5 and 8.6 compare the number of cycles obtained from the fast-track method (FTM) solution for different number of data (n = 2 and n = 6) and the Forman equation for the applied loading of 21.3 MPa and 29.3 MPa, respectively. It can be seen from the data in both tables that there is good agreement for both result obtained with n = 2 and n = 6. In addition, a positive correlation is found between the fast

track-method (FTM) and the Forman equation. The comparison of those results also is presented in Figure 8.3 and 8.4

The results of this study indicate that the amount of data does not significantly affect the accuracy of the results if data chosen is first and last value. This arises because the assumed linear relation between number of cycles and different toughness is valid. It is interesting to note that in all case studies, the results are in good agreement with the empirical model (Forman equation).

Table 8.3 Number of cycles from numerical results for loading of 21.3 MPa in varying toughness

		Toughness (N/mm)					
Incremental crack length (mm)	**Δa**	**5.0**	**7.5**	**10.0**	**12.45**	**15.0**	**17.5**
	0.1	26	41	56	71	87	105
	0.2	43	70	98	127	160	196
	0.3	59	93	131	170	213	260
	0.4	74	119	168	219	278	343
	0.5	89	142	200	261	330	406
	0.6	104	167	235	308	392	484
	0.7	118	189	267	348	441	543
	0.8	132	213	301	393	500	617
	0.9	146	234	330	429	545	670
	1.0	159	255	359	468	595	730

Table 8.4 Number of cycles from numerical results for loading of 29.3 MPa in varying toughness

		Toughness (N/mm)					
Incremental crack length (mm)	**Δa**	**5.0**	**7.5**	**10.0**	**12.45**	**15.0**	**17.5**
	0.1	9	15	22	27	33	39
	0.2	15	25	35	44	54	64
	0.3	21	37	51	65	79	94
	0.4	27	47	65	83	102	121
	0.5	34	57	80	102	126	149
	0.6	39	67	93	119	148	175
	0.7	45	77	108	138	171	202
	0.8	51	86	121	154	191	226
	0.9	56	95	133	170	211	250
	1.0	61	103	145	186	230	272

Table 8.5 Number of cycles from Forman equation and the Fast-track method (FTM) for loading of 21.3 MPa

Crack length (mm)	17.8	17.9	18.0	18.1	18.2	18.3	18.4	18.5	18.6	18.7
Forman Eq.	707	1397	2071	2728	3370	3996	4608	5205	5787	6356
FTM n=2	780	1503	1977	2641	3114	3730	4173	4760	5146	5607
FTM n=6	774	1495	1974	2630	3105	3717	4160	4742	5129	5595

Table 8.6 Number of cycles from Forman equation and the Fast-track method (FTM) for loading of 29.3 MPa

Crack length (mm)	17.8	17.9	18.0	18.1	18.2	18.3	18.4	18.5	18.6	18.7
Forman Eq,	244	483	715	942	1164	1380	1591	1796	1997	2193
FTM n=2	295	483	718	924	1131	1337	1543	1721	1907	2074
FTM n=6	294	480	711	918	1131	1334	1541	1719	1904	2075

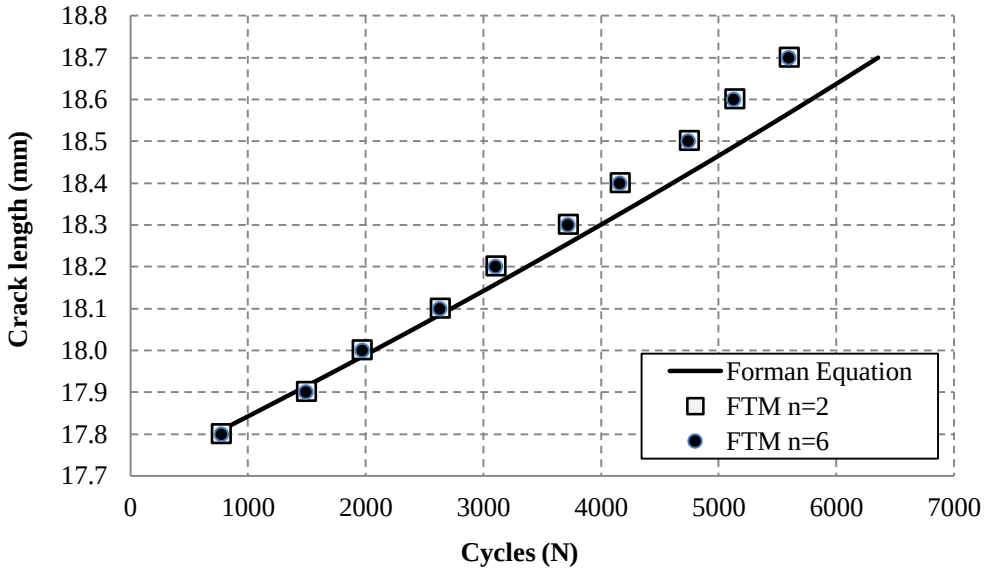

Figure 8.3 Fatigue crack growth for load of 21.3 MPa

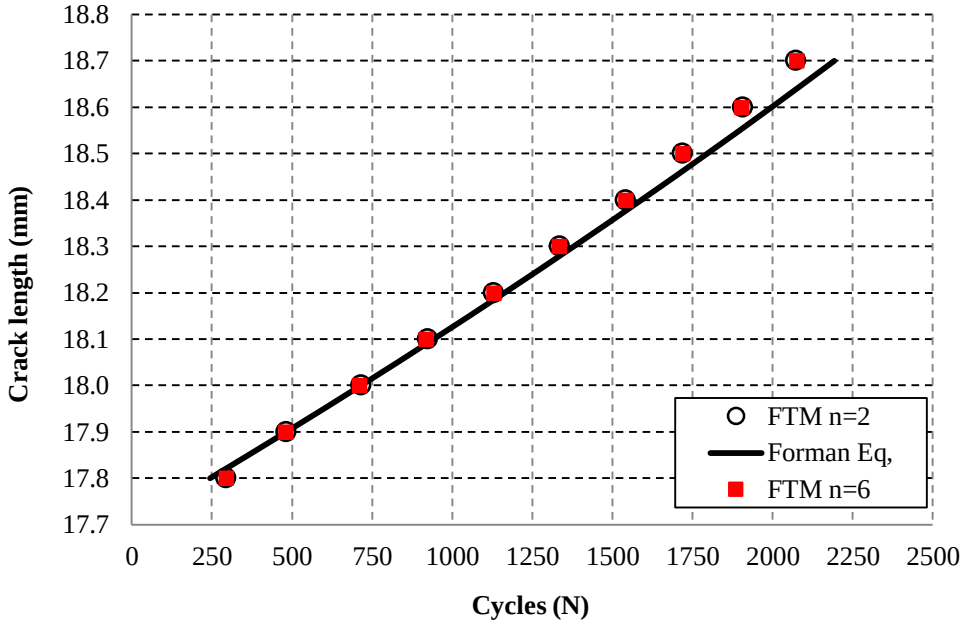

Figure 8.4 Fatigue crack growth for load of 29.3 MPa

8.2.2.4.2 Extrapolation Methodology

The preliminary results from the fast-track method can be used to define both parameters n and C value in the Forman equation. This equation can then be implemented as an extrapolation methodology to determine the complete crack growth curve. In this study, a value of C is given then a value range of n are adjustment and a comparison is made with the results obtained from the fast-track method (FTM) as indicated in Table 8.7 to 8.12.

Table 8.7 to 8.9 contrast the results of the number of cycle obtained from adjustment of n and C parameter values and the fast-track method for the applied loading of 21.3 MPa. In addition, for the applied loading of 29.3 MPa, the results are provided in Table 8.10 to 8.12. All tables show the number of cycles for each incremental crack

length. The value of n and C parameter will be considered by means of the minimum value of error from Equation (8.2) as shown in Figures 8.5 to 8.10. It can be seen from the figures that each C value has a different value of n associated with it.

Table 8.7 The comparison results of Curve fitting and the Fast-track method (FTM) for C = 0.000011 and the applied loading of 21.3 MPa

a (mm)	FTM	n - parameter					
		3.15	3.16	3.17	3.18	3.19	3.2
17.8	774	733	717	701	686	671	656
17.9	1495	1449	1417	1386	1356	1326	1297
18.0	1974	2148	2101	2054	2009	1965	1922
18.1	2630	2830	2768	2707	2648	2589	2532
18.2	3105	3497	3420	3345	3271	3199	3128
18.3	3717	4148	4057	3967	3879	3794	3710
18.4	4160	4784	4678	4575	4473	4375	4278
18.5	4742	5404	5285	5168	5053	4942	4832
18.6	5129	6011	5877	5747	5620	5495	5373
18.7	5595	6602	6456	6312	6172	6035	5901

Table 8.8 The comparison results of Curve fitting and the Fast-track method (FTM) for C = 0.000012 and load of 21.3 MPa

a (mm)	FTM	n - parameter					
		3.11	3.12	3.13	3.14	3.15	3.16
17.8	774	734	718	702	687	672	657
17.9	1495	1451	1419	1388	1358	1328	1299
18.0	1974	2152	2104	2058	2013	1969	1926
18.1	2630	2836	2774	2713	2653	2595	2537
18.2	3105	3504	3427	3352	3278	3206	3135
18.3	3717	4157	4066	3976	3888	3802	3718
18.4	4160	4795	4689	4586	4484	4385	4288
18.5	4742	5418	5298	5181	5066	4954	4844
18.6	5129	6027	5893	5762	5635	5510	5388
18.7	5595	6621	6474	6330	6190	6052	5918

Table 8.9 The comparison results of Curve fitting and the Fast-track method (FTM) for C = 0.000013 and load of 21.3 MPa

a (mm)	FTM	n - parameter					
		3.08	3.09	3.10	3.11	3.12	3.13
17.8	774	724	708	693	678	663	648
17.9	1495	1432	1400	1370	1340	1310	1281
18.0	1974	2123	2076	2031	1986	1943	1900
18.1	2630	2799	2737	2677	2618	2560	2504
18.2	3105	3459	3382	3308	3235	3164	3094
18.3	3717	4103	4013	3924	3838	3753	3670
18.4	4160	4733	4629	4526	4426	4328	4233
18.5	4742	5349	5230	5115	5001	4891	4782
18.6	5129	5950	5818	5689	5563	5440	5319
18.7	5595	6537	6392	6250	6112	5976	5843

Table 8.10 The comparison results of number cycles between Curve fitting and the Fast-track method (FTM) for C = 0.000011 and load of 29.3 MPa

a (mm)	FTM	n - parameter					
		3.15	3.16	3.17	3.18	3.19	3.2
17.8	294	258	252	245	239	233	227
17.9	480	510	497	485	473	461	449
18.0	711	756	737	719	701	683	666
18.1	918	996	971	947	923	900	877
18.2	1131	1231	1200	1169	1140	1111	1083
18.3	1334	1459	1423	1387	1352	1318	1285
18.4	1541	1683	1640	1599	1559	1519	1481
18.5	1719	1901	1853	1806	1760	1716	1673
18.6	1904	2114	2060	2008	1957	1908	1860
18.7	2075	2321	2263	2205	2150	2095	2042

Table 8.11 The comparison results of number cycles between Curve fitting and the Fast-track method (FTM) for C = 0.000012 and load of 29.3 MPa

a (mm)	FTM	n - parameter					
		3.11	3.12	3.13	3.14	3.15	3.16
17.8	294	262	255	249	243	237	231
17.9	480	517	505	492	480	468	456
18.0	711	767	748	729	711	693	676
18.1	918	1011	986	961	937	913	890
18.2	1131	1249	1218	1187	1157	1128	1100
18.3	1334	1481	1444	1408	1372	1338	1304
18.4	1541	1708	1665	1623	1582	1543	1504
18.5	1719	1930	1881	1834	1788	1742	1698
18.6	1904	2146	2092	2039	1988	1938	1889
18.7	2075	2358	2298	2240	2183	2128	2074

Table 8.12 The comparison results of number cycles between Curve fitting and the Fast-track method (FTM) for C = 0.000013 and load of 29.3 MPa

a (mm)	FTM	n - parameter					
		3.08	3.09	3.1	3.11	3.12	3.13
17.8	294	261	254	248	242	236	230
17.9	480	515	503	490	478	466	454
18.0	711	764	745	726	708	690	673
18.1	918	1007	982	957	933	910	887
18.2	1131	1244	1213	1183	1153	1124	1096
18.3	1334	1476	1439	1403	1367	1333	1300
18.4	1541	1703	1660	1618	1577	1537	1499
18.5	1719	1924	1875	1828	1782	1737	1693
18.6	1904	2140	2085	2033	1981	1931	1882
18.7	2075	2350	2291	2233	2176	2121	2068

Figures 8.11 to 8.13 present the prediction and the Forman equation of fatigue crack growth curve for applied loading of 21.3 MPa by applying the difference value of n and fixed value of C = 0.000011, C = 0.000012 and C =0.000013, respectively. It can be seen from figures that value of n = 3.18, n = 3.14 and n = 3.11 give excellent agreement with the Forman equation for value of C = 0.000011, C = 0.000012 and C =0.000013, respectively.

Figures 8.14 to 8.16 indicate the prediction and the Forman equation of fatigue crack growth curve for applied loading of 29.3 MPa by implementing the difference value of n and fixed value of C = 0.000011, C = 0.000012 and C = 0.000013, respectively for comparison. The figures show that value of n = 3.18, n = 3.15 and n = 3.12 have an excellent agreement with the Forman equation for value of C = 0.000011, C = 0.000012 and C =0.000013, respectively.

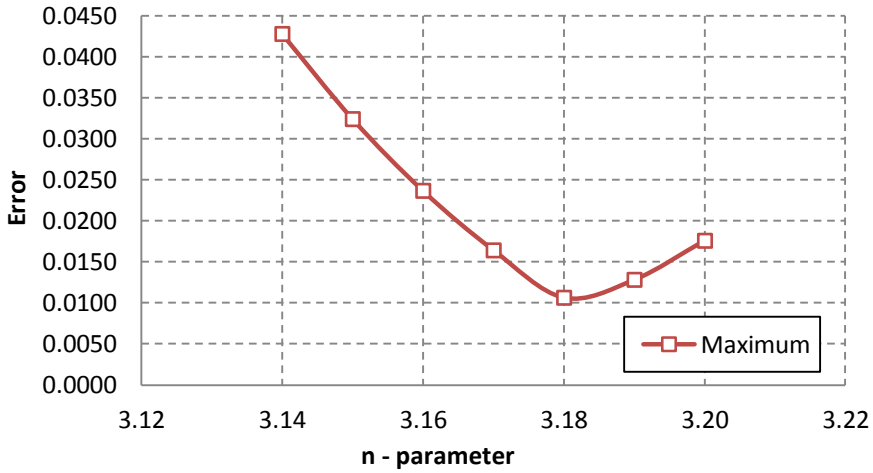

Figure 8.5 Error for C = 0.000011 and load of 21.3 MPa

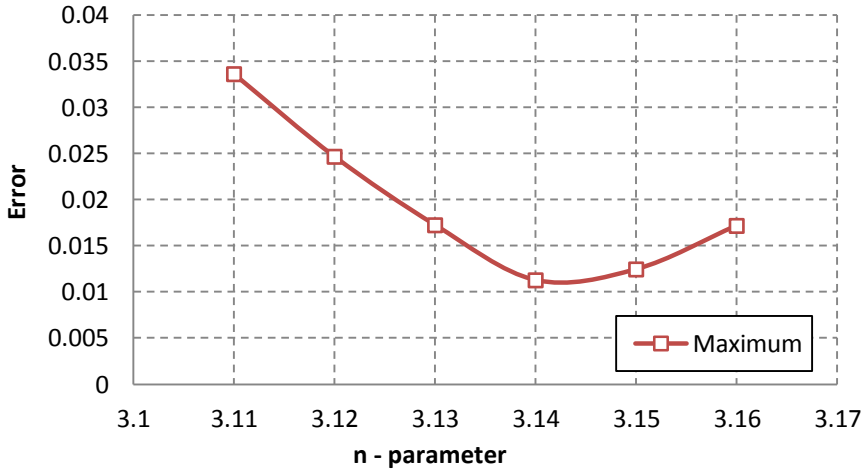

Figure 8.6 Error for C = 0.000012 and load of 21.3 MPa

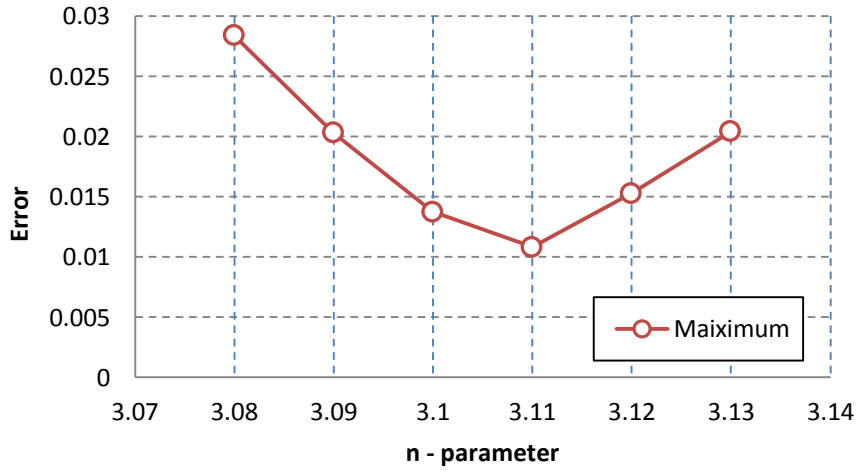

Figure 8.7 Error for C = 0.000013 and load of 21.3 MPa

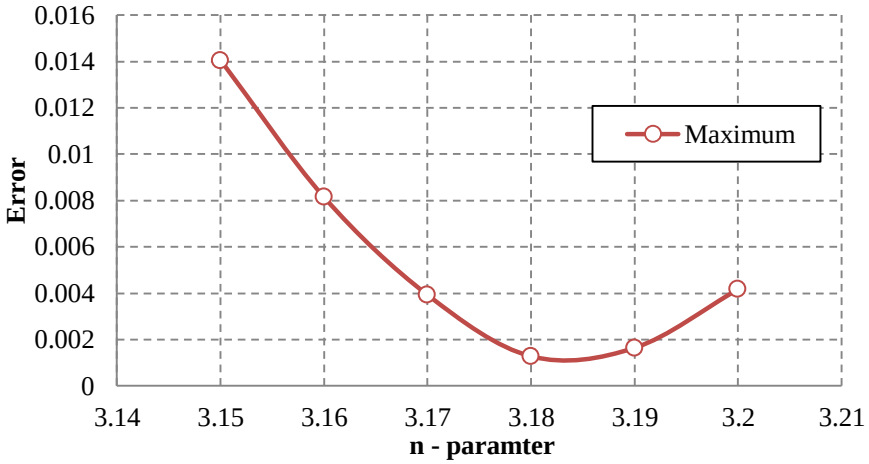

Figure 8.8 Error for C = 0.000011 and load of 29.3 MPa

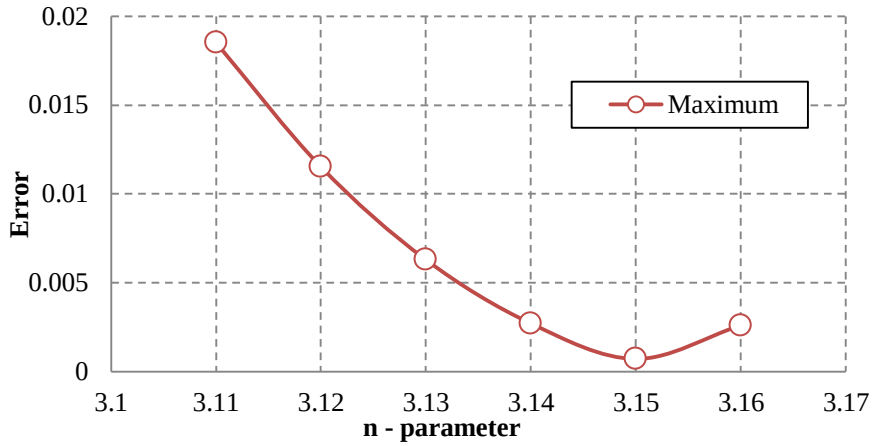

Figure 8.9 Error for C = 0.000012 and load of 29.3 MPa

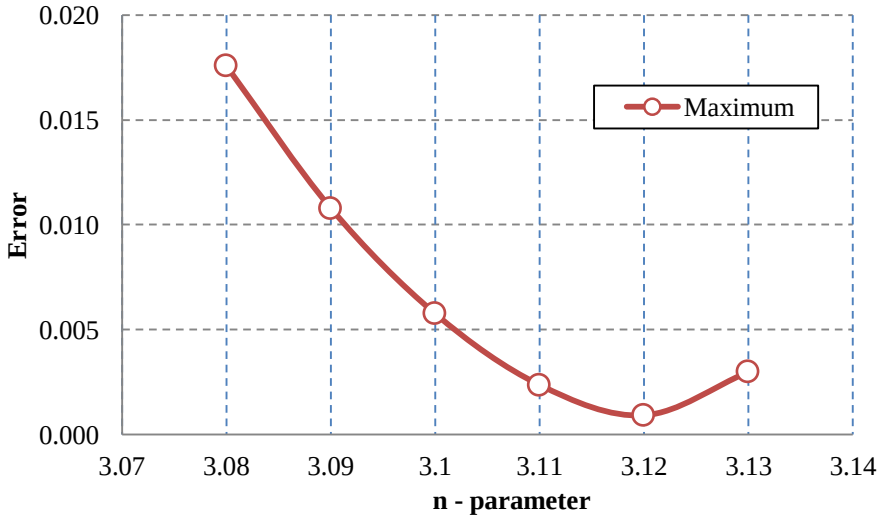

Figure 8.10 Error for C = 0.000013 and load of 29.3 MPa

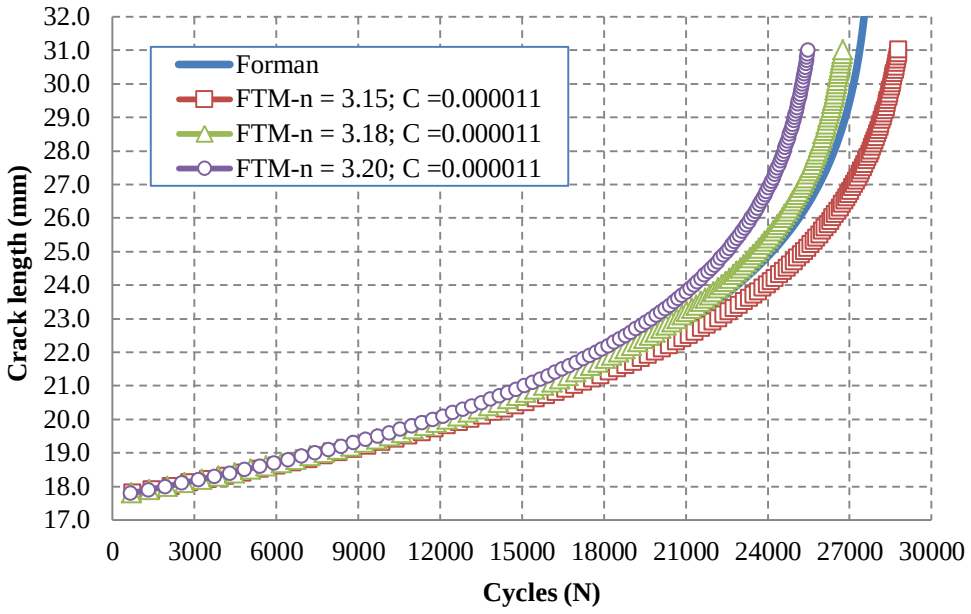

Figure 8.11 Fatigue crack growth for different values of n for C = 0.000011 and load of 21.3 MPa

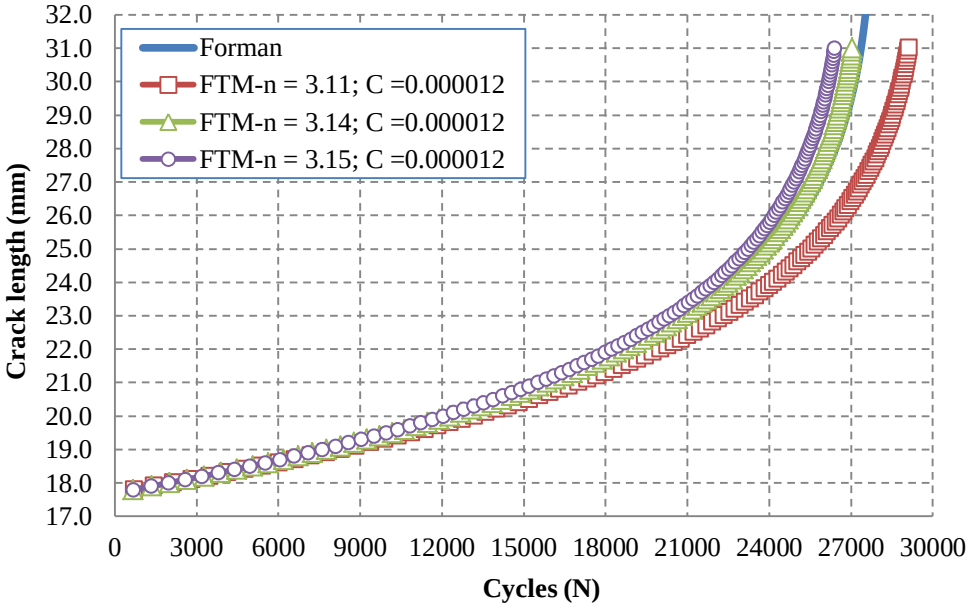

Figure 8.12 Fatigue crack growth for different values of n for C = 0.000012 and load of 21.3 MPa

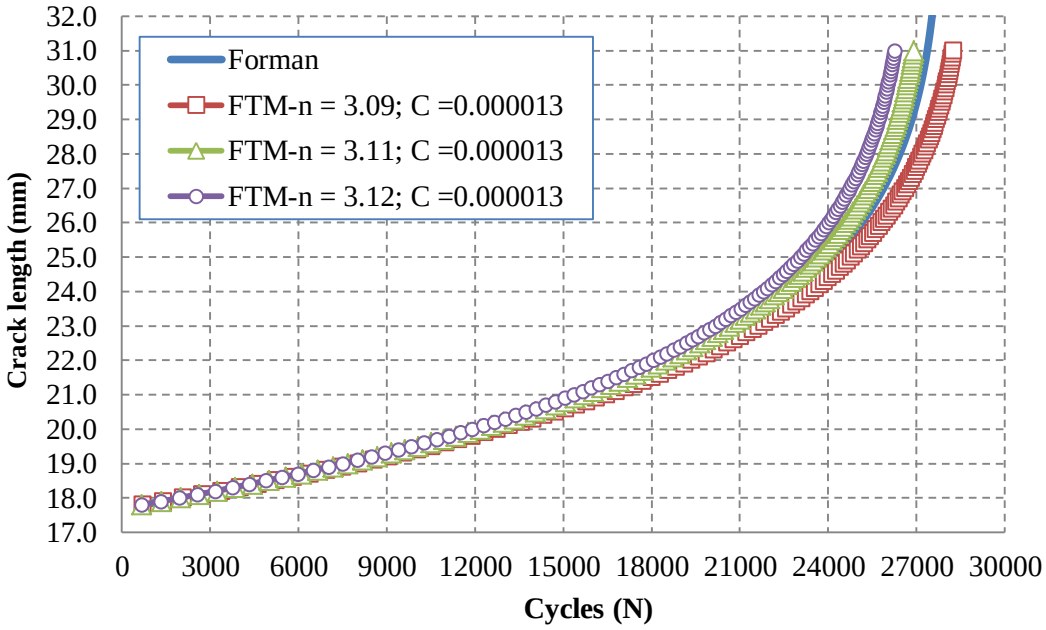

Figure 8.13 Fatigue crack growth for different values of n for C = 0.000013 and load of 21.3 MPa

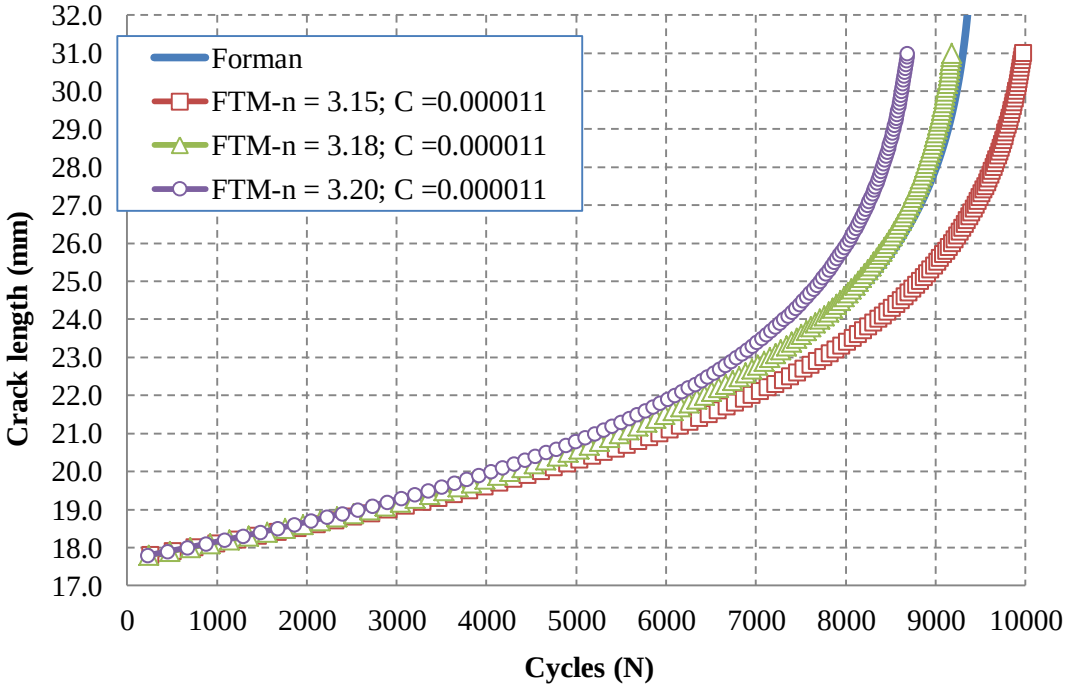

Figure 8.14 Fatigue crack growth for different values of n for C = 0.000011 and load of 29.3 MPa

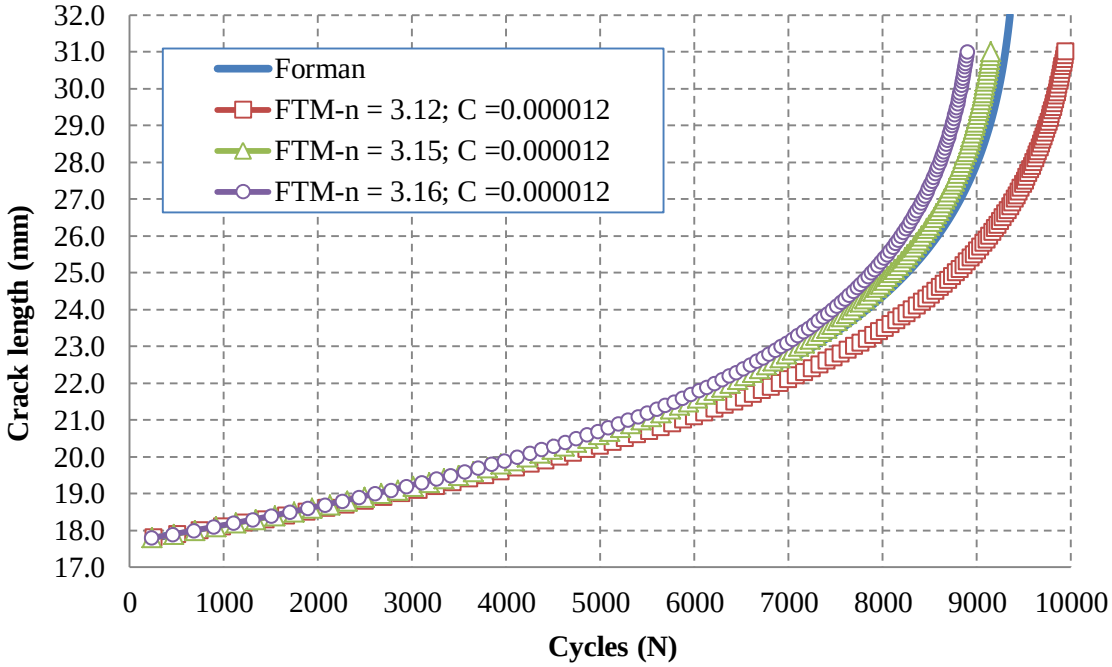

Figure 8.15 Fatigue crack growth for different values of n for C = 0.000012 and load of 29.3 MPa

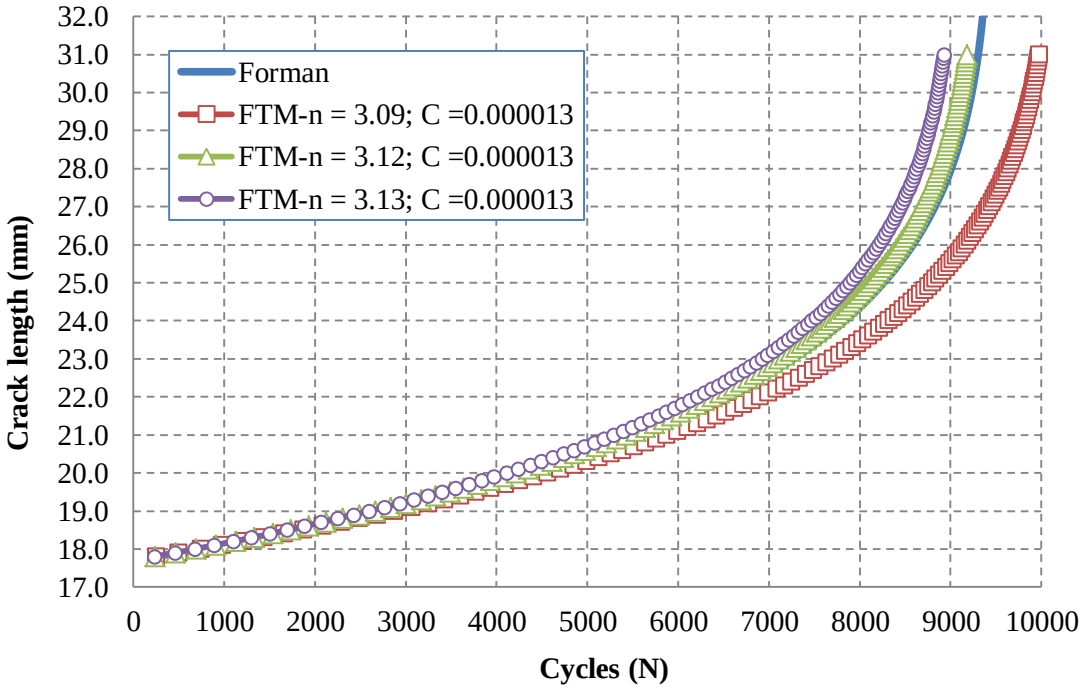

Figure 8.16 Fatigue crack growth for different values of n for C = 0.000013 and load of 29.3 MPa

Figure 8.17 shows a comparison of fatigue crack growth curves produced by the fast-track method and experimental results [83]. In accordance with the results presented in reference [83] stable power-law growth is assumed to be established after 90,000 cycles. Adopting the same starting number of cycles and on application of the fast-track method provides the curves in Figure 8.17. It can be seen from the figure that the new methodology with various constant parameters provide excellent agreement with the experimental results [83] over an initial range of cycles. In the case of n = 3.01 and C = 0.000013 however (which provides the smallest initial error) excellent agreement with experimental results [83] is obtained for all crack lengths.

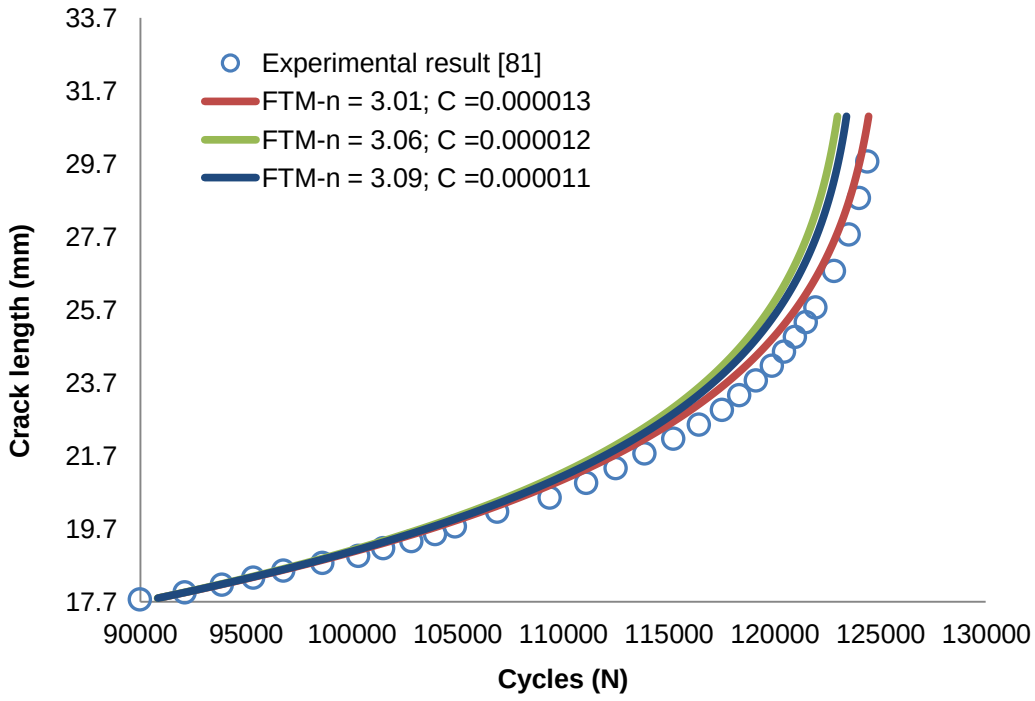

Figure 8.17 Fatigue crack growth for the Fast-track method (FTM) results with various constant parameter and experimental results

8.3. Variable Amplitude Loading

A significant aspect of fatigue crack growth is the retardation concept under variable amplitude loading. The earliest models introduced by Wheeler [47] in consideration of the retardation effect are based on the calculation of the plastic zone size and the reversed plastic zone ahead of the crack tip. Wheeler argued that the application of an overload on a constant amplitude loading induced a large plastic zone ahead of the crack tip. During the processing of fatigue cycles, the crack grows through the plastic zone which retards crack growth as consequence of compressive residual stress bearing down on the tearing the crack. To account for this Wheeler proposed the equation

$$\left(\frac{da}{dN}\right)_{VAL} = \left(C_p\right)\left(\frac{da}{dN}\right)_{CAL} \tag{8.6}$$

where C_p is a retardation factor which may be expressed in

$$\left(C_p\right)_i = \left(\frac{r_{pi}}{\left[a_{ol} + r_{p0} - a_i\right]}\right)^p \tag{8.7}$$

where P is parameter which determined by experiment. Subscript VAL and CAL denote variable amplitude loading and constant amplitude loading, respectively. Here r_{pi} and r_{p0} are the radius of plastic zone for current cycle loading and the plastic zone due to overloading, respectively. In the Irwin's model [61], the radius of plastic zone due to overloading can be calculated from

$$r_{po} = \frac{1}{\pi}\left(\frac{K_{ol}}{\sigma_Y}\right)^2 \tag{8.8}$$

where K_{ol} is the stress intensity factor for overloading. A modified Wheeler's model is considered in reference [64] where a plastic zone correction factor λ is introduced in the expression for instantaneous cycle in a compressive stress field, i.e.

$$r_{pi} = \lambda\left(\frac{1}{\pi}\right)\left(\frac{\Delta K}{2\sigma_Y}\right)^2 \tag{8.9}$$

The amount of retarded fatigue crack growth increases with the magnitude of the overloading applied. As consequence of this, the number of cycles required to grow through the plastic zone created by the peak loading will increase.

8.3.1 Methodology

In this study, the phenomenon of retarded fatigue crack growth is investigated by using the cohesive zone model with two different value of toughness. At this stage, the ratio of number of cycles delayed is measured and the ratio is used in place of the parameter as shown in Equation (8.7). By means Equation (8.6) the fatigue crack growth curve is constructed.

8.3.2 Case Study

In the current study, the retardation phenomenon due to variable amplitude loading is investigated. By continuing the analysis of fatigue crack growth for constant amplitude loading from previous section, the model and materials is the same as the previous analysis. Three case studies are presented here. In the first case study, the single overloading ratio (SOL) are $1.25\left(\sigma_{OVL-1} = 26.63\ \text{MPa}\right)$, and 1.375 $\left(\sigma_{OVL-2} = 29.29\ \text{MPa}\right)$ is applied at initial crack length (a_{o-1} = 17.7 mm). The

second case is the overloading ratio (SOL) of 1.25 $(\sigma_{OVL-1} = 26.63\ MPa)$ and 1.375 $(\sigma_{OVL-2} = 29.29\ MPa)$ is applied at two different crack length (a_{o-1} = 17.7 mm and a_{o-2} = 21.0 mm), respectively. Final test case has two different overloading ratio (SOL) condition which applied at two difference crack length (a_{o-1} = 17.7 mm and a_{o-2} = 21.0 mm). The overloading ratio (SOL) of 1.25 $(\sigma_{OVL-1} = 26.63\ MPa)$ is applied at a_{o-1} = 17.7 mm and then at crack length a_{o-2} of 21.0 mm the overloading ratio (SOL) of 1.375 $(\sigma_{OVL-2} = 29.29\ MPa)$ is applied. All case study results are compared with the Wheeler-Irwin model prediction by using the parameter P = 0.3748 and $\lambda = 0.3748$ [64].

Table 8.13 The value of two different crack length, constant amplitude loading σ_{CAL} and two different single overloading σ_{OVL}

a_{o-1} **(mm)**	a_{o-2} **(mm)**	σ_{CAL} **(MPa)**	σ_{OVL-1} **(MPa)**	σ_{OVL-2} **(MPa**
17.7	21.0	21.3	26.63	29.29

8.3.3 Results and Discussion

Table 8.14 and 8.15 present the results obtained from the preliminary computation of number of cycles in two different value of toughness for the applied overloading ratio (SOL) of 1.25 and 1.375, respectively. The number of cycles for constant amplitude loading (CAL) and overloading (OVL) for each incremental crack length (Δa) are also shown in both tables. Furthermore, the retardation parameter (Cp) which is defined as ratio between overloading (OVL) and constant amplitude loading

(CAL) is presented here. It can be seen from the tables that the number of cycles for overloading (OVL) are significantly increased for both values of variable toughness.

The average retardation parameter (Cp-ave) is utilized to predict the fatigue crack retardation curve as shown in Figure 8.18 and 8.19. Both figures present the predictions for fatigue crack growth retardation due to single overloading ratio (SOL) of 1.25 and 1.375, respectively. As shown from both figures the single overload can induce crack growth retardation. The predictions from the retardation model are in good agreement with the Wheeler-Irwin model for both values of single overloading ratio.

As evident on inspection of Figure 8.20 and 8.21, the double overload induces crack growth retardation. Figures present the fatigue crack growth due to constant amplitude loading (CAL) and double overloading modeling based on Wheeler-Irwin model for single overloading ratio 1.25 and 1.375, respectively. Figure 8.20 and 8.21 also provide a comparison between results from the prediction of retardation model and the Wheeler-Irwin model for both overloading ratio. It can be seen that the predictions from the retardation model are in excellent agreement with Wheeler-Irwin model.

The prediction methodology is also implemented for double overloading with different overloading ratios for each crack length. At the first time, the overloading ratio (SOL) of 1.25 applied at a 17.7 mm crack length and then continuing with applied the overload ratio (SOL) is 1.375 at 21.0 mm of crack length. The crack

growth curve is shown in Figure 8.22 It can be seen that the prediction of retardation methodology is still in excellent agreement results with Wheeler-Irwin model.

8.4. Summary

It is established in this chapter that fatigue crack growth curves can be predicted by means of a unified fast-track method and extrapolation methodology. The new methodology provides excellent agreement with an empirical model and experimental results. The methodology is limited to the constant amplitude loading. However for variable amplitude loading, fatigue crack growth curves can be predicted by using the data obtained for constant amplitude loading but involve the determination of a retardation parameter. This methodology gives good agreement with an empirical model for variable amplitude loading case.

Table 8.14 The comparison of number of cycles obtained from computation between constant amplitude loading and the overloading with SOL = 1.25

Δa (mm)	Gc = 5.0 N/mm			Gc = 7.5 N/mm			Cp-ave
	CAL	OVL	Cp	CAL	OVL	Cp	
0.1	26	29	1.12	41	63	1.54	1.33
0.2	43	65	1.51	70	118	1.69	1.60
0.3	59	80	1.36	93	142	1.53	1.44
0.4	74	95	1.28	119	168	1.41	1.35
0.5	89	110	1.24	142	191	1.35	1.29
0.6	104	125	1.20	167	216	1.29	1.25
0.7	118	139	1.18	189	238	1.26	1.22
0.8	132	154	1.17	213	262	1.23	1.20
0.9	146	167	1.14	234	284	1.21	1.18
1.0	159	180	1.13	255	304	1.19	1.16

Table 8.15 The comparison of number of cycles obtained from computation between constant amplitude loading and the overloading with SOL = 1.375

Δa (mm)	Gc = 5.0 N/mm			Gc = 7.5 N/mm			Cp-ave
	CAL	OVL	Cp	CAL	OVL	Cp	
0.1	26	24	0.92	41	50	1.22	1.07
0.2	43	75	1.74	70	153	2.19	1.96
0.3	59	94	1.59	93	182	1.96	1.78
0.4	74	110	1.49	119	208	1.75	1.62
0.5	89	125	1.40	142	231	1.63	1.52
0.6	104	140	1.35	167	256	1.53	1.44
0.7	118	154	1.31	189	278	1.47	1.39
0.8	132	168	1.27	213	302	1.42	1.35
0.9	146	182	1.25	234	323	1.38	1.31
1.0	159	195	1.23	255	344	1.35	1.29

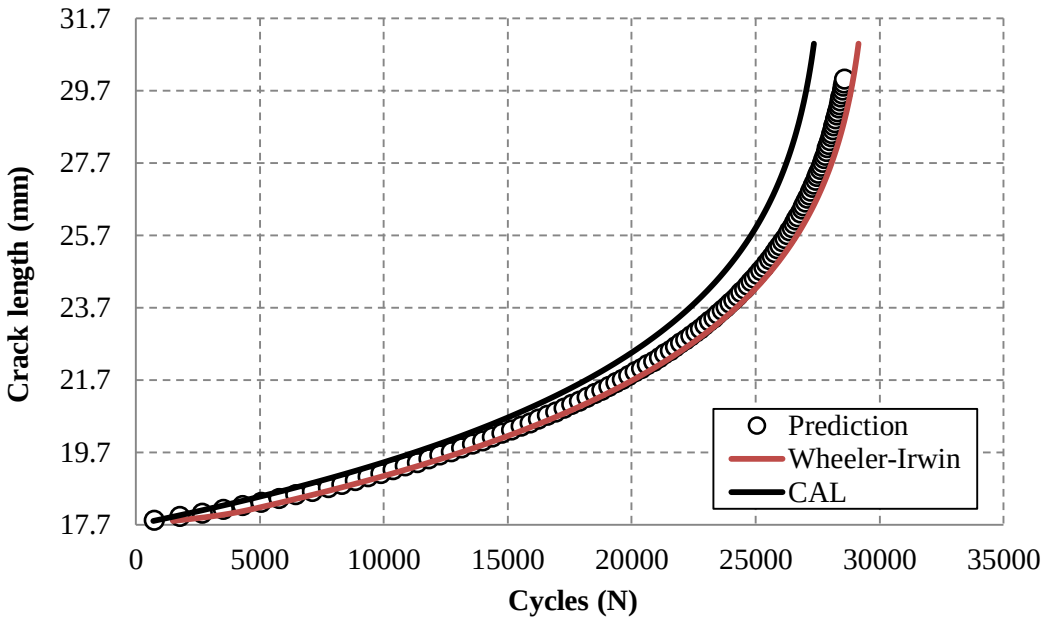

Figure 8.18 The comparison results of fatigue crack growth for single overloading SOL of 1.25

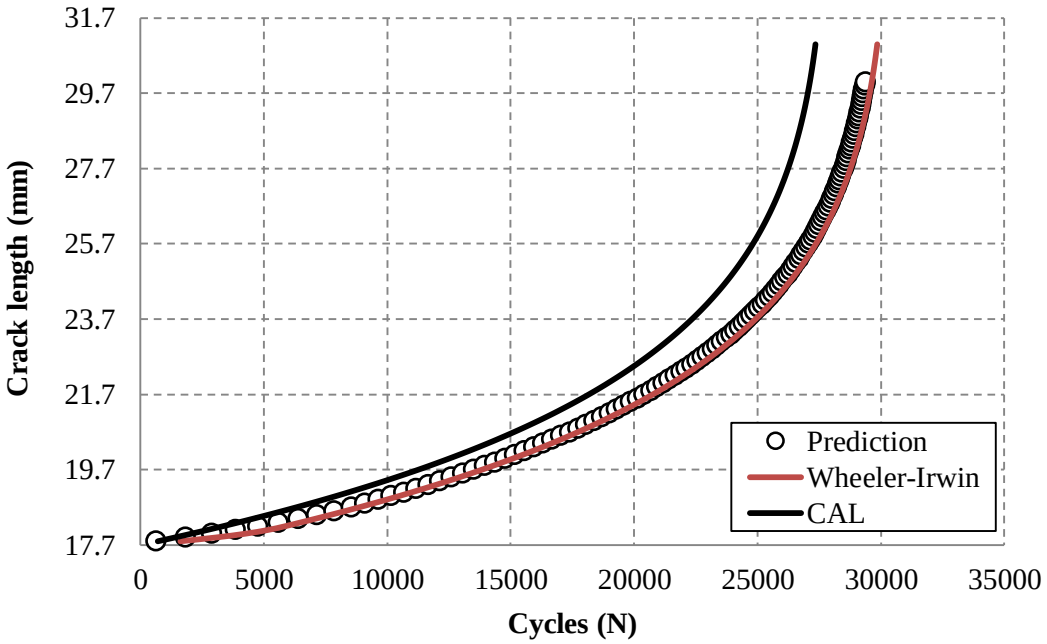

Figure 8.19 The comparison results of fatigue crack growth for single overloading SOL =1.375

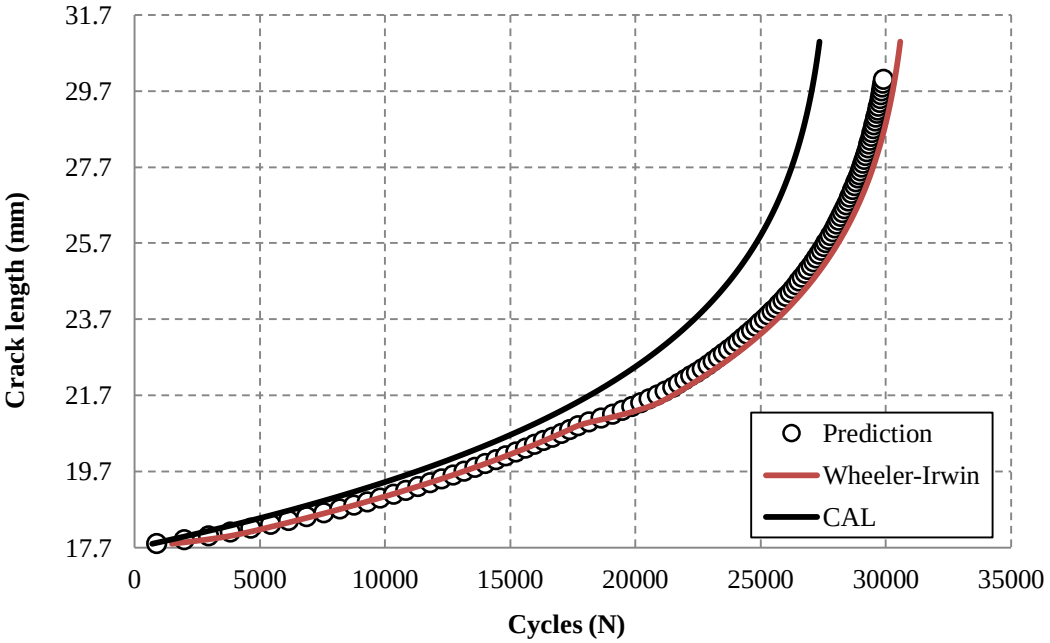

Figure 8.20 The comparison results of fatigue crack growth for double overloading SOL =1.25

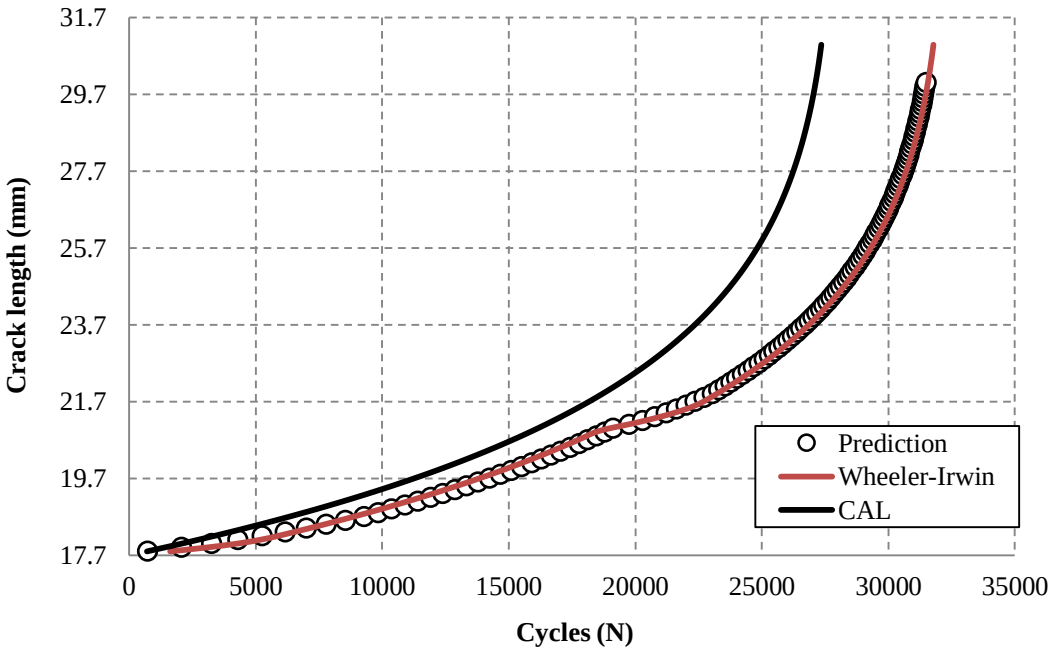

Figure 8.21 The comparison results of fatigue crack growth for double overloading SOL =1.375

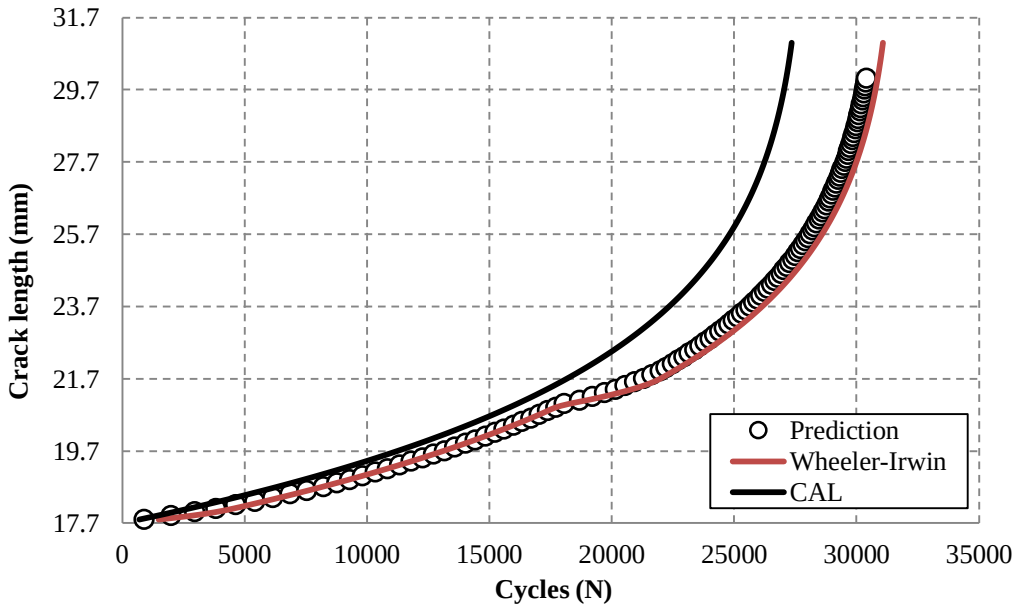

Figure 8.22 The comparison results of fatigue crack growth for difference value of double overloading SOL =1.25 and SOL =1.375

Chapter 9

Conclusion and Recommendation for Further Work

9.1. Conclusion

The cohesive zone model is one of a number of alternative approaches to simulate fatigue crack growth. The model utilizes a relationship between the cohesive traction and separation occurring in a zone ahead of the crack tip. The model introduces irreversibility into the constitutive relationships by means of damage accumulation with cyclic loading. The traction-separation relationship underpinning the cohesive zone model is not required to follow a predetermined path, but is dependent on irreversibility introduced by decreasing the critical traction value.

The cohesive energy is defined as the total of separation energy in the damage zone which is dissipated on creating new surface. However, there is the energy supplied

into the damage zone and this or portion of this energy should reach a critical criterion before the separation energy starts to release. The practical demonstration in the one dimension model in Chapter 4 reveals that elastic strain energy supplies energy into damage zone model for both elastic and elastic-plastic materials. The combination of transport equation and cohesive element demonstrates the mechanism. Meanwhile, the plastic energy completely dissipated for the cohesive model considered when applied to elastic plastic materials.

It is demonstrated in this thesis that crack growth simulated by a cohesive zone model is able to capture crack growth without the need for re-meshing. The cohesive zone model has been used as a vehicle for understanding. The mechanism of fatigue crack growth, where the crack tip separates and cohesive energy is released for elastic-plastic materials. It has been demonstrated that the model can also be applied to simulate the phenomenon of fatigue crack growth retardation. It is shown in Chapter 5 that the amount of retardation occurring in elastic-plastic materials is affected by value of critical cohesive traction. The lager the value of critical cohesive traction, the larger the number of cycles required to propagate a crack. This phenomenon also occurs with overloading ratio where lager the value of overloading ratio ease to an increase in the number of cycles retarded.

Fatigue analysis in a cohesive zone model involves the accumulation of separation energy released per cycle. A crack starts to growth when the accumulation of separation energy reaches a critical value known as toughness. It is revealed that for small scale yielding with the assumption of the fixed critical cohesive traction,

varying toughness does not significantly affect the stress level at the crack tip and also the change in elastic energy for the same incremental crack length. In contrast the plastic energy dissipated increases with toughness. Separation energy is shown to release in the same manner per cycle for the same incremental crack length. It can be concluded that varying toughness with the assumption of a fixed critical cohesive traction and small scale-yielding that the number of cycles has linear relationship with toughness provided the separation energy per cycle remains invariant.

An alternative methodology has been introduced to accelerate the simulation of fatigue crack growth. The method adopts an artificial material property i.e. toughness. The basic intention is that a reduced toughness has the effect of reducing the number of cycles to failure. The approach outlined in Chapter 6 establishes a functional relationship between the number of cycles and variable artificial toughness. The proposed method shows the excellent agreement to the numerical results obtained from packet program for constant amplitude loading and single overloading as demonstrated in Chapter 7.

It is established in the thesis that fatigue crack growth curves can be predicted by means of a unified fast-track method and an extrapolation methodology. The basic idea of the methodology is to find parameters in an empirical model by means of a curve fitting technique applied to set of data obtained from the fast track method. It is shown in Chapter 8 that the new methodology provide excellent agreement with an empirical model. The methodology is only applicable for the constant amplitude loading. However for variable amplitude loading, fatigue crack growth curves can be

predicted by using the data obtained for constant amplitude loading and involve to determination of a retardation parameter. The parameter can be determined by considering the ratio of the number of cycles delayed using the cohesive zone model. The retardation parameter has been established by different value of toughness. This methodology gives good agreement with an empirical model for variable amplitude loading case.

9.2. Recommendation for Further Work

From the study and corresponding conclusions above, there are some recommendations for further work, i.e.

- The preliminary investigation using the combination of the transport equation and cohesive element shows that the elastic strain energy dominantly supplies the driven energy to the crack surface. However in this study, the practical demonstration is limited to a one dimension model. The enhancement of the concept requires further investigation especially in two or three dimensions. In further models, alternative energy concept can be compared with more traditional approaches, e.g. the J-integral.
- In elastic-plastic materials, plastic deformation plays a major role in fatigue crack growth retardation. The influence of plastic deformation in cohesive zone model is modified by the critical cohesive traction. Therefore, further study is recommended to establish definitely the critical cohesive traction.
- The fast-track method is introduced by reducing the toughness to decrease the number of cycles to failure. This method establishes a functional relationship

between the number of cycles and variable artificial toughness. However the proposed method assumes small-scale yielding. An additional investigation should be performed to evaluate the applicability of the new approach to the large scale yielding condition. It is also recommended to implement the fast track method to solve the problem in industrial components.

Reference

[1]. Paris, P.C., Gomez, M.P. & Anderson, W.P. , A rational analytic theory of fatigue. The Tren. in Engineering, 1961. 13: p. 9-14.

[2]. Laird, C., Mechanisms and Theories of Fatigue. . In: Fatigue and Microstructure. American Society for Metals, 1979: p. 149-203.

[3]. Foreman, R.G., Kearney, V. E., and Engle, R. M. , Numerical analysis of crack propagation in cyclic loaded structures. J. Basic Eng. Tram ASME. Series D, 1967. 89: p. 459-464.

[4]. Pearson, S., Effect of mean stress in 12.6 mm aluminum alloys of high and low fracture toughness. Engineering Fracture Mechanic, 1972. 4.

[5]. Elber, W., Fatigue crack closure under cyclic tension. Journal Engineering Fracture. Mechanics, 1970. 2: p. 37-45.

[6]. Ural, A., Krishnan, V. R., Papoulia, K. D. , A cohesive zone model for fatigue crack growth allowing for crack retardation. International Journal of Solids and Structures, 2009. 46: p. 2453-2462.

[7]. Beaurepaire, P., Schueller, G. I. , Modeling of variability of fatigue crack growth using cohesive zone elements. Engineering Fracture Mechanics, 2011. 78: p. 2399-2413.

[8]. Elices, M., Gunea, G. V., Gomez, J., Planas, J. , The cohesive zone model: advantages, limitation and challenges. Engineering Fracture Mechanics. Engineering Fracture Mechanics, 2002. 69: p. 137-163.

[9]. Rice, J.R., A path independent integral and the approximate analysis of strain concentration by notches and cracks. ASME J. Appl. Mech, 1968a. 35: p. 379-386.

[10]. Rice, J.R., Mathematical analysis in the mechanics of fracture. In: Liebowitz, H. (Ed.), Fracture—An Advanced Treatise, Academic Press, New York, 1968b. 2: p. 191-311.

[11]. Simha, N.K., Fischer, F. D., Shan, G.X., Chen, C.R., Kolednik, O, J-integral and crack driving force in elastic–plastic materials. Journal of the Mechanics and Physics of Solids, 2008. 56(9): p. 2876-2895.

[12]. Dugdale, D.S., Yielding of Steel Sheets Containing Slits. Journal of the Mechanics and Physics of Solids, 1960. 8: p. 100-108.

[13]. Barenblatt, G.I., The mathematical theory of equilibrium cracks in brittle fracture,. Advance Applied Mechanics, 1962. 7(55-129).

[14]. Hillerborg, A., Modeer, M., Petersson, P.E., Analysis of crack formation and crack growth in concrete by means of fracture mechanics and finite element. Cement Concrete, 1976. 6: p. 773-781.

[15]. Ritchie, R.O., Mechanisms of fatigue-crack propagation in ductile and brittle solids. International Journal of Fracture, 1999. 100: p. 55-83.

[16]. Irwin, G.R., Analysis of stresses and strains near the end of a crack traversing a plate. ASME J. Appl. Mech, 1957. 24: p. 361-364.

[17]. Elber, W., Damage Tolerance in Aircraft Structure. ASTM STP 486, American Society for Testing and Materials, 1971: p. 230-242.

[18]. Aliaga, D., Davy, A., Schaff, H. , A simple crack closure model for predicting fatigue crack growth under flight simulation loading. . In: Newman

JC, Elber, W, editors. Mechanics of fatigue crack closure, ASTM STP 982. Philadelphia: American Society for Testing and Materials, 1988. 491-504.

[19]. De Ko¨ning, A.U., A simple crack closure model for prediction of fatigue crack growth rates under variable-amplitude loading. In: Roberts R, editor. Fracture mechanics, ASTM STP 743. Philadelphia: American Society for Testing and Materials, 1981: p. 63-85.

[20]. Newman, J.C.J., A crack closure model for predicting fatigue crack growth under aircraft spectrum loading. Method and Models for Predicting Fatigue Crack Growth under Random Loading. ASTM STP 748. J. B. Chang and C. M. Hudson, Eds. American Society for Testing and Materials. , 1981: p. 53-84.

[21]. Newman, J.C.J., Prediction fatigue crack growth under variable- amplitude and spectrum loading using a closure model. In: Abelkis PR, Hudson CM, editors. Design of fatigue and fracture resistant structure. ASTM STP 761. Philadelphia: American Society for Testing and Materials, 1982: p. 255-277.

[22]. Yamadaa, Y., Lacya, T., Newman J. Jr., Smithb, B. L., Kumar, B., Effects of crack closure on fatigue crack-growth predictions for 2024-T351 aluminum alloy panels under spectrum loading. International Journal of Fatigue. International Journal of Fatigue, 2007. 29: p. 1503-1509.

[23]. Solankia, K., Daniewicza, S.R., Newman, J.C. Jr. , Finite element analysis of plasticity-induced fatigue crack closure: an overview. Engineering Fracture Mechanics, 2004. 71: p. 149-171.

[24]. Lee, S.Y., Song, J., H, Crack closure and growth behavior of physically short fatigue cracks under random loading. Engineering Fracture Mechanics, 2000. 66: p. 321-346.

[25]. Toribio, J., Kharin, V. , Simulations of fatigue crack growth by blunting–re-sharpening: Plasticity induced crack closure vs. alternative controlling variables. International Journal of Fatigue, 2012.

[26]. El-Zeghayara, M.T., T.,H., Conleb, F.A. Bonnenc, J.J.F, Modeling crack closure and damage in variable amplitude fatigue using smooth specimen fatigue test data. International Journal of Fatigue, 2011. 33: p. 223-231.

[27]. Borregoa, L.P., Antunesb, F.V., Costab, J.D., Ferreira, J.M.,, Numerical simulation of plasticity induced crack closure under overloads and high–low blocks. Engineering Fracture Mechanics, 2012. 95: p. 57-71.

[28]. Pippan, R., Grosinger, W, Fatigue crack closure: From LCF to small scale yielding. International Journal of Fatigue, 2013. 46: p. 57-71.

[29]. Noroozi, A.H., Glinka, G., Lambert, S. , A two parameter driving force for fatigue crack growth analysis. International Journal of Fatigue, 2005. 27: p. 1277-1296.

[30]. Griffith, A., A. , The phenomena of rupture and flow in solids. Philos. Trans. R. Soc. London A 221, 1921: p. 163-198.

[31]. Rice, J.R., The mechanics of crack tip deformation and extension by fatigue. Symp. on fatigue crack growth In: ASTM-STP-415, 1967.

[32]. Turner, C.E., A re-assesment of ductile tearing resistance (Part I). In: Firrao D editor. Fracture behavior and design of materials and structures, proc. ECF 1990. 8: p. 933-943.

[33]. Turner, C.E., A re-assesment of ductile tearing resistance (Part II). In: Fracture behavior of materials and structures, proc. ECF, 1990. 8: p. 951-968.

[34]. Cojocaru, D., Karlsson, A.M., Assessing plastically dissipated energy as a condition for fatigue crack growth. International Journal of Fatigue, 2009. 31: p. 1154-1162.

[35]. Daily, J.S., Klingbeil, N., W., Plastic dissipation in fatigue crack growth under mixed-mode loading. International Journal of Fatigue, 2004. 26: p. 727–738.

[36]. Daily, J.S., Klingbeil, N., W., Plastic dissipation in mixed-mode fatigue crack growth along plastically mismatched interfaces. International Journal of Fatigue, 2006. 28: p. 1725–1738.

[37]. Klingbeil, N., W., A total dissipated energy theory of fatigue crack growth in ductile solids. International Journal of Fatigue, 2003. 25: p. 117-128.

[38]. Cojocaru, D., Karlsson, A. M. , An object-oriented approach for modeling and simulation of crack growth in cyclically loaded structures. Advance Engineering Software, 2008. 38(12): p. 995-1009.

[39]. Camacho, G., Ortiz, M. , Computational modelling of impact damage in brittle materials. International Journal of Solids and Structures, 1996. 33: p. 2899-2938.

[40]. Roe, K., L., Siegmund, T. , An Irreversible Cohesive Zone Model for Interface Fatigue Crack Growth Simulation. Engineering Fracture Mechanics, 2003. 70(209-232).

[41]. Jiang, H., Gao, X., Srivatsan, T.S., , An Irreversible Cohesive Zone Model for Interface Fatigue Crack Growth Simulation. Engineering Fracture Mechanics, 2009. 70: p. 209-232.

[42]. Brinkmann, S., Siegmund, T., Computations of fatigue crack growth with strain plasticity and an irreversible cohesive zone model. Engineering Fracture Mechanics, 2008. 75: p. 2276-2294.

[43]. Matthieu, M., M., Fedelich, B, Simulation of fatigue crack growth by crack tip plastic blunting using cohesive zone elements. Procedia Engineering, 2010. 2: p. 2055-2064.

[44]. Tvergaad, V., Overload effects in fatigue crack growth by crack-tip blunting. International Journal of Fatigue, 2005. 27: p. 1389 – 1397.

[45]. Tvergaad, V., Effects of underloads and overloads in fatigue crack growth by crack-tip blunting. Engineering Fracture Mechanics, 2006. 73: p. 869-879.

[46]. Kim, K.S., Kim, S.C., Shim, C.S., & Park, J.Y., A studying on the effect of overload Ratio on Fatigue Crack Growth. Key Engineering Materials, 2004: p. 1159-1168.

[47]. Wheeler, O.E., Spectrum loading and crack growth. Journal Basic Engineering, Trans ASME, Ser. D, 1972: p. 81-86.

[48]. Xiaoping, H., Moan, T., Weicheng, C, An engineering model of fatigue crack growth under variable amplitude loading. International Journal of Fatigue, 2008. 30: p. 2-10.

[49]. Harmain, G.A., A model for predicting the retardation effect following a single overload. Theoretical and Applied Fracture Mechanics, 2010.

[50]. Pavlou, D.G., Vlachakis, N.V., Pavlou, M.G., Vlachakis, V.N, Estimation of fatigue crack growth retardation due to crack branching. Computational Materials Science, 2004. 29: p. 446-452.

[51]. Siegmund, T., A numerical study of transient fatigue crack growth by use of an irreversible cohesive zone model. International Journal of Fatigue, 2004. 26: p. 929-939.

[52]. Huneau, B., Mendez, J. , Evaluation of environmental effects on fatigue crack growth behavior of a high strength steel in a saline solution with cathodic protection. International Journal Fatigue, 2006. 28: p. 124–131.

[53]. Hsu, K.C., Lin, C.K, Effects of R-ratio on high-temperature fatigue crack growth behavior of a precipitation–hardening stainless steel. International of J Fatigue, 2008. 12: p. 2147–2155.

[54]. Dominguez, J., Zapatero, J., Pascual, J. , Effect of the load histories on scatter of fatigue crack growth in aluminum alloy2024-T 351. Engineering Fracture Mechanics, 1997: p. 65-76.

[55]. Zhao, H., An improved probabilistic model of fatigue crack growth. Engineering. Fracture Mechanics, 1993: p. 773–780.

[56]. Wu, W.F., Ni, C.C. , Probabilistic models of fatigue crack propagation and their experimental verification. Probabilistic Eng. Mechanic, 2004: p. 247–257.

[57]. Mohanty, J., R, Verma, B,B, Ray, P.K, Evaluation of overload-induced fatigue crack growth retardation parameters using an exponential model. Engineering. Fracture Mechanic, 2008: p. 3941-3951.

[58]. Ahn, J.J., Ochiai, S, Statistical analysis for application of the Paris equation to whisker reinforced metal matrix composites. International Journal Fatigue, 2003: p. 231-236.

[59]. Schijve, J., Fatigue of Structures and Materials, 2nd edition. Springer, 2009.

[60]. Broek, D., Elementary Engineering Fracture Mechanics, 3rd revised edition. Martinus Nijhoff, 1982.

[61]. Irwin, G.R., Plastic zone near a crack and fracture toughness Proc. Sagamore Conf., 1960: p. IV-63.

[62]. Geary, W., A review of some aspects of fatigue crack growth under variable amplitute loading. International Journal Fatigue, 1992: p. 377-386.

[63]. Fatigue Design Handbook, 2nd edition, SAE. 1988.

[64]. Mohanty, J.R., Verma, B. B., Ray, P. K. , Prediction of fatigue crack growth and residual life using an exponential model: Part II (mode-I overload induced retardation). International Journal of Fatigue, 2009. 31: p. 425–432.

[65]. Klingbeil, N.W., A total dissipated energy theory of fatigue crack growth in ductile solids. International Journal of Fatigue, 2003. 25: p. 117-128.

[66]. Sun, C.T.J., Z.-H., Fracture Mechanics. Academic Press is an imprint of Elsevier, 2012.

[67]. Geubelle, P.H., Baylor, J. S., Impact-induced delamination of composite: a 2D simulation. Composites Part B 1998: p. 589–602.

[68]. Qiu, Y., Crisfield, M. A., Alfano, G. , An interface element formulation for the simulation of delamination with buckling. Engineering Fracture Mechanic, 2001. 68: p. 1755-1776.

[69]. Turon, A., Camanho, P.,P. Costa, J., Davila, C., G., A damage model for the simulation of delamination in advance composites under variable-mode loading. Mechanics of Materials, 2006. 38: p. 1072-1089.

[70]. Sarrado, C., Turon, A., Renart, J., Urresti, I.,, Assessment of energy dissipation during mixed-mode delamination growth using cohesive zone models. Composites: Part A, 2012. 43: p. 2128-2136.

[71]. Tvergaad, V., Hutchinson, J., W., The relation between crack growth resistance and fracture process parameter in elastic-plastic solid. J. Mech. Phys. Solids, 1992. 40: p. 1377-1397.

[72]. Siegmund, T., n Needleman, A., A numerical study of dynamic crack growth in elastic-vicoplastic solids. Int. J. Solids Structure, 1997. 34: p. 769-787.

[73]. Needleman, A., An analysis of tensile decohesion along an interface. J. Mech. Phys. Solids, 1990. 38: p. 289-324.

[74]. Xu, X.-P., Needleman, A., Numerical simulations of fast crack growth in brittle solids. J. Mech. Phys. Solids, 1994. 42: p. 1397-1434.

[75]. Ortiz, M., Pandolfi, A., Finite-deformation irreversible cohesive elements for three-dimensional crack propagation analysis. Int. J. Numer. Meth. Eng., 1999. 44: p. 1267-1282.

[76]. Roy, Y.A., Dodds, R. H. Jr., An Irreversible Cohesive Zone Model for Interface Fatigue Crack Growth Simulation. Engineering Fracture Mechanics, 2003. 70: p. 209–232.

[77]. Scheider, I., Brocks, W., Cohesive element for thin-walled strctures. Computational Materials Science, 2006. 37: p. 101-109.

[78]. Scheider, I., Schodel, M., Brocks, W., Schonfeld, W., Crack propagation analyses with CTOA and cohesive model: Comparison and experimental validation. Engineering Fracture Mechanics, 2006. 73: p. 252-263.

[79]. Hutchinson, J.W., Evans, A. G., Mechanics of materials: top-down approaches to fracture. Acta mater, 2000. 48: p. 125-135.

[80]. Jin, Z., H., Sun, C., T., Cohesive zone modeling of interface fracture in elastic bi-materials. Engineering Fracture Mechanic, 2005. 72: p. 1805-1817.

[81]. de-Andres, A., Perez, J. L., Ortiz, M., Elastoplastic _nite element analysis of three!dimensional fatigue crack growth in aluminum shafts subjected to axial loading. International Journal of Solids and Structures, 1999. 36: p. 2231-2258.

[82]. Nguyen, O., Repetto, E. A., Ortiz, M. and Radovitzky, R. A. , A cohesive model of fatigue crack growth. International Journal Fracture, 2001. 110: p. 351-369.

[83]. Mohanty, J.R., Verma, B. B., Ray, P. K. , Prediction of fatigue crack growth and residual life using an exponential model: Part I (constant amplitude loading). International Journal of Fatigue, 2009. 31: p. 418-424.

[84]. Cornec, A., Scheider, I., Schwalbe, K. H., On the practical application of cohesive model. Engineering Fracture Mechanic, 2003. 70: p. 1963-1987.

[85]. Janssen, M., Zuidema, J. , Fracture Mechanics Second Edition. Spon Press, New York, USA, 2004.

[86]. Li, W., Siegmund, T., An analysis of crack growth in thin-sheet metal via a cohesive zone model. Eng. Fracture Mechanics, 2002: p. 2073–2093.